PhD Course in

Bioengineering and Robotics

Curriculum: Bioengineering and Bioelectronics

XXX Cycle

PhD Dissertation title

Ultra conformable and multimodal tactile sensors based on organic field-effect transistors

Scientific Field

ING-INF/06

PhD Candidate: Fabrizio Antonio Viola

Advisor: Prof. Annalisa Bonfiglio

Co-Advisor: Prof. Piero Cosseddu

Academic year of PhD defense 2017-2018

Outline

Cognitive psychology is the branch of psychology related to all the processes by which sensory input is transformed, processed and used. Academic and industrial research has always invested time and resources to develop devices capable to simulate the behavior of the organs where the perceptions are located.

In recent years, in fact, there have been numerous discoveries related to new materials, and new devices, capable of reproducing, in a reliable manner, the sensory behavior of humans. Particular interest in scientific research has been aimed at understanding and reproducing of man's tactile sensations. It is known that, through the receptors of the skin, it is possible to detect sensations such as pain, changes in pressure and/or temperature.

The development of tactile sensor technology had a significant increase in the last years of 1970s, thanks to the important surveys of Stojiljkovic, Harmon and Lumelsky who presented the firsts prototype of sensors for *artificial skin* applications, and summarized the main characteristics and requirements of tactile sensors.

Recently, organic electronics has been deeply investigated as technology for the fabrication of tactile sensors using biocompatible materials, which can be deposited and processed on ultra flexible and ultra conformable substrates. In general, the most attractive property of these materials is mainly related to their high mechanical flexibility, which is mandatory for artificial skin applications.

The main object of this PhD research activity was the development and optimization of an innovative technology for the realization of physical sensors able to detect pressure and temperature variations, which can be applied in the field of biomedical engineering and biorobotics.

By exploiting the particular characteristics of the employed materials, such as mechanical flexibility, the proposed sensors are very suitable to be integrated with flexible structures (for example plastics) as a pressure and temperature sensor, and therefore, ideal for the realization of an artificial skin like.

In Chapter 1, the basics of humans somatosensory system will be introduced: after a brief description of tactile thermoreceptors, mechanoreceptors and nociceptors, a definition of electronic skin and its characteristics will be provided.

In Chapter 2, a wide analysis of the state of the art will be reported. Several and different examples of tactile sensor (in inorganic and organic technology) will be presented, underlining advantages and disadvantages for each approach.

In Chapter 3, the firsts experimental results, obtained in the first part of my PhD program, will be presented. All the steps of the fabrication process of the devices will be described, as well as the measurement setup used for the electrical characterization of the sensors.

In Chapter 4, the sensor structure optimization will be presented. It will be demonstrated how the presented devices are able to sense simultaneously thermal and mechanical stimuli. Moreover, it will be demonstrated that, thanks to an alternative and innovative fabrication process, the sensors can be transferred directly on skin, thus proving the suitability of the proposed sensor architecture for tactile applications.

Contents

List of Figures

List of Tables

1 Tactile perception and electronic skin

In this Chapter the basic concepts of the human somatosensory system will be introduced, with a particular focus on sensory transduction. After a brief description of tactile thermoreceptors, mechanoreceptors and nociceptors, a description of electronic skin and its characteristics will be provided.

1.1 Somatosensory system

The human tactile system, unlike others sensory systems, is not located in a specific apparatus, but it is distributed in different parts of the human body like skin, muscles, skeleton etc. This system plays a fundamental role in modelling humans interplay with our surroundings in terms of pain, temperature and, finally, touch.

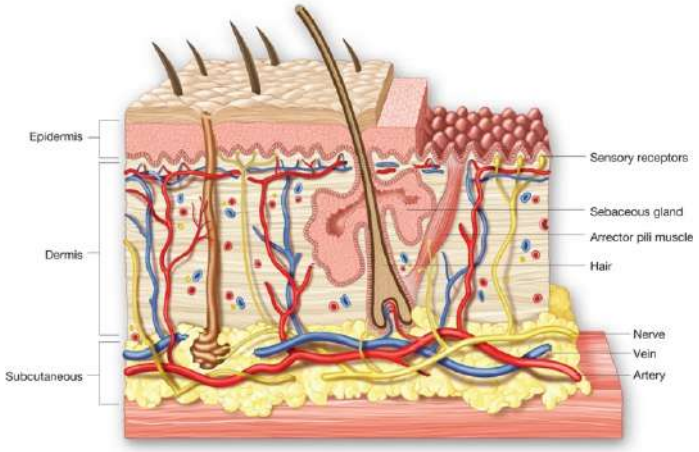

Fig. 1.1: Anatomy of the human skin. (Courtesy of http://humananatomylibrary.com)

The skin (*cutaneous system*) is the largest organ in the human body and it is a very important part of the tactile system; it performs the function of protection from bacteria, viruses and hazardous external substances, it provides a proper thermoregulation (i.e. the possibility to adapt our body to a great diversity of climates, including hot humid, hot arid and warm), it helps to maintain our structural integrity, and it achieves the function of sensation. These functions are allowed by a complex network of sensors (i.e. *somatosensory neurons* or *tactile receptors*) that receive specific

inputs from the surrounding environment, and in particular about object properties, such as size, roughness, softness, temperature etc.

As shown in Fig. 1.1, the skin is constituted of different layers, the *subcutaneous tissue* (also called *hypodermis* or *subcutis*), the *dermis* and the *epidermis*:

- subcutaneous tissue: connects the dermis with the other underlying tissue. It is used chiefly for fat storage, and it operates as filling and as a reserve of energy.
- Dermis: it is constituted of connective tissue and it's connected to the epidermis through a basement membrane. Most of the tactile receptors are located in this layer of skin.
- Epidermis: is the external layer of skin, so the fundamental function is to provide a barrier to external environment. It is formed of five different layers (namely cornified, translucent, granular, spinous, and basal layer).

There are several structural types of receptors in the skin. Tactile receptors fall into the category of *encapsulated* receptors or *non-encapsulated* receptors (see Fig. 1.2). The non-encapsulated receptors or *free nerve endings*, are simply the peripheral end of the nervous system. These mostly respond to noxious (pain) and thermal stimuli but there are also some specialized free nerve endings around hairs that respond to very light touch. The encapsulated endings are specialised nerve endings covered by a various number of connective layers, which influence the response characteristics of the nerves. Most encapsulated receptors are for touch.

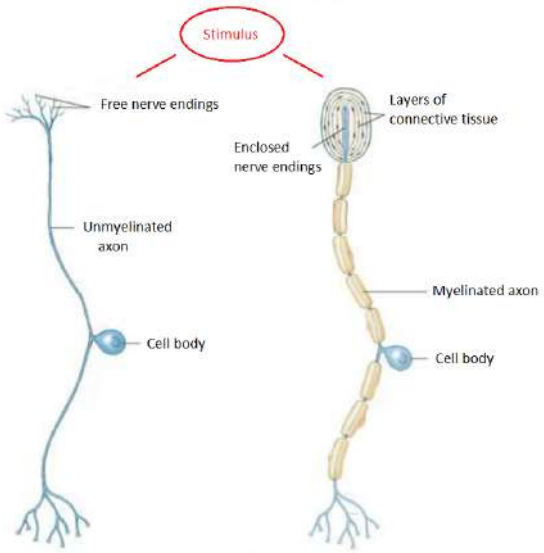

Fig. 1.2: Different structures of tactile neurons.

Since the different parts constituting the human nervous system communicate through electric signals, tactile receptors must transduce the sensory inputs into electric signals that propagate to the *central nervous system* (CNS) where they are eventually elaborated within the brain. The nervous system receives inputs not only from tactile receptors, but also from a large number of

sensory receptors: photoreceptors in the eyes, taste receptors on the tongue, odorant receptors in the nose etc.

The *law of specific nerve energies*, proposed by Johannes Muller in 1835, assumes that each type of sensation depends on the part of the CNS in which a specific fibre terminate. Consequently, each type of receptors is specific for a particular stimulus (called *modality*).

1.2 Sensory transduction and neural adaptation

As already mentioned, tactile receptors are themselves neurons (free or encapsulated nerve endings) and can generate electric signals in response to a stimulus. These signals are called *action potentials* and they are the way employed by the human somatosensory system to communicate with the CNS. Action potentials are temporary ions displacements occurring through the neurons' membrane that can be caused by tactile stimuli or, more in general, by a specific modality (see Fig. 1.3a). Action potentials are also called *nerve impulses*.

To understand how neurons are able to communicate to each other, it is necessary to describe the role of their membrane in generating these signals. Neurons have a negative concentration gradient most of the time due to a dynamic equilibrium given by several phenomena such as the different concentration of chlorine, calcium, sodium, and potassium ions between intracellular and extracellular fluids, the different cell membrane permeability to these ions, and the presence of active mechanisms such as the ATP-dependent Na+/K+ pump.

The resulting transmembrane potential of a cell depends on the dynamic equilibrium that occurs across its plasma membrane, which is related by the reversal potentials of the ions to which the cell is somehow permeable. For instance, considering a single ion, e. g. potassium, its reversal potential is easily achievable using the Nernst equation:

$$V_K = \frac{RT}{zF}\left(\ln\frac{[K^+]_o}{[K^+]_i}\right). \tag{1.1}$$

On the other hand, if more than one ion contributes to the transmembrane potential, Nernst equation can not completely describe the whole mechanism and the resulting transmembrane potential is given by the Goldman-Hodgkin-Katz equation. Considering the contribution of the three main ions, namely Sodium Na^+, Potassium K^+, and Cl^-, the value of the resting potential V_{REST} is determined by dynamic equilibrium between the ion flow through the cell membrane and the active ion transport (efficiency of the ion pumps):

$$V_{REST} = \frac{RT}{F}\left(\ln\frac{p_K[K^+]_o + p_{Na}[Na^+]_o + p_{Cl}[Cl^-]_i}{p_K[K^+]_i + p_{Na}[Na^+]_i + p_{Cl}[Cl^-]_o}\right), \tag{1.2}$$

where:

- R is the universal gas constant (8.314 $J*K^{-1}*mol^{-1}$).
- T is the temperature in Kelvin.
- F is the Faraday's constant ($9.6485*10^4$ $C*mol^{-1}$).
- p_K is the membrane permeability for K^+.
- p_{Na} is the membrane permeability for Na^+.
- p_{Cl} is the membrane permeability for Cl^-.
- $[K^+]_o$ is the concentration of K^+ in the extracellular fluid.
- $[K^+]_i$ is the concentration of K^+ in the intracellular fluid.
- $[Na^+]_o$ is the concentration of Na^+ in the extracellular fluid.
- $[Na^+]_i$ is the concentration of Na^+ in the intracellular fluid.
- $[Cl^-]_o$ is the concentration of Cl^- in the extracellular fluid.
- $[Cl^-]_i$ is the concentration of Cl^- in the intracellular fluid.

The resulting transmembrane potential, is called *resting membrane potential* and has a value which depends on the type of cell. For example, in a typical neuron, the resting membrane potential is about -70 mV. The membrane remains at its resting potential until some event, such as for example an external stimulus, triggers a change in the extracellular potential and a subsequent modification of the membrane permeability (which is in turn determined by the kinetics of specific ion channels).

In general, it is possible to divide the period of a nerve impulse in four different phases:

I. Resting potential, in this phase the membrane potential is -70 mV.

II. Depolarization phase, the membrane begins to depolarize when an external stimulus is applied. Voltage-gated sodium channels are activated and this lets positively charged sodium ions flow into the negatively charged membrane, and depolarize it. The voltage begins a rapid rise toward +30 mV.

III. Repolarization phase, the membrane voltage starts to return to a negative value. The sodium pumps are closed and the potassium pumps opened.

IV. Undershoot or Hyperpolarization, in this phase the cell is more negative than its typical resting potential. Potassium channels stay open a little bit longer, and continue to let positive ions exit the neuron. As the potassium pumps close, the sodium-potassium channels works to set the resting state.

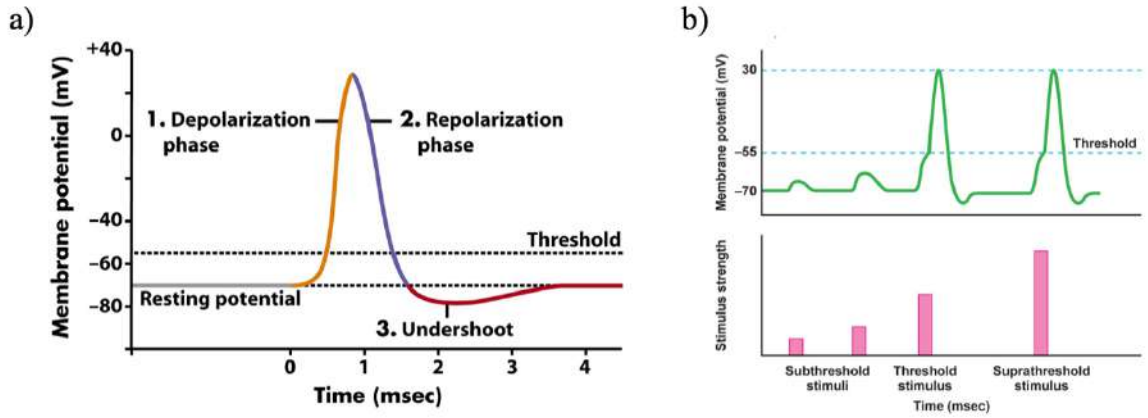

Fig. 1.3: a) Different phases of a nerve pulse. b) Representation of All-or-none law. [1]

Action potentials follow an *all-or-none* law: this principle, proposed by the American physiologist Henry Pickering Bowditch in 1871, says that the strength by which a receptor responds to an external stimulus is independent of the strength of the stimulus. When that stimulus overreaches the *threshold potential* of a neuron's membrane (see Fig. 1.3b), the neuron will give a complete feedback; otherwise, there is no response. In general, the threshold potential is of about -55 mV.

In view of the above, the information that the CNS uses to discriminate the strength of the stimulus is the frequency of the action potentials (*frequency code*), i.e. there is a strong and direct correlation between the intensity of the external stimuli the frequency of the nerve impulses. The precision of the localization of a stimulus is called *acuity* and it depends on the number of receptors excited during the sensory transduction. This number is related to the *receptive field* of the sensory unit i.e. the limited area of the sensory space in which an external stimulus can change the firing action of that neuron. It is possible to distinguish two categories of tactile receptors, based on the *adaptation* of the electric response of a receptor neuron.

According to [2] adaptation is "the decline of the electric responses of a receptor neuron over time in spite of the continued presence of an appropriated stimulus of constant strength".

- Slow adaptation (SA) or tonic receptors: they respond with a train of nerve impulses for all the duration of the external stimulus.
- Rapid adaptation (RA) or phasic receptors: they are sensitive only to dynamic stimuli.

In general, the most common division is based on the type of modality that they can detect: *mechanoreceptors* for the response to mechanical stimuli, *thermoreceptors* for the response to thermal stimuli and *nociceptors* for the response to pain.

1.3 Mechanoreceptors

A mechanoreceptor is a receptor that can sense mechanical pressure or shear forces. These kinds of receptors can be divided into different categories based on their structure.

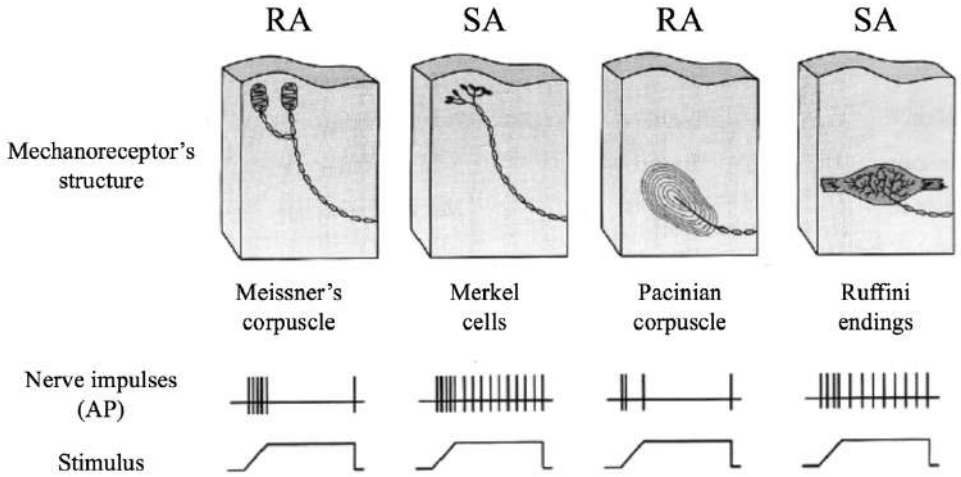

Fig. 1.4: Classification of mechanoreceptors and their adaptation. [3]

Meissner's corpuscules (RA I units): they have a small receptive field (3 – 4 mm) and a high sensitivity for dynamic forces in the range between [10 – 50 Hz]. They are located in different areas of the hairless skin, especially in lips and fingers with a spatial density of 140 units/cm^2. They have a cylindrical structure covered by different layers of connective tissue and are involved in the detection of low frequency vibrations, flutter, slip and motion detection.

Pacinian corpuscles (RA II units): these units are mostly responsible for rapid adaptation in human skin. They are in fact sensitive to high frequency forces [40 – 400 Hz] and they have a large receptive field (>20 mm). Pacinian corpuscles are located throughout the body in various areas in the subcutaneous layer of the skin, and they are involved in the detection of surface roughness and small vibrations.

Merkel cells (SA I units): they are densely located in hairless skin (70 units/cm^2). They have a small receptive fields and a high sensitivity to low-frequency dynamic skin deformation (< 5 Hz) and to static forces. Merkel cell are involved for fine form detection and texture discrimination.

Ruffini endings (SA II units): incorrectly classified in the past as thermoreceptors, these mechanoreceptors are activated by static stimuli applied perpendicularly, and respond well when skin is stretched. Ruffini endings are located in the deep layers of the skin (subcutaneous tissue) with a spatial density of 10 units/cm^2. They can sense the stretch of the skin especially around joints and fingernails and they contribute to finger position and motion detection, perception of the shape of an object.

Edin et al. [4] proposed in 1995 an interest survey of the response of cutaneous *low-threshold mechanoreceptors*, i.e. the most sensitive mechanoreceptors of human body, in which the authors have studied the three areas with the higher density of these receptors: i) the palm of the hand; ii) the fingertips innervated by the median nerve; iii) the back of the hand innervated by the radial nerve, iv) the perioral region innervated by the alveolar nerve. As shown in Fig. 1.5, the survey demonstrated that the threshold force measured for the receptors located in the inferior alveolar nerves was 0.36 mN, on the contrary, those obtained for the receptors of the hand were higher (0.57 mN and 1.09 mN).

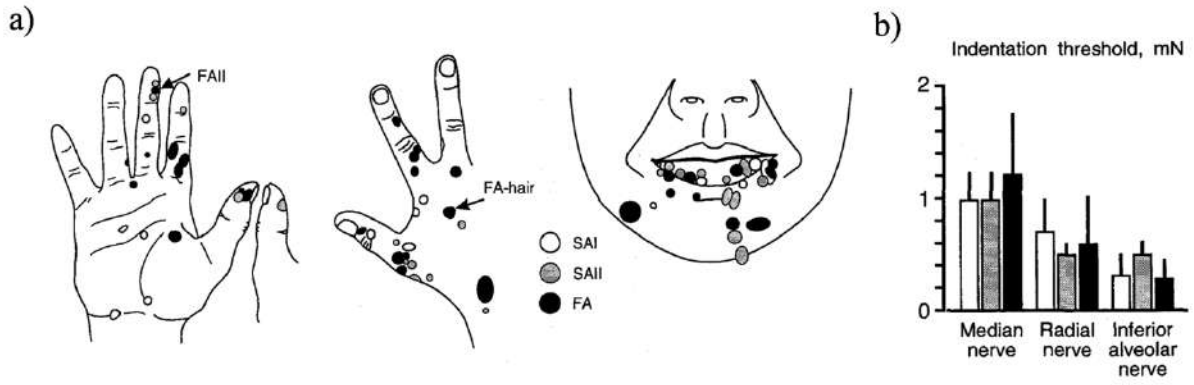

Fig. 1.5: a) Distribution of the mechanoreceptors in the median nerve, radial nerve and alveolar nerve. b) Indentation threshold of the three categories of receptors. [4]

1.4 Thermoreceptors

Thermoreception is a very complex sensory system. Thermoreceptors have, in general, a free nerve ending morphology (like Merkel cells) and they are the primary thermosensory units. They can be divided into two groups:

- Cold receptors: these thermoreceptive nerve endings have a diameter of 1.5 – 3 μm and innervate the layer between the dermis and the epidermis. They have a maximum sensitivity in the range of 25 – 30 °C
- Warm receptors: they are more superficial and smaller than cold receptors (diameter of 1 – 2 μm), so in general they innervate the epidermis. Warm receptors transduce information through nerve pulses more slowly than the cold ones. They have a maximum sensitivity in the range of 40 – 42 °C.

At constant skin temperature in the normal range (35 – 37 °C) all the cutaneous thermoreceptors generates a series of nerve impulses with a constant frequency. When the skin temperature rises, cold receptors exhibit inactivity but in warm receptors the frequency of the nerve pulses increases.

On the contrary, when the skin temperature falls, cold receptors increase the frequency of the pulses and warm receptors are inoperative (see Fig. 1.6).

Differently from mechanoreceptors, thermoreceptors have a small superficial density on fingertips (2 – 3 units/cm^2 for cold receptors and 2 units/cm^2 for warm receptors) and their density rises on lips where is of about 20 units/cm^2.

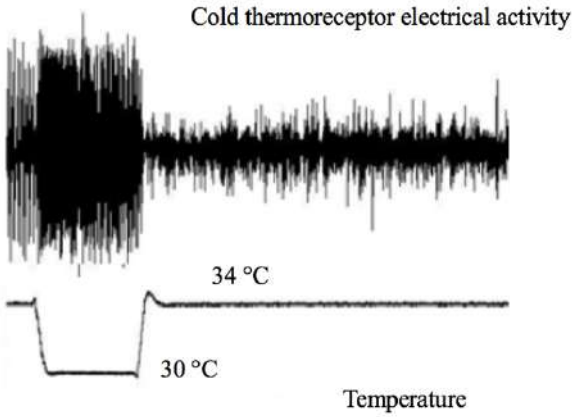

Fig. 1.6: Electrical activity of a cold receptor. At 34 °C the unit shows a regular firing, at 30 °C the unit has a increase in firing rate. [5]

Some researchers have identified a very high concentration of thermosensitive *Transient Receptor Protein Ion Channels* (TRP Ion Channel) in the epidermis [6]. It has been demonstrated that this TRP Ion Channels work as secondary thermosensory units, making the epidermis a continuous thermosensory organ. TRP Ion Channel are transmembrane proteins and typically allow an influx of different ions in a similar way to voltage-gated ion channel.

The change in ion concentration depolarizes the membrane and causes firing of action potentials. There are many subfamilies in the TRP group of Ion Channels, each of them has a specific temperature sensitivity:

- **TRPV1** is important in the detection of painful stimuli induced by noxious temperatures and by low pH, for this reason it is possible to consider TRPV1 as a polymodal receptor and with a heat threshold of about 43 °C
- **TRPV2** is similar to TRPV1, and it is selective for calcium ions influx. TRPV2 is activated by extreme heats (>53 °C).
- **TRPV3** has an activation threshold of 33 °C.
- **TRPV4** is activated between 25 °C and 34 °C.
- **TRPA1** is activated at extremely cold temperatures (<17 °C).
- **TRPM8** ion channel is activated at a wide range of cold temperatures: 8 – 28 °C. When activated, TRPM8 allows an influx of calcium ions. As well as other ions TRPM8 is also

sensitive to some chemical compounds for example menthol activates TRPM8 in the same way of cold temperatures.

The combination of TRP Ion Channels and Cold and Warm receptors provide a large range of temperature sensitivity (see Fig. 1.7). It is possible to describe the behaviour of TRP channels with the equation 1.3:

$$Q_{10} = \frac{\text{Rate (T + 10)}}{\text{Rate (T)}}, \tag{1.3}$$

in which Q_{10} is the increased of the ion flux for a 10 °C increase. Voltage gated ion channel have in general a Q_{10} value of 4, heat-activated TRP channels have Q_{10} values between 6 and 30 which is several time bigger than typical ion channels.

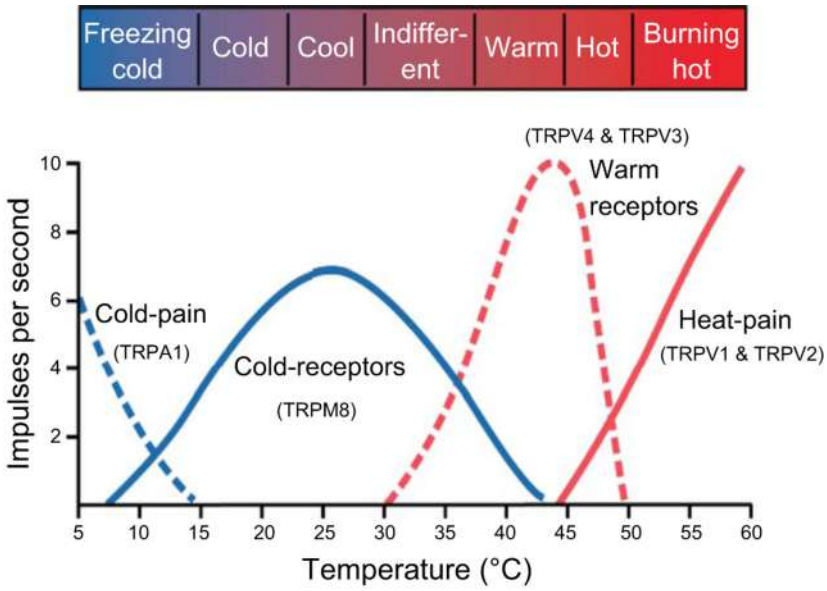

Fig. 1.7: Human range of temperature sensitivity. [7]

The surveys of Stevens et al. [8] – [9] in 1977 were fundamental to understand and explain human thermal sensibility. They reported that human can identify two warming stimuli differing by about 0.05 °C if an area of 1 cm^2 of the palm of the hand is stimulated. This thermal resolution could improve if the stimulated area is increased. Interestingly, authors have demonstrated that thermal discrimination is affected by the rate of change of the temperature: if the skin temperature change of 1 °C in a period of 20 to 30 minutes, the subject could be unaware of the shift.

1.5 Nociceptors

Nociception can be defined as the brain process of encoding pain and potential damaging stimuli. The sensitive units of nociception process are the nociceptors, which are located in any area of the

body (skin, cornea, muscle, skeletal structures, viscera etc.). There are different categories of nociceptors based on the different noxious stimuli that they can sense:

- thermal nociceptors, respond to extreme temperatures (>45 °C or <15 °C).
- Mechanical nociceptors, respond to mechanical damage such as cutting, crushing, pinching or intense pressure.
- Polymodal nociceptors, respond equally to all kinds of damaging stimuli.

Nociceptors are in general inactive and start to transmit nerve impulses when external stimuli excite them. The structural units of nocioceptors are $A\delta$ and C free nerve endings, like those specialized in thermoreception. Aδ fibers are usually divided into two categories: A-H fibers (sensitive to warm and cold) and A-M fibers (sensitive to mechanical stimuli). C fibers are associated to polymodal nociceptors and are sensitive to thermal and mechanical external stimuli.

1.6 E-Skin

As already mentioned, skin tactile receptors are excited by different external stimuli, our brain or, in general, our nervous system is able to encode the information acquired by tactile receptors and give different sensation like pressure, heat, cold, vibrations etc. The attempt to create an *artificial skin* or *electronic skin* (*e-skin*), i.e. a skin like tissue that can simulate the receptive behaviour of human skin, is motivated by the possibility to fabricate a multi-sensitive interface for different kind of applications like robotic, prosthetic etc.

Stojiljkovic and Clot presented in 1977 a superficial network of sensors called “artificial skin” based on change of resistance in a soft and elastic material [10]. This system was integrated with a prosthetic hand and was able to recognize soft material (as a cigarette) and hard material (as a metal box) when these objects were being grasped.

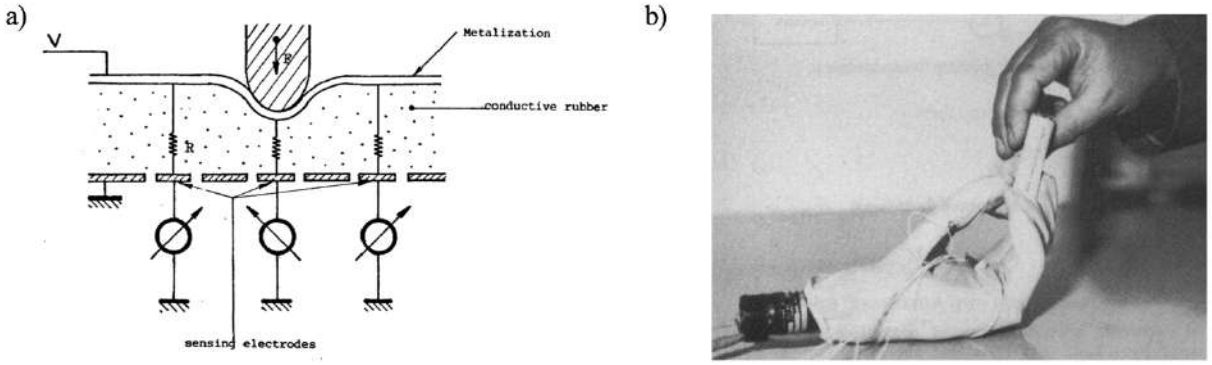

Fig. 1.8: a) Schematic of the transducer construction. b) Integration of the sensing glove with the prosthetic hand. [10]

In Fig. 1.11 is shown the number of tactile papers between 1981 and 1997, it is noticeable the increasing trend that demonstrated the rising interest of researchers and industries to this important thematic. For instance, in 80' Lumelsky, which was collaborating with General Electric, proposed a prototype of e-skin [11]. The module, shown in Fig. 1.9, contained 64 infrared sensor placed on a flexible substrate at a resolution of 25 mm and it was capable to detect objects within a distance up to about 20 cm.

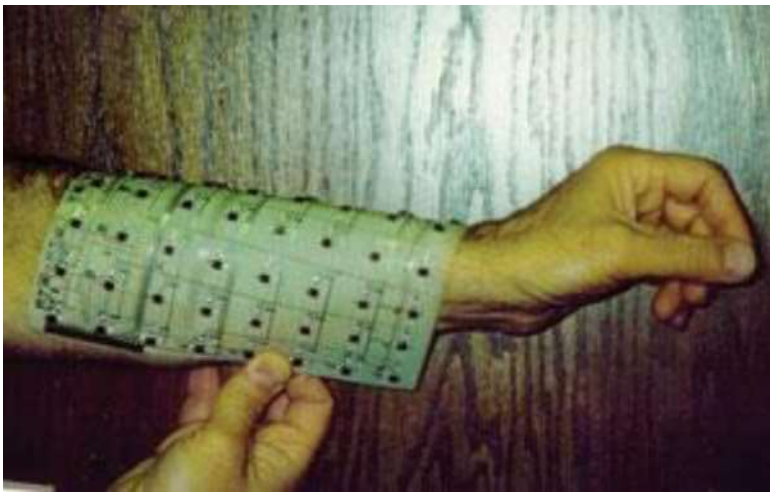

Fig. 1.9: Sensitive skin module with 64 infrared sensor pairs (LEDs and photodetectors) on a Kapton substrate. [11]

In 1985 was presented a pioneering work by Dario and De Rossi in which were evaluated and compared different approaches for tactile sensing (i.e optical sensors, conductive elastomer sensors and silicon strain gauges) [12].

Another implementation of tactile sensor for e-skin application is described in [13]. Authors fabricated a 256-element array of carbon fibers between two electrodes. Applying a voltage between the electrodes, the system was able to measure change in resistance when was stimulated with mechanical stimuli. The device was interesting because had a lifetime of about 2 million of cycle and the output showed small hysteresis.

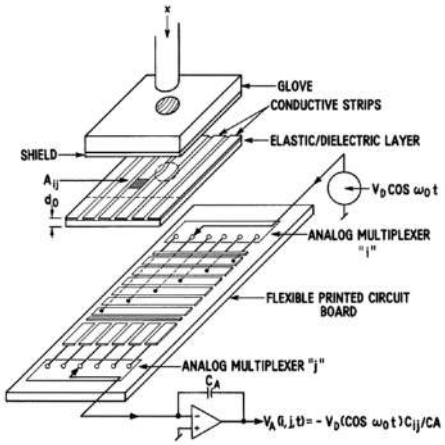

Fig. 1.10: Schematic view of a 6 x 6 capacitive touch sensors. [14]

In the same period, at Bell Labs, Boie et al. fabricated an 8x8 tactile sensor array based on the capacitive variations of mechanical stressed dielectric materials. Each element had an active area of 2.5 mm^2 and was able to measure pressure up to 5 kPa with a low special resolution imposed by the distance between the different elements [14].

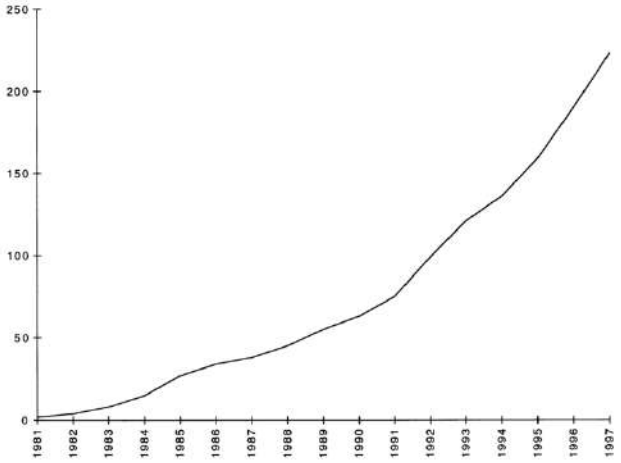

Fig. 1.11: Count of tactile papers between 1981 and 1997. [15]

In the 1990s, researchers started to use flexible electronic materials to fabricate low cost and large-area sensor for artificial skin. Jiang et al. [16] proposed a flexible shear stress sensor for e-skin application with an area of 3 cm^2 and about 100 sensors. One of the advantages of this approach was the fabrication process in which the micro-electromechanical Silicon island as small as 100 μm allows the application of the sensors on small surfaces with large curvatures.

Referring to the characteristic of human skin, already discussed in previous paragraphs, it is possible to resume the requisite of artificial skin in terms of mechanical requirements and thermal requirements:

artificial mechano receptors characteristics

- spatial resolution, fingertip >140 units/cm^2.
- Force resolution, ~1 mN.
- Force range, [0.001 – 10] N.
- Bandwidth, [0 – 1000] Hz.
- Response time ~1 msec.

Artificial thermo receptors characteristics

- spatial resolution, lips >20 units/cm^2, other parts 5 units/cm^2.
- Thermal resolution, ~0.02 °C.
- Temperature range, [0 – 55] °C.
- Temperature variation range, 1 °C/min.

Besides the sensing properties described in previous paragraphs, artificial skin should have specific mechanical properties in order to mimic the mechanical behaviour of the human skin layers.

Some interesting works [17] – [18] have demonstrated that the *Young's modulus* of the skin, *E*, varies between 0.42 MPa and 0.85 MPa for torsion tests, 4.6 MPa and 20 MPa for tensile tests and it is well known that the skin is stretchable up than 70% strain [19] and, consequently, has the capability to be adapted to the movements of human's body by bending and stretching.

Flexible and stretchable electronics [20] allows the fabrication of devices able to be bent and to be accommodated over irregular surfaces such as elbows and knees. Notable progress has been obtained in this research field in recent years: Lacour et al. [21] proposed an approach for the realization of stretchable interconnects for 3D electronic circuits, made of gold deposited and patterned on elastomeric substrates, that can be stretched up to 10% remaining electrically continuous.

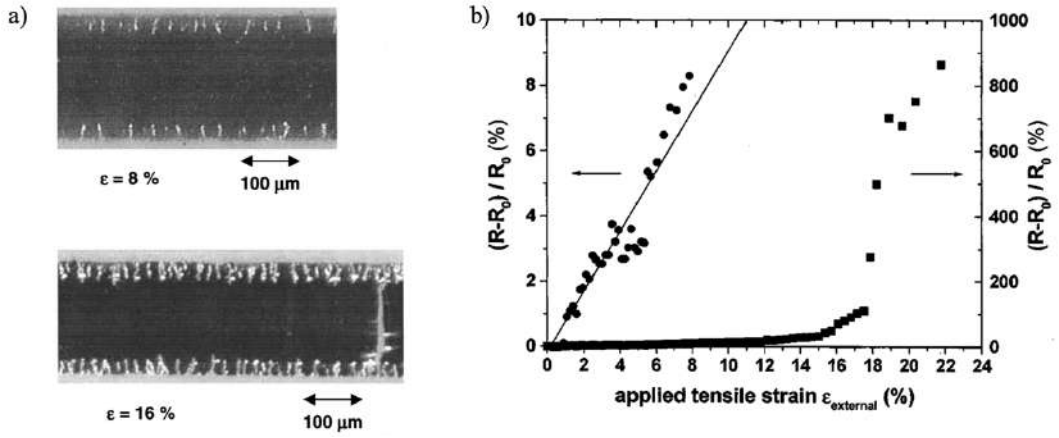

Fig. 1.12: a) Photographs of a 100-nm-thick Au stripe on PDMS substrate under 8% and 16.4% tensile strain. b) Variation of the normalized change in electrical resistance of the stretchable gold conductor with applied tensile strain. [21]

Roger's group, by exploiting materials with suitable mechanical properties that are able to mimic the mechanical properties of the skin, proposed an approach that led to the development of a variety of conformable "epidermal electronic systems". These systems showed an excellent adhesion to skin, and consist in the integration on the same ultra-flexible and conformable substrate of different kinds of electronic devices (sensors, light-emitting diodes, photodetectors etc.) [22].

In addition, *organic electronics* may represent a valid candidate for the realization of tactile devices, thanks to its great potential for large area fabrication techniques and the possibility of using flexible, stretchable and ultrathin materials.

The problematic of using organic materials is the large variability of their biocompatibility [23]. In general, elements such as chemical composition and pH can influence *cytotoxicity*, i.e. the

quality of being toxic to cells. For these reasons, many different natural materials as starches, gelatin, DNA molecules etc. have been used as substrates or dielectrics or active materials for the fabrication of electronic devices. In last years, also the employment of resorbable have been investigated. In fact, this could be a practical solution not only for the possible fabrication of artificial skin systems, but also for many different kinds of bioelectronics applications.

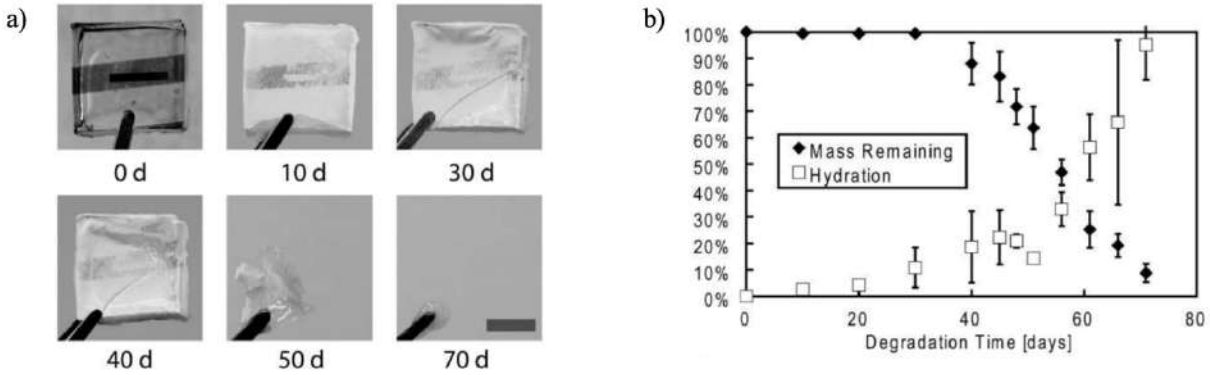

Fig. 1.13: a) Photographs from representative devices at various stages of the degradation time. b) Plot of mass remaining and water uptake by mass (hydration). [24]

In particular, Bettingen and Bao proposed a resorbable OFET fabricated on a biocompatible and biodegradable PLGA (poly l-lactide-co-glycolide) substrate. The advantages of using this kind of materials is that the devices can be dissolved after a tunable specific period of time [24].
To summarize, additional characteristics of artificial skin can be recap in Table 1.1:

Mechanical characteristics	***System's characteristics***
Flexibility	High sensitivity
Conformability	Reliability
Biocompatibility	Low cost technology
Softness	Low power dissipation

Table 1.1: Mechanical and System characteristics of artificial skin.

Bibliography

[1] C.L. Stanfield, "*Principles of Human Physiology*", Pearson, 2012.

[2] M.D. Binder et al. "*Encyclopedia of Neuroscience*", Springer, 2009.

[3] E. R. Kandel et al. "Principles of neural science", McGraw-Hill, 2000.

[4] B. B. Edin et al. "*Receptor encoding of moving tactile stimuli in Humans. I. Temporal pattern of discharge of individual Low-Threshold Mechanoreceptors*", The Journal of Neuroscience, January 1995, 15(1) pp. 830-847.

[5] M. Campero et al. "*Unmyelinated afferents in human skin and their responsiveness to low temperature*", Neurosciences Letters, 2010, pp. 188-192.

[6] J. A. Boulant, "*Physiology and Pathophysiology of temperature regulation*", World Scientific Publishing Co., 1998.

[7] A. C. Guyton et al. "*Textbook of Medical Physiology (13th ed.)*", Elsevier Saunders, 2011.

[8] J. C. Stevens et al. "*Regional sensitivity and spatial summation in the warmth sense*", Physiologic Behaviour, 1974, (13) pp. 825-836.

[9] J. C. Stevens et al. "*Subjective warmth in relation to the density, duration and areal extent of infra-red irradiation*", ASHRAE Transaction (Part 1), 1973, (76) pp. 110-112.

[10] Z. Stojiljkovic et al. "*Integrated behaviour of artificial skin*", IEEE Transaction on Biomedical Engineering, 1977, 24 (4) pp. 396-399.

[11] V. J. Lumelsky et al. "*Sensitive skin*", IEEE Sensors Journal, June 2001, vol. 1 (1).

[12] P. Dario et al. "*Tactile sensors and the gripping challenge: Increasing the performance of sensors over a wide range of force is a first step toward robotry that can hold and manipulate objects as humans do*", 1985, IEEE Spectrum, vol. 22 (8).

[13] B. E. Robertson et al. "*Tactile sensor system for robotics*", Robot Sensors, 1986, vol. 2 pp. 89-97.

[14] R. A. Boie, "*Capacitive impedance readout tactile image sensor*", Proceedings of International Conference of Robotics, 1984, pp. 370-378.

[15] M. H. Lee et al. "*Tactile sensing for mechatronics – a state of the art survey*", Mechatronics, 1999, pp. 1-31.

[16] F. Jiang et al. "*A flexible MEMS technology and its first application to shear stress sensor skin*", International Proceedings of IEEE MEMS, 1997, (155) pp. 335-350.

[17] P. G. Agache et al. "*Mechanical properties and Young's modulus of the human skin in vivo*", Archives of Dermatological Research, 1980, 269 (3) pp. 221-232.

[18] J. F. Manschot et al. "*The measurement and modelling of the mechanical properties of human skin in vivo. I. The Measurement*", Journal of Biomechanics, 1986, 19 (7) pp. 511-515.

[19] C. Edwards et al. "*Evaluation of biomechanical properties of human skin*", Clinics in Dermatology, July-August 1995. 13 (4) pp. 375-380.

[20] T. Yamada et al. "*A stretchable carbon nanotube strain sensor for human motion detection*", Nature Nanotechnology, March 2011, (6) pp. 296-301.

[21] S. P. Lacour et al. "*Strechable gold conductors on elastomeric substrates*", Applied Physics Letters, April 2003, vol. 82 (15).

[22] D. H. Kim et al. "*Epidermal electronics*", Science, August 2011, vol. 333 (6044).

[23] M. L. Hammock et al. "25th Anniversary Article: The evolution of electronic skin (E-Skin): A brief history, design considerations, and recent progress", Advanced Materials, 2013, (25) pp. 5997-6038.

[24] C. J. Bettinger et al. "*Organic thin-film transistors fabricated on resorbable biomaterial substrates*", Advanced Materials, 2010, vol. 22 (5).

2 Tactile sensors: state of the art

In this Chapter there will be a detailed analysis of the state of the art of the most employed approaches for the realization of tactile transducers, underling for each approach the advantages and disadvantages.

2.1 Capacitive tactile sensors

A capacitive sensor takes advantages of the structure and the working principle of capacitors. As shown in Fig. 2.1, this type of sensors consists of two metallic, or conductive, plates with a dielectric material in between. Capacitance can be expressed with Equation 2.1 in the common case of parallel plate capacitors:

$$C = \varepsilon_0 \varepsilon_r \frac{A}{d}, \tag{2.1}$$

where ε_0 and ε_r are respectively the permittivity of the free space and the relative permittivity of the dielectric, d is the distance between the two conductive plates and A is the area of the plates. In the case of pressure sensors, a variation in d, due to an applied normal pressure on the structure, can change the value of the capacitance C, if the reduction of the distance between the plates is large enough. Furthermore, changes in A are typically used to sense *shear forces*.

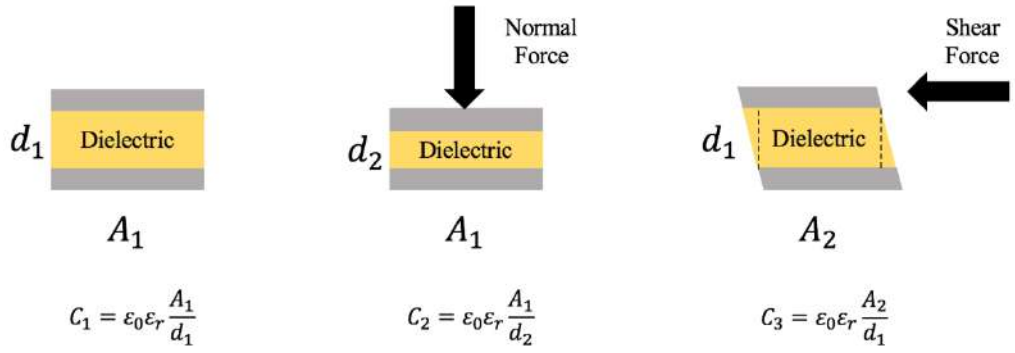

Fig. 2.1: Capacitive device for transducing sensory stimuli in skin.

Capacitive sensors are generally used in different applications like prosthetic and robotics thanks to their simple architecture and the possibility to achieve high spatial resolutions [1] – [3]. For this kind of sensors, the choice of the dielectric is fundamental to optimize their sensitivity. In particular, elastomers have the property of a high elasticity and deformability, with an elastic

modulus typically two orders of magnitude lower than that of silicon, and high yield strain [4]. For this reason, these polymers are widely used as an alternative to dielectric inorganic material.

An interesting approach has been proposed by Vandeparre et al. [5]. In this work a conformable capacitive pressure sensor is fabricated by using a particular elastomeric foam dielectric and stretchable electrodes. The dielectric used is a flexible, microcellular *polyurethane* (PU) foam with ultrathin gold electrodes evaporated on it. This particular foam structure of the dielectric allows the sensors to be stretched, thus maintaining stable the electrical conduction properties of the metal film (see Fig. 2.2). The fabrication procedure is very simple; a two-component mixture of PU foam (Smooth-on Flex-Foam-iT) is bar coated on a glass carrier. After 2 hours of crosslinking at room temperature, the top and bottom surfaces of the foam are coated by a patterned, with a shadow mask, metal structure in order to obtain an array of 25 nm thick gold electrodes, with an area of 1 cm^2 for each sensor.

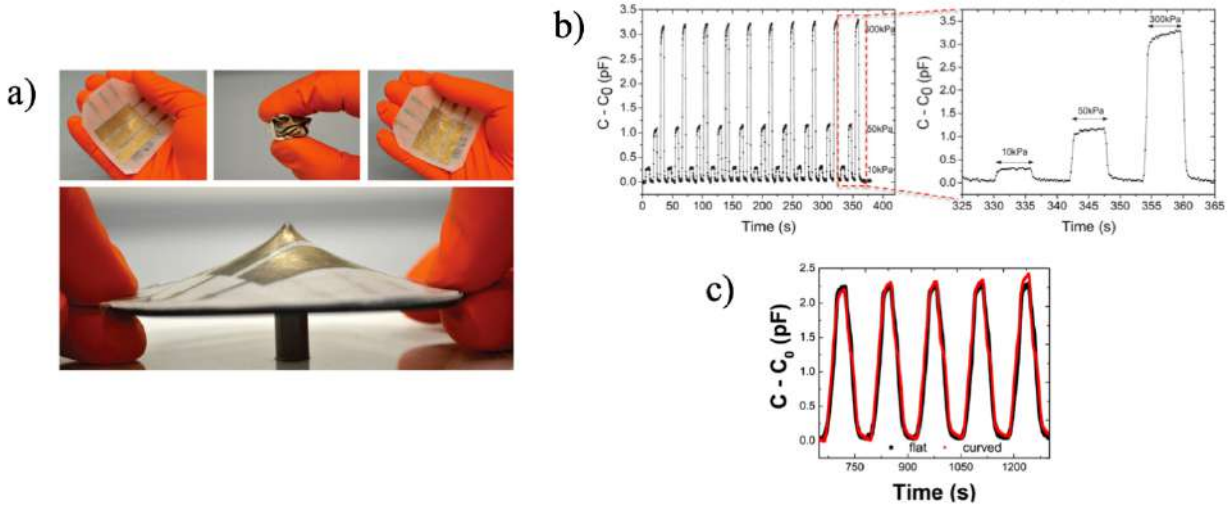

Fig. 2.2: a) Pictures of a matrix with a 3 x 3 sensors, the structure can sustain crumpling as sharp indentation. b) Change in capacitance for 3 different pressure. c) Change in capacitance during before (black line) and during (red line) a 75% compressive strain. [5]

Fig. 2.2 shows the structure and the response of the proposed structure. The device is able to detect pressure variations from 10kPa to 300kPa with a good reproducibility and is able to work even after a wide strain (~75%). The main drawback of the proposed approach is that employing a pattering through a shadow mask does not allow achieving the typical high resolutions requested for mechanical sensors for tactile applications.

A different solution has been presented by Hu et al. [6] who developed a flexible capacitive sensor for the detection of strain and pressure. The most important advantages of this approach is the use of highly compliant materials for the fabrication of electrodes, made of a composition of ultrathin silver nanowires (AgNws) over an elastomeric polyurethane substrate. In this case the PU is not used as dielectric, but as a carrier of the electrodes and the sensitive material. One more

very interesting feature of this devices is that the electrodes are also completely transparent (see Fig. 2.3b).

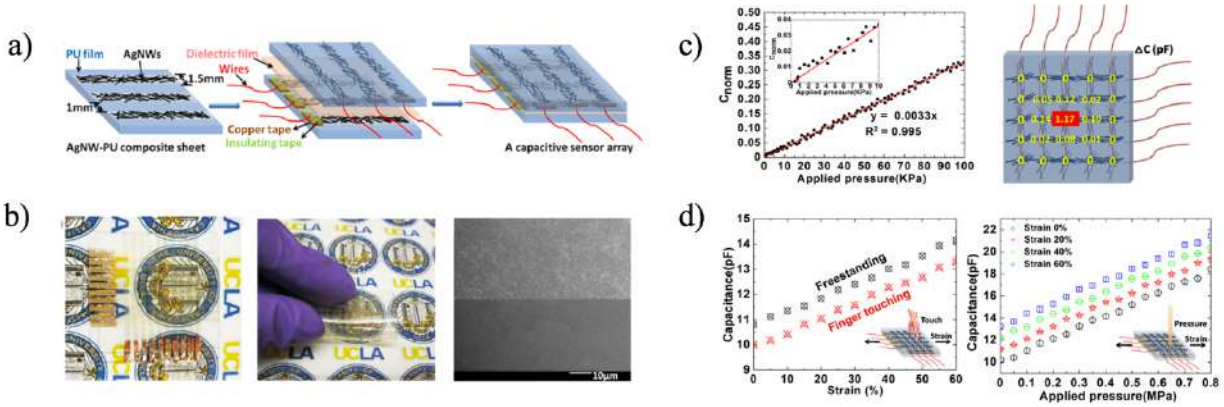

Fig. 2.3: a) Schematic illustration of the fabrication procedure of the capacitive array. b) Image of a matrix with 10 x 10 transparent sensors and SEM images at the interface between AgNW and PU. c) Change of capacitance due to an applied pressure and mapping of the measured capacitance changes where a pressure was applied on the central sensor. d) Change in capacitance combined with figure touch versus uniaxial stretching strain and change in capacitance versus independently applied transverse pressure and uniaxial elongation. [6]

Silver nanowires were deposited by spray coating through a contact mask over a glass substrate and then annealed for 30 minutes at 190 °C. PU liquid compound (Clear Flex®) was dropcasted over the AgNW on glass substrate. The resulting AgNW-PU composite sheet was peeled off and the sensors were fabricated by an elastomeric dielectric between two AgNW-PU composite electrodes with the conducting surface inward. As shown in Fig. 2.3c, if there is a mechanical stimulation of the central sensor in a matrix of 10 x 10 pixels, the change of the capacitance of the addressed pixel is several times bigger than the neighboring sensors. Authors have demonstrated that this kind of approach can allow detecting pressures variation in the range of 1kPa to 100kPa, the typical pressure range of soft touch, hand grip and finger press with a spatial resolution of 1.5 mm^2.

An original and interesting work, presented by Mannsfeld et al. [7] in 2010, has demonstrated that it is possible to increase the sensitivity of an elastomer based capacitive sensor acting on its structure. Elastomers can be considered as “rubber-like” polymers and, consequently, have the well known problems associated with visco-elastic behaviour of rubbers. In this work, authors have demonstrated that microstructuring the framework of an elastomeric material (*polydimethylsiloxane* or PDMS) it is possible to overcome the already mentioned problems and also to minimize the relaxation time of the capacitors after compressions. The fabrication process of the capacitive sensor started with the deposition of the solution of the PDMS, that it was deposited through drop casting technique onto a Silicon wafer mould containing replicas of the inverse of the dielectric structure required. An *indium tin oxide* (ITO) coated over a flexible

poly(ethyleneterephthalate) (PET) sheet was laminated and pressed to the mould and the PDMS was cured at 70 °C for 180 minutes, and it acted as top electrode. After the curing process, the PET substrate with the PDMS structure was peeled off the Silicon wafer. The bottom electrode was a patterned aluminium film deposited over a flexible PET film. In this work, were tested three different types of PDMS structures: pyramidal, linear and planar (unstructured). The experimental results are given in Fig. 2.4: the structured PDMS (pyramidal and linear) exhibit a higher sensitivity than the unstructured one with the same thickness, especially for pressure values >0.5 kPa. The pressure sensitivity is the slope of the curves and it can be written as:

$$S = \frac{\delta\left(\frac{\Delta C}{C_0}\right)}{\delta p}, \tag{2.2}$$

where ΔC is the variation of capacitance under an applied pressure, C_0 is the capacitance in the resting state and δp is the applied pressure. All the types of structures have negligible hysteresis and can be cycled more than 1000 times. However, the relaxation time of the three types of proposed sensors are wide different: in the specific case of unstructured film, relaxation time is more than 10 seconds which makes it unsuitable for tactile applications. On the contrary, those registered for structured films are in the range of few millisecond, typically the range of requested for e-skin applications. The reasons of these different behaviour can be explained referring to the different configurations of PDMS dielectrics: structured films have air hole between the elastomer texture, consequently there is far less elastic resistance in this type of capacitors. Another interesting explanation is that, when structured capacitors are compressed, the total volume of displaced dielectric much higher than those in unstructured capacitors, due to the presence of air gaps. Therefore, the reduction of the distance between the bottom and top electrodes is higher in the first type of structure. Authors have also demonstrated that this kind of capacitors can detect very small loads as 3 Pa, so they can be used for sensors area that require high sensitivity and resolution for very low pressure. On the contrary, the sensitivity in medium-high pressure range is very low.

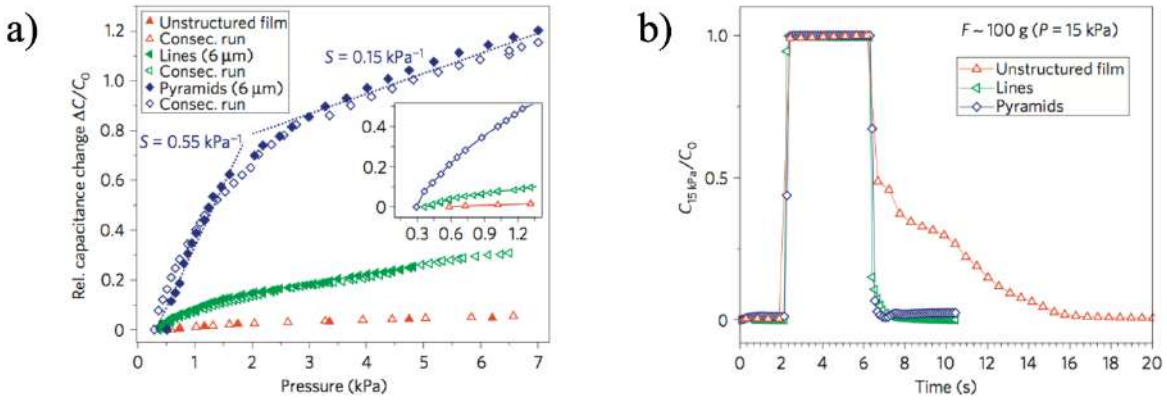

Fig. 2.4: a) Change in capacitance for different types of microstructured PDMS films and their relative sensitivity. b) Relaxation and resting-state curves for pyramidal, linear and unstructured films. [7]

2.2 Resistive tactile sensors

The working principle of resistive sensors is based on the modulation of the resistance of a particular material due to pressure stimulation (*piezoresistive* sensors) or due to temperature stimulation (*thermistors* and *RTD sensors*). Piezoresistive sensors are typically a pressure sensitive element as conductive polymers or elastomers. Resistive temperature sensors usually exploit the temperature dependence of classic metals or conductive polymers too. According to Equation 2.3, resistance modulation can be easily detected by an electrical measuring system thanks to the voltage current characteristic of a simple resistive element:

$$V = RI, \tag{2.3}$$

where R is resistance, V the applied voltage across the resistance and I the measured current. The change in resistance can be affected by different factors as:

- variations in contact resistance (R_C) between two conductive elements.
- Variations in the geometry (length or width) of the sensing element (especially for strain sensors).
- Variations in the resistivity of a semiconductor due to a modification in its band structure.
- Variations in the resistivity (ρ) of a conductive element, due to a temperature stress.
- Variations in the percolating/tunnelling mechanism in amorphous polymers (e.g. PDMS) loaded with conductive particles or in CNTs.

Resistive devices have the advantages of requiring less readout electronic complexity and are less susceptible to noise than capacitive sensors. However, the power consumption is much high and they have a lower frequency response [8].

2.2.1 Piezoresistive tactile sensors

Variations in contact resistance (R_C) depends on changes in contact area between two conductive elements due to an external applied pressure. This phenomenon, is governed by Equation 2.4 [9]:

$$R_C \propto F^{-1/2} \tag{2.4}$$

In literature it has been demonstrated that sensors based on contact resistance are advantageous thanks to their high sensitivity especially at low pressure, to their large working range, low temperature sensitivity and fast responses [10]. In Dabling et al. [11] is reported an interesting study of the behaviour of these kind of sensors: authors have demonstrated that their performances can suffer of hysteresis, drift and loss of sensitivity.

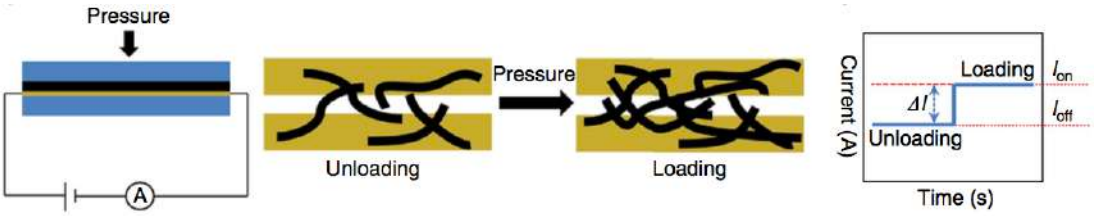

Fig. 2.5: Schematic illustration of the AuNWs sensor based and current changes in responses to external pressure. [12]

Gong et al. [12] proposed an wearable pressure sensor based on gold nanowires (AuNws). The device can achieve a high sensitivity (>1.14 kPa^{-1}), a fast response time with a good stability. The sensing mechanism is related to the contact resistance of the AuNWs which were sandwiched between two interdigitated arrays: in particular, when a pressure is applied on the device, the number of AuNWs bridging top and bottom electrodes increase and consequently the contact resistance decrease (see Fig. 2.5).

In the last decade, the combination of different materials, for example composites based on conductive fillers dispersing into a non-conducting polymer matrix, are attracting more attention for many applications because of their unique electrical and mechanical properties: for instance, in Abyaneh et al. [13] is reported the piezoresistive behaviour of Zn-PDMS composite, authors have demonstrated that with this kind of composite is possible to obtain high change in resistance under uniaxial pressure due to variation of the tunnelling effect between the Zn particles.

Interesting result are shown in [14] where Dang et al. presented the study of the piezoresistive behaviour of multiwall carbon nanotubes (MWCNTs) dispersed into a silicone rubber. One of the main aspect of this survey is that the sensitivity of the composite can be tuned by changing the concentration of MWCNTs.

Very recently, Takao Someya's group reported a transparent bending-insensitive pressure sensor based on composite nanofibers of CNTs and graphene dispersed into a fluorine rubber [15]. The fabrication process is based on an electrospinning process, in order to reduce the the rigidity

and the total thickness of the pressure sensor, of a mix of fluorinate copolymer, CNTs and graphene. The solution was deposited over different flexible plastic substrates. The bending-insensitive behaviour is related to the nanofibrous structure that can change its alignment and follow perfectly the deformation, thus minimizing the strain in the singles fibres. Authors have deeply investigated the individual role of CNTs and graphene in the mixture.

They have demonstrated that a simple mixture of CNTs and the fluorinated copolymer could be use as pressure sensor but shows a very low sensitivity. On the contrary, a mix of the copolymer and graphene can not be used as conductor or as pressure sensor. Only the composite of both CNTs and graphene can achieve a high sensitivity as pressure sensor. The working principle is based on the modulation of the conductivity of the sample due to the formation of conductive paths into the sensor's framework. The device, thanks to its low thickness (∼1.4μm) can be accommodated onto the surface of the human skin and can detect and monitor the pressure distribution, especially in the low-range [0.6 – 1.5] kPa.

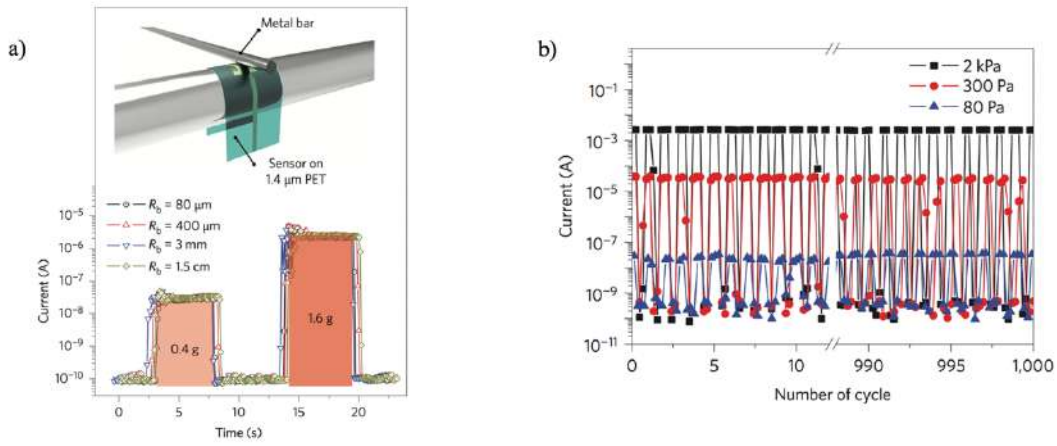

Fig. 2.6: a) Piezoresistive esponse of the device for different normal forces (0.4 and 1.6 g). b) On/off cyclic test of the sensor at different pressures. [15]

Strain sensors have been used in many areas such as robotics, biomedical application, bioengineering, wearable devices etc. The transduction mechanism is based on the variation of resistance of a material due to a modification in its structure caused by a strain stress. In general, the sensitivity of a strain sensor is referred to as the *gauge factor* (GF) defined as:

$$\mathrm{GF} = \frac{\Delta \mathrm{R}}{\mathrm{R}_0 \varepsilon}, \tag{2.5}$$

where ΔR is the variation of the initial resistance R_0, and ε is the strain. Recently, it has been demonstrated that, by using strain sensors based on composite materials, it is possible to increase the value of their gauge factor.

For instance, Xiao et al. [16] proposed a high GF strain sensor based on ZnO nanowire/polystyrene on a PDMS film. This particular incorporation of ZnO as conductive material has led to obtain a GF value of 116, which is comparable to those of traditional inorganic strain sensors. However, the high initial resistance ($R_0 \approx 10$ GΩ) leads to use an high precision instrument thus strongly limiting the real employment of this approach in practical applications.

Recently, Gong et al. [17] presented a high strain sensor composed of polydimethylsiloxane (PDMS) and polyaniline (PANI) for various applications such as tactile strain sensor. The working mechanism and the response of the sensor is shown in Fig. 2.7. Authors explain that the variation of resistance during the strain is affected not only by the deformation of the PANI film (variation of geometry parameters l and w) but also by the formation and modification of micro-cracks in the sensor structure. The obtained GF (54 at 50% strain) is higher than other reported flexible sensor, and the proposed approach does not require a complex measurement system due to the high value of the measured current (≅ mA) at 1 V.

Piezoresistivity is also related to a change in chemical bonds in different materials [18]. In Bae at al. [19] is presented a piezoresistive strain sensor based on graphene fabricated on very thin, flexible plastic. The graphene was grown by chemical vapour deposition (CVD) and patterned by standard photolithography and by reactive ion etching (RIE).

The device was able to sense tensile strain up to 7% and it is completely transparent thanks to the optical property of graphene. However, experimental results have shown a strong non-linear behaviour for strains higher than 1.8%. Authors explain this phenomenon referring to the structure of graphene: the existence of two different piezoresistive regions is due to the formation of micro-craks and defects for strains >1.8%. On the contrary, in the linear region, the working mechanism is related to a modification of the carbon-carbon bond length during stretching.

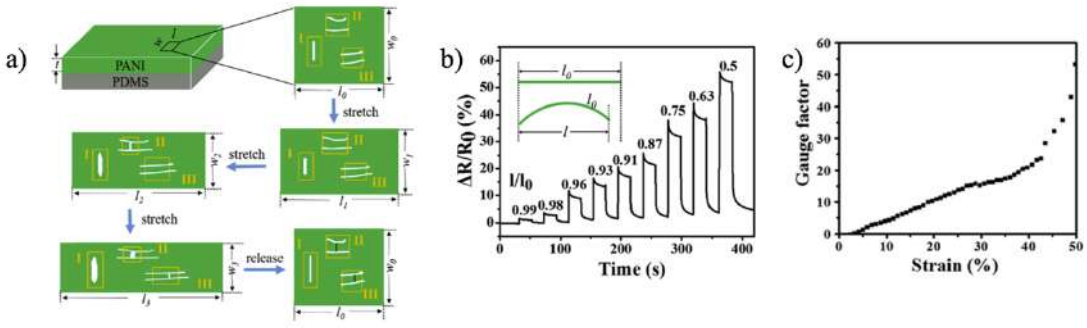

Fig. 2.7: a) The working mechanism and changes in structure of the strain sensor. b) Relative change in resistance under bending conditions. c) Gauge Factor of the sensor under different strains. [17]

2.2.2 Pyroresistive tactile sensors

In the state-of-the-art of temperature sensors, resistors whose electrical resistance greatly depends on the temperature are of great interest. These sensors are usually divided into two categories: thermistors and RTD sensors. RTD have a larger range of detectable temperature, they are made of pure material, in general a metal, and they generally show a linear output characteristic.

The work by Mattana et al. [20] represented an innovative step in the fabrication of RTD flexible sensors. In this works authors presented two temperature sensors fabricated with different techniques: gold resistors by standard photolithography and inkjet-printing). In both cases the sensors are able to detect temperature variations in the range between 10 °C and 80°C. Roger's group have developed a conformal resistive device for thermal characterization of human skin [21]. The ultrathin (∼1.2 μm) and compliant structure of the presented sensor permit to minimize the strain sensitivity of the device and to maximize the adhesion to the skin.

Thermistors have a non-linear characteristics and are usually made by polymers or ceramics with a particular piezoresistive behaviour: negative (NTC) or positive (PTC) temperature coefficient. The relationship between the measured resistance and the temperature change can be expressed as:

$$R(T) = R_0(1 + AT + BT^2 + CT^3), \tag{2.6}$$

where T represents the temperature in °C and R_0 is the value of the resistance at T = 0 °C. For small temperature variation ΔT around T, this relation can be linearized as follows:

$$R(T + \Delta T) = R(T)(1 + \alpha_T \Delta T), \tag{2.7}$$

where $\alpha_T = \frac{1}{R(T)}\frac{\Delta R}{\Delta T}$ is the sensitivity (Temperature Coefficient of Resistance, TCR) of the sensor in units of °C.

In addition to good reliability and reproducibility of temperature sensors, a good linearity of the temperature dependent resistance and high sensitivity are generally required.

Dankoco *et al.* [22] reported a thermistor developed to achieve surface temperature measurement of the human body. The device must be supplied under a bias voltage of 1 V and presents a high nominal resistance. The device is composed of silver deposited on a Polyimide substrate (Kapton HN). The temperature sensor has a sensitivity of 2.19×10^{-3} °C^{-1} obtained in the typical range of tactile applications [20 – 60] °C and a nominal resistance of 2.032 kΩ at 38.5 °C.

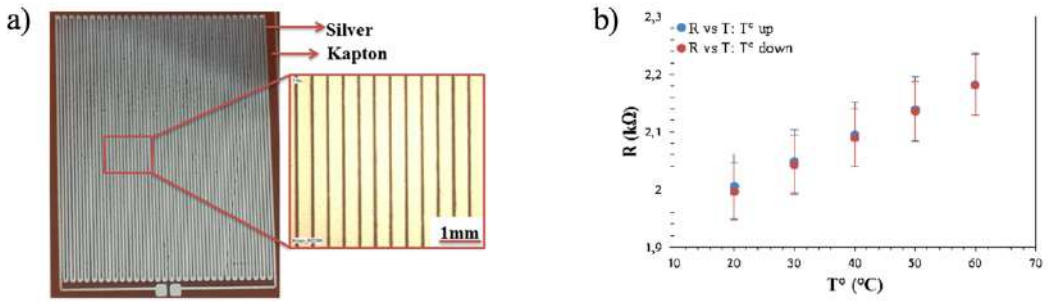

Fig. 2.8: a) Silver thermistor over a flexible Kapton substrate. b) Changes in resistance with temperature variations. [22]

Very recently an another example of skin-mountable temperature sensor has been presented by Vuorinen *et al.* [23]. The devices, shown in Fig. 2.9, were fabricated with inkjet-printed graphene/PEDOT:PSS ink on top of a skin-formable bandage like substrate, which also provides good adhesion to skin. Using this approach, authors managed to obtain a device which has the possibility to monitor temperature changes directly on human skin with a TRC value higher than 0.06%°C under optimal conditions [35 – 45] °C. Even if this device does not yet compete in terms of sensitivity with already existing temperature sensors it could be used in its present form as a simple fever indicator on human skin. This is due to the simple fabrication process, which enables low-cost fabrication of epidermal electronics with the added value of disposability. Scalable and simple manufacturing process combined with the stretchable, functional materials makes it possible to manufacture epidermal temperature sensors, which are comfortable to use with an excellent skin/device interface.

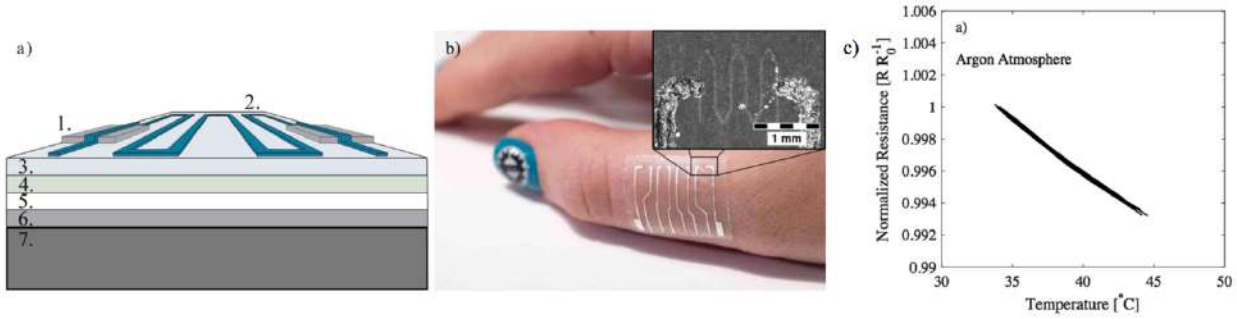

Fig. 2.9: a) Multilayer device structure, 1- silver conductors, 2- graphene/PEDOT:PSS temperature sensors, 3- PU substrate, 4- adhesive layer, 5- protective paper, 6- PET film, 7- cooling/heating element. b) Photograph of the device on human skin. c) Change in resistance in argon atmosphere. [23]

Another interesting approach has been reported by Zhenan Bao's group [24]. In this work they presented a Ni microparticle-filled binary polymer composite, used as temperature sensor. This material showed a much higher sensitivity than other types of flexible thermoresistors based on amorphous polymers. The resistivity of this composite material is affected by the temperature, but

the strong PTC effect is limited in the range between 35 °C and 42 °C which makes the device particularly suitable for human body temperature.

2.3 Piezoelectric and pyroelectric tactile sensors

The words *piezoelectricity* and *pyroelectricity* find their etymological origin in the ancient Greek words "πιεζω" and "πυροζ" which means respectively "to press" and "fire" and "ελεζτρον" (electron) which was the word associated to those materials known for their electrostatic property. Piezoelectricity and pyroelectricity are the abilities, of some materials, to generate a voltage in response to an applied force or a temperature variation.

The piezoelectric effect can be described by a linear relationship between the *electric displacement* **D**, the *piezoelectric coefficient* **d** and the applied mechanical stress σ:

$$D_i = d_{im}\sigma_m. \tag{2.8}$$

On the other hand, the pyroelectric effect is related with the external thermal stress **ΔT**:

$$D_i = p_i \Delta T, \tag{2.9}$$

where **p** is the *pyroelectric coefficient* defined by Equation 2.10:

$$p_i = \frac{\partial D_i}{\partial T}. \tag{2.10}$$

Even if the first reference to pyroelectric effect can be founded in writings of Theophrastus in 314 BC, research became more precise not before the 19th century with Sir Brewster and brothers Curie. But only after the studies of Voigt on the physical crystallography of materials, published in 1910, it was clear the relationship of piezoelectric and pyroelectric effect in materials without a centre of symmetry in their structure.

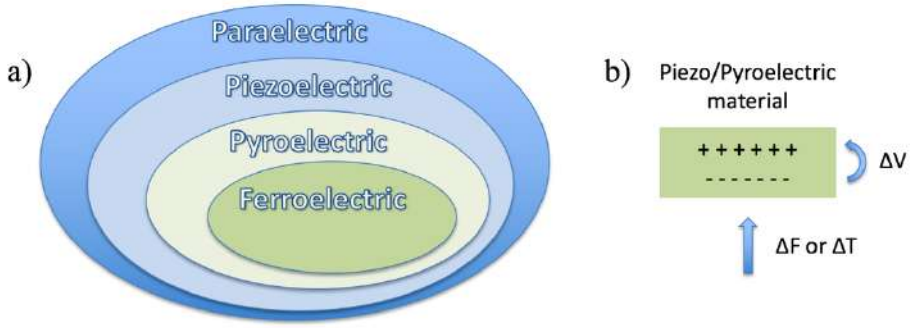

Fig. 2.10: a) Schematic representation of different classes of solid materials. b) Piezoelectric/pyroelectric response under a specific external stress.

Solids are characterized by a three dimensional arrangements of atoms, generally locked into their positions. A *crystalline solid* is a material which has a repetitive structure in the three dimensions (x, y, z) with a long range order and has different physical properties in different directions

(*anisotropy*). On the other hand, an *amorphous solid* does not present a long range order in its structure and has the same physical properties in all the directions (*isotropy*).

Crystalline solid can be divided into 32 crystal classes or into 6 crystal system (*triclinic system*, *monoclinic system*, *orthorhombic system*, *tetragonal system*, *hexagonal system*, *isometric system*). Only 21 crystallographic classes are non-centrosymmetric and shows the piezoelectric effect, except for the isometric class 432 in which the piezoelectric charges along the <111> axes cancel each others. Among the piezoelectric crystal classes, ten show also the *pyroelectric* effect: these crystals contain a non-zero polarization when a temperature variation induced changes of the total dipole moment. Over a certain temperature T_C (called the *Curie temperature*), the pyroelectric effect vanishes, and the crystals transform into the *paraelectric* state. As shown in Fig. 2.10, only few pyroelectric classes have the *ferroelectric* property i.e. the characteristic of some pyroelectric materials to have a *spontaneous* polarization that can be reversed by an external electric field. Piezoelectric and pyroelectric materials can be classified into three categories:

- crystals: *triglycine sulphate* (TGS), *lithium tantalate* ($LiTaO_3$) etc.
- Ceramics: *lead-zirconate titanate* (PZT) etc.
- Polymers: *polyvinyl fluoride* (PVDF) and its copolymers (PVDF-TrFE) etc.

if compared to resistive devices, the advantages of using a piezoelectric/pyroelectric sensors are that these materials exhibit a good high-frequency response and a high sensitivity [8]. However, these sensors can not work over their Curie temperature T_C and have unreliable static sensing properties.

In Khan et al. [25] is presented a pressure sensor for artificial skin application, based on a piezoelectric polymer, *polyvinylidene fluoride-trifluoroethylene* (PVDF-TrFE), over a thin polyamide (PI) substrate. The device consisted in 4x4 sensitive elements made by sandwiching the PVDF-TrFE between two conductive silver plates. The fabrication process started from the deposition of the bottom silver electrode by screen printing. Then, the sensitive elements were deposited over the bottom electrodes by screen printing or spin coating and sintered for 4 hours at 130 °C. After that, the silver top electrodes were patterned on the piezoelectric polymer. Piezo/pyroelectric polymers ad PVDF and PVDF-TrFE need a polarization (or poling) process, through a high voltage across the polymer, in order to introduce and increase their piezo/pyroelectric behaviour. The amplitude of the voltage depends on the thickness of the polymer to be poled: in literature is reported that are required 100 V/μm at room temperature or 70 V/μm at 80 °C [26]. As shown in Fig. 2.11, the device were tested at different frequencies and different force values (from 0.5 N to 4 N). The output voltages have the same quasi linear behaviour for screen printed and spin coated sensors. Furthermore, screen printed sensors shown

a higher sensitivity and authors explain that it could depends on the different thickness and uniformity obtain for spin coated sensors.

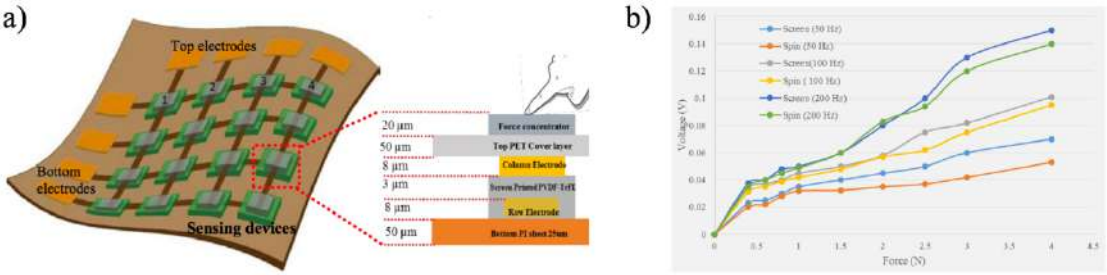

Fig. 2.11: a) Schematic illustration of the 4x4 sensor array. b) Piezoelectric response of spin coated and screen printed PVDF-TrFE. [25]

In a different work Yang et al. [27] presented the first application of a ceramic lead-zirconate titanate (PZT) pyroelectric nanogenerator (PNG) for detecting the temperature of a finger tip. The innovation of this approach is based on the use of an energy harvesting self-powered nanotechnology that provide the power instead of an external battery or supply systems. The PZT micro/nanowires were obtained from the bulk PZT by mechanical method, then a single micro/nanowire was fixed on a glass substrate and was poled under a high voltage power supply. A PDMS thin layer was used to encapsulate the device. In Fig. 2.12 is represented the variation of the temperature on the PNG and the measured output voltage. It is clear that the device is able to respond to dynamic changes of T with a good reproducibility. The sensor was also tested with different temperature and, as shown in the graph b), the response is linear in the range from 300 °K up to 325 °K, which are the temperatures in the typical range for tactile applications. The power consumption is a fundamental issue for integrated e-skin systems, for this reason the realization of self-powered systems is an important goal especially for this kind of tactile sensors. However, the response time of the device is very high (~0.9 sec) and the minimum detection limit is 0.4 °K which is higher than that requested for artificial skin applications.

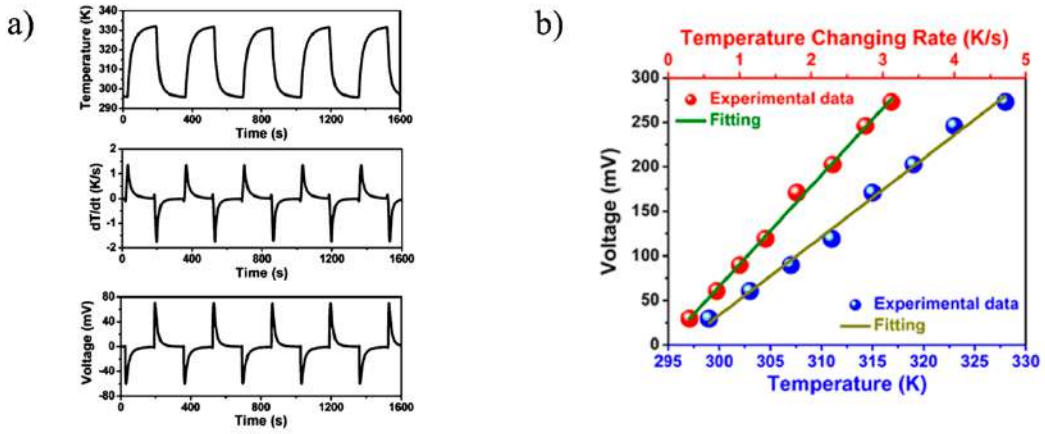

Fig. 2.12: a) Cyclic changes in temperature and the corrisponding differential curve, with the measured output voltage of the sensor. b) Calibration curve of the PZT nanogenerator. [27]

2.4 Other transduction mechanisms

Less used than the previous transduction mechanisms are *inductive tactile sensors* and *optoelectronic tactile sensors* because of their limited advantages. In general, an inductive sensor is based on the variation of magnetic coupling between a pair of coils, due to, for instance, a change in the geometrical parameters of one coil. Typically, inductive sensors have a high dynamic operating range but, due to their large dimension, suffer of a low spatial resolution and they also show a significant hysteresis [8].

Optic tactile sensors employ a light source and a photodetector. The transduction mechanism is based on the variation of the intensity of the light, emitted from the source and revealed by the detector, due to a variation of the temperature of the source or when an applied force changes the light's spectrum. In general, optoelectronic sensors do not suffer of the common low frequency noise and interferences and they have a good spatial resolution. However, their size and the problems related to their fabrication over flexible substrates make the integration in e-skin systems extremely difficult [8].

2.5 Field effect transistors as tactile sensors

A very large number of examples of tactile sensors reported in literature are based on Field-Effect Transistors (FETs). The success of FET structures with respect to other electronic sensors is mainly related to different aspects:

- FETs are multi-parameter devices, which allow the implementation of a wide range of transduction mechanism.
- FET structures have a very low power consumption and, thanks to their field effect, have a good amplification of the response.
- With this kind of structure there is the possibility to implement array and matrix of sensors, coupled the switching and addressing capability of these devices.

Referring to the output current of the transistor, I_{DS}:

$$\mathrm{I_{DS}} = \mathrm{f}(\mu, \mathrm{C_{ins}}, \mathrm{W}, \mathrm{L}, \mathrm{V}), \tag{2.11}$$

it can be noticed that, several parameters play an important role to the final value of the current: the charge carrier mobility (μ) of the semiconductor, the insulating capacitance (C_{ins}) of the dielectric, the geometrical parameters width (W) and length (L) of the channel and the operating voltages (V). All these parameters can be in theory employed for the transduction of external stimuli.

Field Effect Transistors as tactile sensors can be divided into two major groups. The first one includes approaches where the sensing element is the FET itself. The second group includes all the approaches where a FET structure is coupled with an external sensing element. In this case the transistor act as a transducing element.

One of the first works based on FETs as mechanical sensor was proposed by Sekitani et al. [28]. They demonstrated that by applying a compressive strain in the *Pentacene* active layer of an organic field effect transistor, an increase in the I_{DS} was observed. On the other hand, a decrease in the output current was induced during a tensile strain. Authors assumed that this phenomenon can be attributed to a reversible change of the structural properties of the polycrystalline semiconductor film. Considering the Equation of the hopping transport:

$$\mu \sim \mu_0 \exp(-\Delta E / k_B T), \tag{2.12}$$

where μ is the semiconductor mobility during a strain, μ_0 is the mobility without any tensile/compressive strain, k_B is the Boltzmann's constant, T is the temperature and ΔE is the energy barrier for hopping transport in Pentacene, it is evident that the strain has an effect in the semiconductor mobility referring to the value of the $\Delta E \propto -k_B T \ln(1+0.05\varepsilon)$ where ε is the strain expressed in percent. This behaviour is confirmed by the value of the mobility during different strains, which is reported in Fig. 2.13.

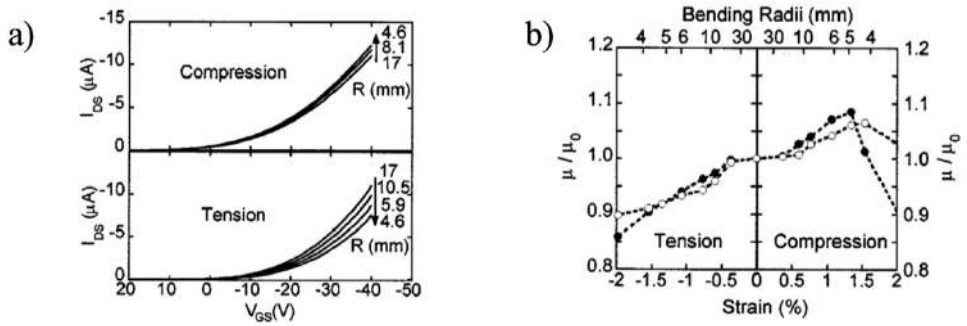

Fig. 2.13: a) Transfer curves on a compressive and tensile strains. b) Relative change in mobility of FETs plotted as function of strain. [28]

The correlation between the induced strain ε, and bending radius r, in a FET structure, is described in [29] by the following formula:

$$\varepsilon = \frac{(d_l + d_s)}{(2 * R)} \frac{(1 + 2\eta + \chi\eta^2)}{(1 + \eta)(1 + \chi\eta)}, \tag{2.13}$$

in which d_l and d_s are the thicknesses of the active layer and the substrate respectively, η is defined as d_l/d_s, R is the bending radius and χ is the ratio between the Young's moduli of the active layer and the substrate (i.e. $\chi = Y_l/Y_s$).

In Scenev et al. [30] is reported a deeper investigation on the effect of the strain on the active layer in an organic FET. Authors performed an accurate morphological analysis of the Pentacene active layer during strain stresses. Atomic Force Microscopy images, reported in Fig. 2.14, demonstrated that when a compressive strain is applied on the active layer of the FET structure, it is observed a decrease of the distance between grains. Considering the Equation 2.12, it is possible to assume that a compressive strain can reduce the energy barrier for hopping transport ΔE and consequently an increase in mobility is achieved. On the other hand, authors have demonstrated that strain stresses leave the crystal structure unaffected and also the deformation of the active layer is completely reversible.

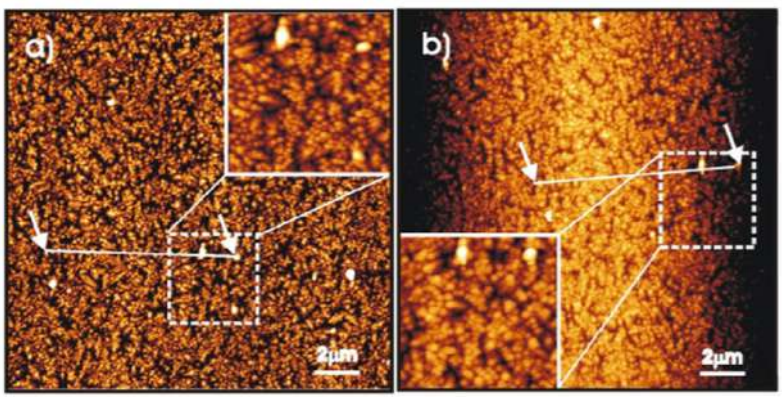

Fig. 2.14: SFM micrographs of a) a pristine Pentacene layer, and b) an in situ 10% strained Pentacene film. [30]

Particularly interesting is the work presented by Cosseddu et al. [31] where it has been demonstrated that morphological properties of the active layer have a strong correlation with the electrical behaviour of Pentacene based FET structures, during compressive strain. In particular, modulating the Pentacene morphology in terms of grain size, it is possible to tune the sensitivity to surface strain in a predictable and controllable way. However, the structures presented in [28] and [30] have a maximum tolerable strain of ~2%: it has been demonstrated that strains larger than 2% cause the formation of cracks within the gold source and drain electrodes on top of Pentacene film due to the high thickness of the employed substrate (~175μm).

In [32] authors compare the sensitivity of transistors with different semiconductors (Pentacene and *P3HT*). It has been demonstrated that the highly disordered structure of polymeric films, as P3HT, lead to a decrease of the sensitivity of the device due to the transport properties of these polymers. On the other hand, Pentacene based device showed a higher sensitivity (12.4% kPa^{-1}), a good reproducibility and a linear response in the range of 0.7 up to 4 kPa. However, the recovery time is quite high (>10 sec) and this can limit the dynamic response of the sensor.

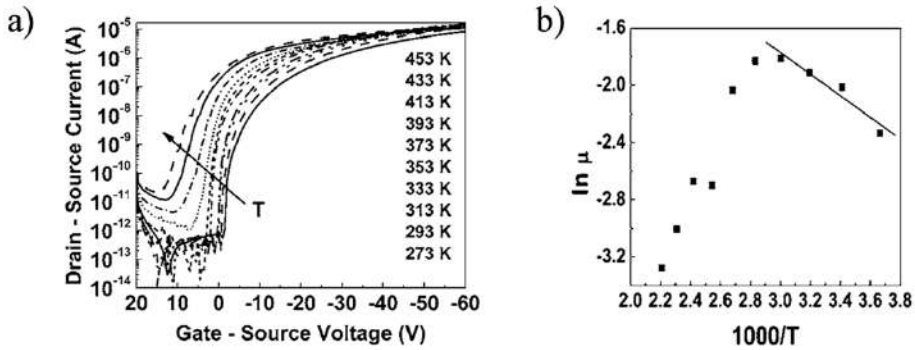

Fig. 2.15: a) Temperature dependent transfer curve of a pentacene TFT. b) Temperature dependent mobility in the saturation region. [33]

The correlation between mobility and mechanical stress is not the only way to exploit a FET structure. For instance, in Jung et al. [33] it has been investigated and demonstrated the relationship between the variations of the mobility of a semiconductor due to variations in their temperature. The proposed device is a bottom contact organic field effect transistor with a doped n-type silicon wafer which acts as substrate and gate. The gate dielectric is SiO_2 grown by thermal treatment, the Pentacene active layer was deposited by thermal evaporation over Palladium source and drain contacts. Authors have investigated the temperature dependence of the transport mechanism of Pentacene both in subthreshold and saturation regimes in a very large range from 273 to 453 °K.

Experimental results are reported in Fig. 2.15, the saturation current show negligible variations compared to those recorded in subthreshold regime where the current rise due to an increase of temperature from 273 °K to 333 °K. Interesting that the device shows a saturation of the response

for temperature higher than 333 °K caused by two possible reasons: the desorption of Pentacene active layer at higher temperature and/or an increase of the scattering of the Pentacene carries. Authors underlined that more studies were necessary. The temperature dependence of the output current is due to a variation of the effective mobility which can be described with the Arrhenius-like form:

$$\mu_{eff} \propto \exp\left(\frac{-E_a}{kT}\right), \tag{2.14}$$

where E_a is the activation energy, k is the Boltzmann's constant and T is the temperature.

Trung et al. [34] proposed a FET based temperature sensor, with a high thermal responsivity. The device exploit the thermosensitive property of a nanocomposite layer of *reduced graphene oxide* (R-GO) and a pyroelectric polymer (PVDF-TrFE). This layer is used as active layer in a field effect transistor. Moreover, authors have demonstrated that by changing properly the thickness of the R-GO/PVDF-TrFE active layer and by changing the concentration of R-GO it is possible to finely tune the sensitivity of the device (see Fig. 2.16). Also, the device shows a very high resolution (~0.1 °C) which is comparable to that of human skin, and a very large range of detectable temperatures [30 – 80] °C. Furthermore, the high flexibility and optical transparency of the employed materials make this device particularly suitable for artificial skin application.

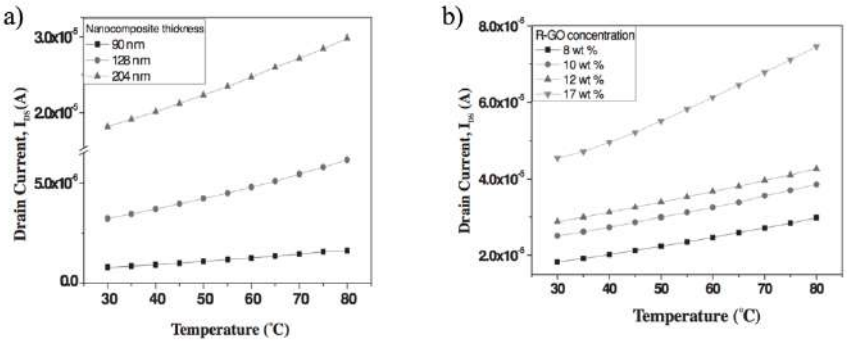

Fig. 2.16: a) I_{DS} response of the FET to temperature at different thickness of nanocomposite. b) I_{DS} response of the FET to temperature at different concentration of R-GO. [34]

As already mentioned, FETs structures can act as transducing part in a tactile sensor when coupled with an external sensing element. In this case the external stimulus, which can be mechanical (force, pressure or strain) or thermal, is sensed not directly by the OFETs semiconductor, but by the indirect modulation of the OFETs electrical parameters. This kind of "indirect" sensing is a versatile approach and, thanks to the wide range of categories of sensing elements and fabrication techniques that can be employed, there is the opportunity of achieve different sensitivities on different ranges, depending on the application's requirements.

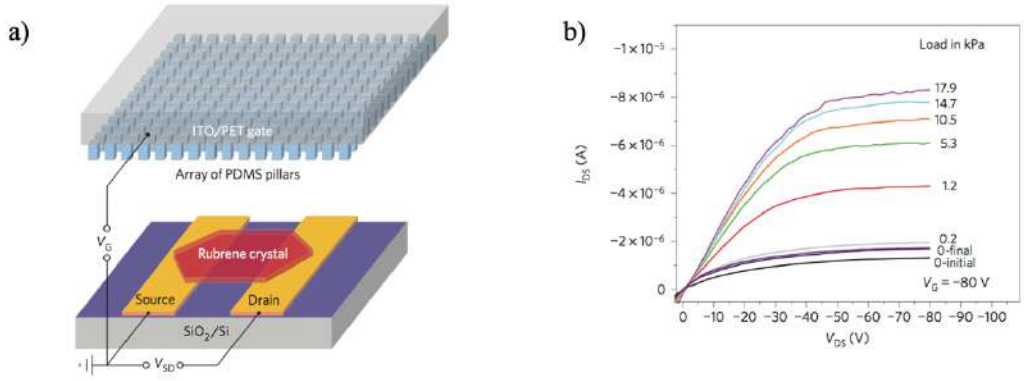

Fig. 2.17: a) Layout of pressure sensing OFET and structured PDMS dielectric film. b) I_{DS} with different external pressure applied. [7]

One of the most common approaches is for sure the connection of a sensing element to the gate electrode in order to change the output current of the transistor, due to a variation in its gate capacitance. As already mentioned in section 2.1, microstructuring the framework of an elastomeric material as dielectric layer of a capacitor it is possible to increase the sensitivity in terms of $\Delta C/C_0$.

Zhenan Bao's group were the firsts to report a microstructurated PDMS layer as a gate dielectric in a FET structure. The first work, presented in 2010, is based on a single-crystal *Rubrene* semiconductor (see Fig. 2.17) and a layer of PDMS pillars as gate dielectric [7]. The sensor shows a very high sensitivity, large workable pressure range [0.2 – 18] kPa, and negligible hysteresis. However, the use of highly n-doped silicon oxide wafer as FET's substrate limits the flexibility and stretchability of the device which are two fundamental requirements for e-skin application sensors.

To overcome this problem, the same group presented in 2013 a fully flexible pressure sensor based on FET structure with microstructure PDMS as gate dielectric [35]. Flexible *Polymide* (Kapton Hn) was used as substrate, PiI2T-Si (a high mobility coniugate semiconductor polymer) was deposited over gold Source and Drain electrodes. The high sensitivity (8.2 kPa^{-1}) in the low-pressure range [0 – 8] kPa and the fast response time (less than 10 msec) make this approach particularly interesting for artificial skin applications. Moreover, is recorded a linear response, but with a less sensitivity, in the range from 8 kPa up to 50 kPa and the sensor has a detection limit of 0.02 kPa. However, the system requires a very high driving voltage thus limiting the portability of the device.

The use of the gate capacitance as sensing variable is not the only way to exploit the FET structure as transducers. As already mentioned, several parameters play an important role to the final value of the current I_{DS}. Taking advantage of the well known properties of piezoelectric and pyroelectric materials it is possible to couple them with a FET structure in order to obtain a sensor.

For instance, in Dahiya et al. [36] is proposed a new version of *POSFET* (Piezoelectric oxide semiconductor field effect transistor) structure for tactile force sensing. The device is a simple FET structure in which a piezoelectric polymer film (PVDF-TrFE) is deposited over the gate electrode. When an external force is applied on the PVDF-TrFE film, a charge separation in the the polymer is generated thus a potential across it is generated. This potential affects the FET working point and, consequently, a shift in the output current I_{DS} is obtained. In this work are presented 16 POSFET element, fabricated in CMOS technology which guarantees a high integration, reliability and very high gain. The response has a detection limit of 0.01 N (which is comparable to that of human skin) and a clear linear behaviour from 0.01 N to 3 N. However, like any other CMOS based technology, the rigid nature of Silicon makes this chips non conformable. To overcome this problem, the same group is now working on the development of a POSFET structure fabricated on bendable thin Silicon substrate: recently, they have published an interesting work where is proposed a model which describe the behaviour of bendable POSFET as touch sensing system [37].

A similar approach, but exploiting the pyroelectric properties of PVDF-TrFE has been reported in [38]. In this work, authors used a fully flexible FET structure in which the transistor act as amplifier read-out unit. The sensing element, a screen printed pyroelectric PVDF-TrFE capacitor, has one electrode connected to the gate of the transistor. Initially the transistor is in the off state, therefore, when a change in temperature is applied to the pyroelectric capacitor, the voltage induced by the pyroelectric material leads to a variation of the transistor working point leading the transistor to switch on. The device is tested as opto-thermal switches with a good reproducibility and do not require high driving voltages. Nevertheless, is missing a complete electrothermal characterization in the typical tactile temperature range.

Another kind of approach consists in modulating the effective V_{DS} applied to an OFET, for instance with the employment of a conductive pressure sensor (as a conductive rubber) to be put in series with the source or drain electrode. Conductive rubbers can decrease their electrical resistance when they are subjected to an external pressure. Someya et al. [39] were the first to adopt this particular solution. The OFET was realized on one side of a plastic substrate, while the rubber was laminated in the back side. A through hole creates the connection between the source electrode and the pressure-sensitive rubber. The device is able to respond to pressure due to a variation of the rubber resistance, from 1 MΩ to 1 kΩ, which affected the output current I_{DS}.

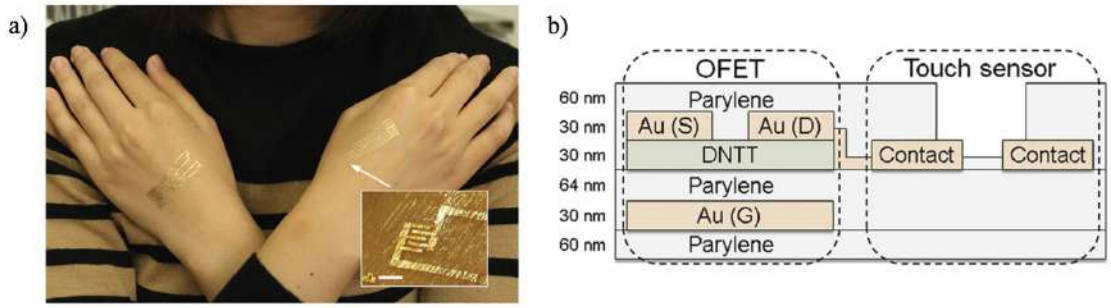

Fig. 2.18: a) 300-nm thick e-skin. b) Structure of the employed OFET and touch sensor. [40]

Very recently, the same group presents a tactile sensors based a FET structure on an ultrathin Parylene C substrate (~300 nm). This revolutionary approach exploit the biocompatibility of Parylene C, which make the device imperceptible and it can be transferred on human skin without causing any dermal irritation [40]. The structure, showed in Fig. 2.18, is a low voltage field effect transistor in which the touch sensor is connected with the drain electrode. The FET fabrication process started with the deposition of Parylene C substrate (~60 nm) on two sacrificial layers of *polyvinil alcohol* (PVA) and *fluorinated polymer* (FP) which were spin coated over a glass substrate. Gold gate electrode was thermally evaporated over the Parylene substrate, followed by a second Parylene C deposition (~64 nm) which acts as gate dielectric. Gold source and drain electrodes were deposited and patterned through shadow mask over a thin layer of DNTT organic semiconductor (~30 nm). Before the peel off of the device, it was encapsulated with a final deposition of Parylene C (~60 nm). After a complete electrical characterization which demonstrate the low voltage behaviour of the device, the transistor has been tested as a pressure detector. Its drain voltage depends on the conductivity of the touch sensor: in particular, when an object shorts the touch sensors contact, the voltage applied to the drain electrode change significantly. As shown in Fig. 2.19, the device can easily detect and discriminate the touch of a conductive element or a human finger.

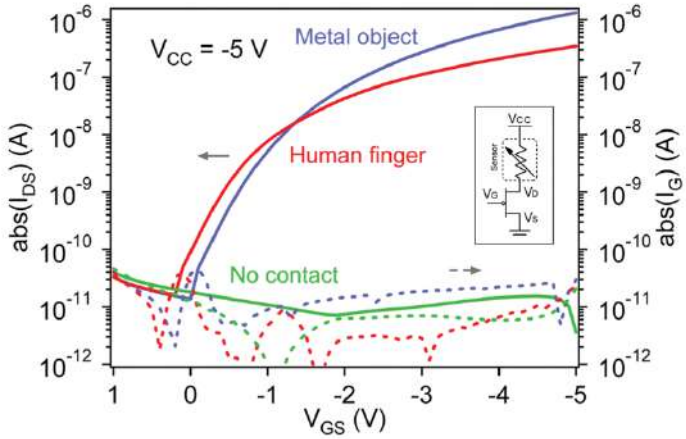

Fig. 2.19: Transconductance curve of the 300-nm thick e-skin with no contact, human finger contact or metallic object contact. [40]

A non secondary problem of some of the previously reported structures [28] – [35] is that the external stimulus is directly applied to the semiconductor. This can lead to an irreversible degradation of the active layer or of the source and drain contact.

To overcome this problem, is interesting the approach proposed by Lai et al. [41]. In this work a new FET structure (called *Pressure-Modulated Organic Field-Effect Transistor* or PMOFET) is presented. The peculiarity of PMOFETs is that the pressure-sensitive area is physically separated from the active area of the device. Basically, is a floating-gate transistor biased through a control capacitor called *control gate*. The transduction mechanism is based on the modulation of a PDMS capacitor, which acts as the sensing element, connected with the floating gate due to a change in its thickness when is exposed to mechanical stresses. According to Equation 2.15 this modulation can affect the floating gate voltage:

$$V_{FG} = \frac{C_{CF}}{C_{SUM}} V_{CG} + \frac{C_V}{C_{SUM}} V_C + \frac{Q_0}{C_{SUM}}, \tag{2.15}$$

where V_{FG} is the floating gate voltage, C_{CF} is the control gate capacitance, C_V is the PDMS variable capacitance, Q_0 is the total charge in the floating gate (which depends on the fabrication process), V_{CG} is the control gate potential, V_C is the potential applied to the top electrode of the PDMS capacitor and C_{SUM} is the sum of the all the capacitance in series with the floating gate.

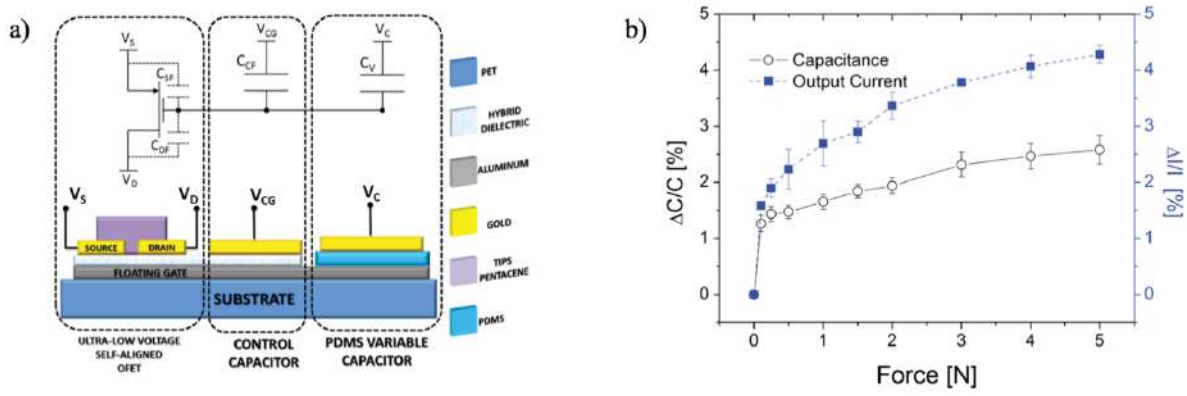

Fig. 2.20: a) Structure of the PMOFET and employed materials. b) Variation in the output current of the PMOFET compared with the variation of the PDMS capacitance with the applied force. [41]

The structure and the response of the sensor are shown in Fig. 2.20. A change in the floating gate voltage lead to a variation of the output current I_{DS}. Thanks to the field effect of the transistors, which act as an amplifier, the percentage variation of the current is higher than that of the PDMS capacitor. Moreover, the device is able to sense forces with a resolution of 0.1 N, in the range from [0.1 – 5] N.

2.6 Multifunctional tactile sensors

As widely described in Chapter 1, artificial skin must have the capability to detect different parameter simultaneously in order to simulate the multifunctional nature of human skin. Normal, shear and torsion force, temperature variations, stretch and bending are, probably, the most important parameters that e-skin should be able to recognize.

Moreover, a growing interest in electronic devices having features such as flexibility, conformability, and lightness has paved the way to several kinds of flexible and ultra-conformable electronic devices that can be transferred on the skin: the term “tattoo electronics” is used to refer to these applications, especially in the biomedical field.

One of the first approach of a fully flexible multifunctional sensors for artificial skin application is the work presented by Someya et al. [42] in 2005. Basically, this approach is based on an active matrix, based on flexible organic transistors, with an integration of:

i. conductive rubber sheet for pressure sensing.
ii. Organic Diodes (CuPc/PTCDI) on ITO-PEN sheet for temperature monitoring.

The innovative employed structure (a net shape framework) permits to stretch the active matrix up to 25% and also leads to a good thermal isolation between neighboring regions. As shown in Fig.

2.21, conductive rubber and organic diodes play a fundamental role in the modulation of transistor's output current with pressure and temperature, respectively. Moreover, the matrix has a good selectivity between the two different stimuli, due to the completely insensitive behaviour of the rubber and the diodes at temperature and pressure respectively.

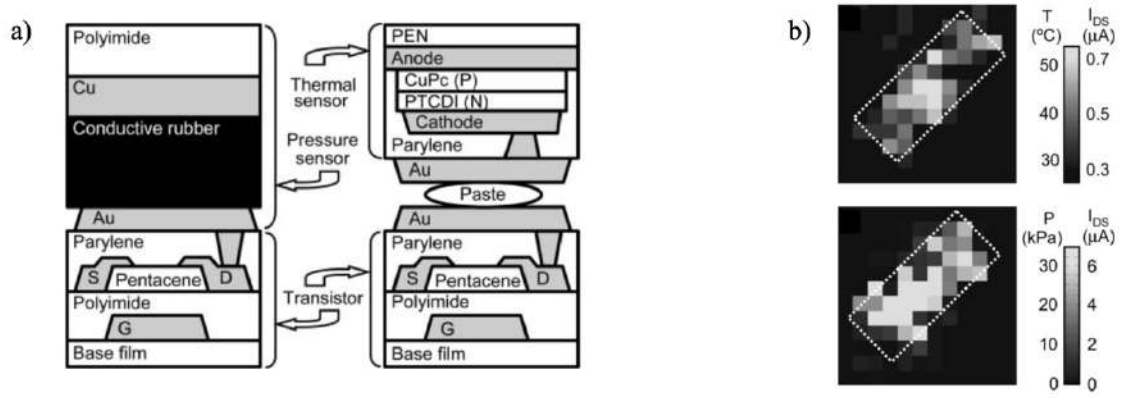

Fig. 2.21: a) Cross section of the pressure sensor (left) and thermal sensor (right). b) Spatial distribution of temperature and pressure and output current response. [42]

In Graz et al. [43] is presented an integration of flexible matrix cells for pressure and temperature sensing skin. Through a proper poling procedure, authors have demonstrated that is possible to maximize the piezoelectric property and minimize pyroelectric one (and vice versa) of a single cell thus tuning the sensitivity of each cell. This result is achieved by the combination of different ferroelectric materials: each multifunctional sensing element is based on pyroelectric ceramic nanoparticles (lead titanate) embedded in a ferroelectric polymer (PVDF-TrFE). Interfacing both sensory cells with organic transistors is possible to obtain an active matrix of sensors for flexible electronic skin.

John Rogers' group proposed an approach that led to the development of a variety of conformable "epidermal electronic systems" with an excellent adhesion to skin [44]. Authors show how to optimize the conformal contact between electronic devices and skin, by reducing not only the thickness of the employed materials, but also varying their Young's modulus (or elastic modulus) and the layout of the device and the interconnections. Referring to Equation 2.16:

$$E_{EES} = E_{int} * \left(1 + \frac{L_d}{L_s}\right), \tag{2.16}$$

where E_{EES} is the effective elastic modulus of the reported system, E_{int} is the effective modulus of the interconnections, L_d is the characteristic device size and L_s is the distance between the devices, it is possible to minimize E_{EES} by reducing the Young's modulus of the interconnections and also the ratio L_d/L_s. Using a filamentary serpentine (FS) for the devices' interconnections, which significantly increase L_s, it is possible to achieve an $E_{EES} \sim 140$ kPa which is comparable to that of

human skin (~160 kPa). The system permits to obtain a very good conformal contact to human skin even during high compressive or tensile deformations (see Fig. 2.23). Another interesting point is the fabrication process: all the devices (fabricated in Si/GaAs technologies) are integrated on the surface of a thin elastomeric Silicon based sheet (~30 μm) which is fixed onto a water-soluble sacrificial layer of polyvinyl alcohol (PVA). After mounting the system onto the skin, it is possible to remove the PVA layer by simple washing procedure, as a "tattoo like" mounting procedure based on the Van der Walls forces between the integrated devices and the epidermis.

However, the most important disadvantages of this fabrication procedure is the easiness of the delamination of the system to the skin that significantly reduces the lifetime of the integrate devices.

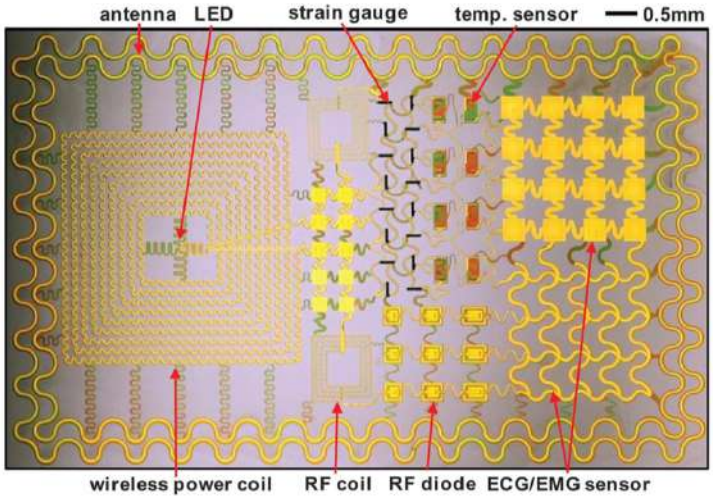

Fig. 2.22: Image of a demonstration of an epidermal electronics. [44]

To overcome this problematic, the same group propose an alternative fabrication process which can improve the system's lifetime and also can reduce further the total thickness of the structure [45]. This is based on a "spray-on-bandage" process in which an adhesive layer is sprayed onto the epidermis, then the electronics are transferred on the adhesive layer and finally a encapsulant is sprayed on the system. This method can improve the Van der Walls interaction forces between the system and the epidermis, and the duration of the tattoo attached on the skin. Moreover, with this new fabrication process is possible to transfer only the electronic devices with no Silicon sheet thus reducing the total thickness of a few microns.

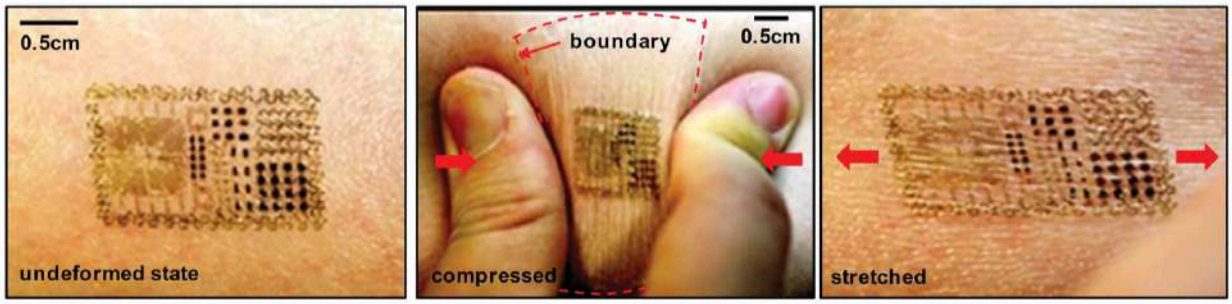

Fig. 2.23: Epidermal electronics on skin: undeformed (left), compressed (center), stretched (right). [44]

Takei et al. proposed a multifunctional flexible system for monitoring temperature/strain [46] and temperature/pressure [47]. The system's structure is similar in both cases, and is based on screen printed CNTs and silver nanoparticles (AgNP) pressure/strain sensors and screen printed CNTs and PEDOT:PSS as temperature sensors. The system is able to detect and monitoring temperature changes in a quite large range [19 – 50] °C with a linear response. On the contrary, the range of detectable pressure/strain sensors is limited due to a saturation of the piezoresistive response of the CNTs/AgNP sensors.

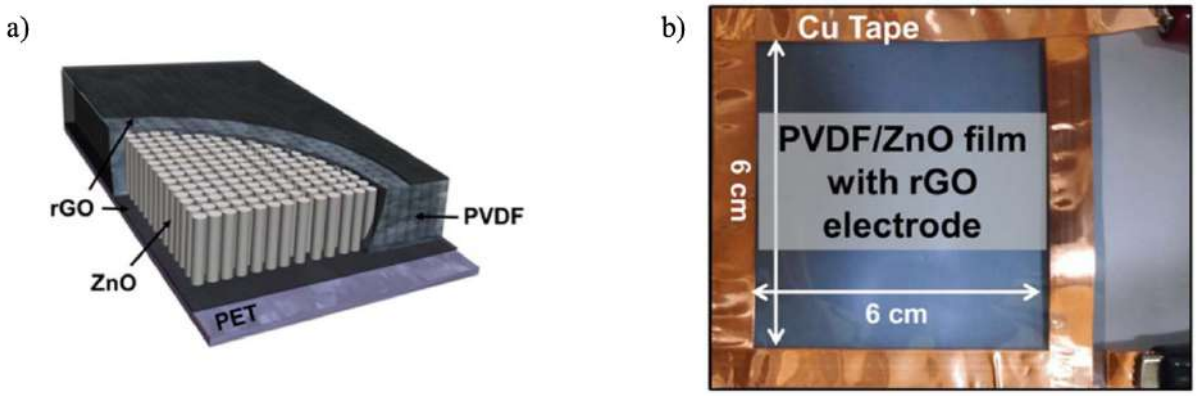

Fig. 2.24: a) Schematic representation of the sensor. b) Photograph of the ZnO/PVDF composite device. [48]

In Lee et al. [48] is presented a highly sensitive and multifunctional resistive sensor for pressure and temperature monitoring for artificial skin applications. The sensing element is a hybrid PVDF thin film coupled with zinc oxide (ZnO) vertical nanorods over an inkjet printed graphene based electrode. Fig. 2.24 shows a schematic illustration of the flexible multilayer device. Zinc oxide nanorods were embedded in the PVDF polymer onto a reduced graphene oxide (rGO)-treated flexible polyethylene terephthalate (PET) thin film. Graphene oxide aqueous ink was deposited over a flexible PET substrate via inkjet printing, and reduced for use as an electrode. The ZnO nanorods were grown, followed by a hydrothermal treatment. The 20-wt% PVDF solution was spin-coated onto the ZnO nanorods and then poled at a strong constant electric field of 300 kV/cm at 90 °C to induce ferroelectricity in the PVDF. Monitoring pressure, which affect the electrical

resistance of the material, and temperature, which can be inferred from the recovery time of the signal, it has been demonstrated the multimodal nature of the device.

However, despite a pressure resolution of 10 Pa which is several times lower to that of human skin, the detectable pressures range is [10 – 120] Pa which do not cover the entire range requested for e-skin application. On the contrary, the device is able to monitor temperature between [20 – 120] °C but there is no information about the thermal resolution.

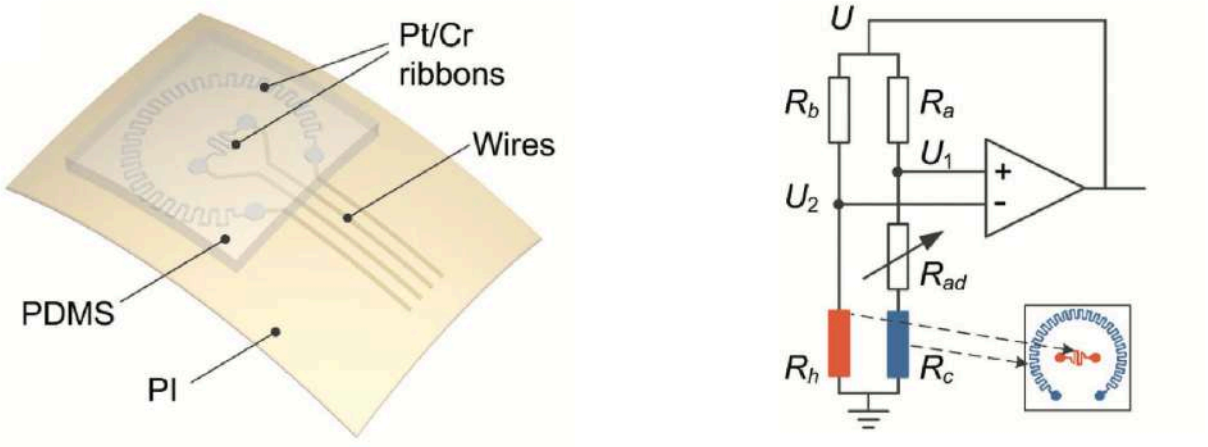

Fig. 2.25: Illustration of the Pt nanoribbons sensor (left) and schematic of the employed circuit (right). [49]

Very recently, Zhao and Zhu reported an electronic skin with multifunction sensors for temperature and pressure detection [49]. The system is based on a pair of platinum (Pt) ribbons connected into a Wheatstone bridge and covered by a PDMS elastomer (see Fig. 2.25). The transduction mechanism is based on the pyroresistive behaviour of the platinum and the thermal conductivity of the PDMS. The resistances of the center ribbon (R_h), which acts as pressure sensor, is 92 Ω and the resistance of the anular ribbon (R_c), which acts as temperature sensor, is 933 Ω. R_h is heated to a higher temperature respect to the ambient. Due to the ΔT between the center Platinum ribbon and the ambient, lead to a conductive heat transfer from the ribbon to the PDMS. When a pressure is applied to the elastomer, its thermal conductivity change and consequently the ΔT with the center ribbon. By calculating the variation of the temperature, it is possible to establish the external applied pressure P.

On the other hand, anular platinum ribbon is used as a simple pyroresistive sensor, and gives information to the ambient temperature. As shown in Fig. 2.26, the system is able to detect simultaneously temperature and pressure variations with a high sensitivity and resolution and a negligible hysteresis.

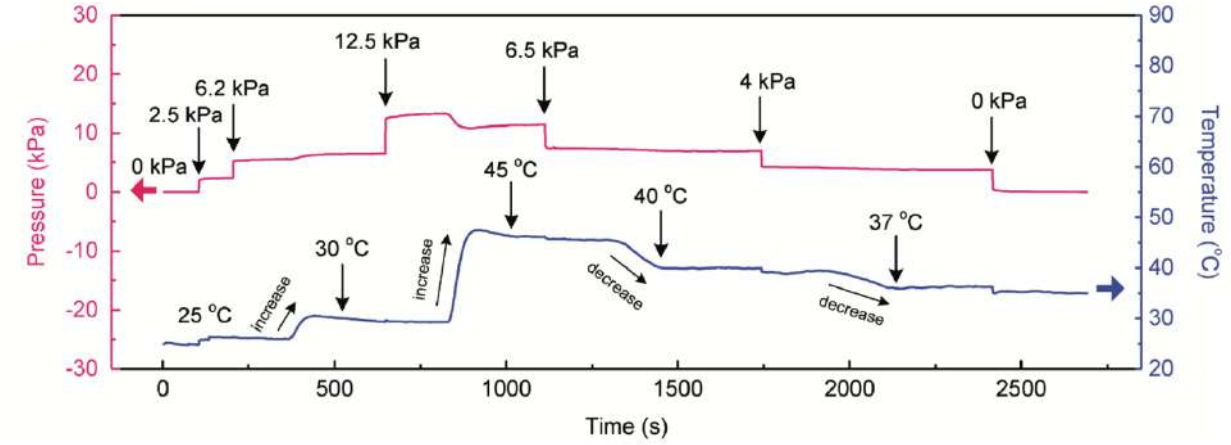

Fig. 2.26: Simultaneous and independent detections of pressure and temperature. [49]

Bibliography

[1] D. P. J. Cotton et al. "*A multifunctional capacitive sensor for stretchable electronic skins*", IEEE Sensors Journal, 2009, vol. 9 (12).

[2] J. A. Dobrzynska and M. A. M. Gijs, "*Polymer-based flexible capacitive sensor for three-axial force measurements*", Journal of Micromechanics and Microengineering, 2012, vol. 23.

[3] X. Guo et al. "*Capacitive wearable tactile sensor based on smart textile substrate with carbon black/silicone rubber composite dielectric*", Measurements Science and Technology, 2016, vol. 27.

[4] S. P. Lacour et al. "*Elastomeric Capacitive Sensors*", 16th International Solid-State Sensors, Actuators and Microsystems Conference, June 2011.

[5] H. Vandeparre et al. "*Extremely robust and conformable capacitive pressure sensors based on flexible polyurethane foams and stretchable metallization*", Applied Physics Letters, 2013, 103 (204103).

[6] W. Hu et al. "*Elastomeric transparent capacitive sensors based on an interpenetrating composite of silver nanowires and polyurethane*", Applied Physics Letters, 2013, vol. 102 (083303).

[7] S. C. B. Mannsfeld et al. "*Highly sensitive flexible pressure sensors with microstructured rubber dielectric layers*", 2010, Nature Materials, vol. 9, pp. 859-864.

[8] M. I. Tiwana et al. "*A review of tactile sensing technologies with applications in biomedical engineering*", Sensors and Actuators A: Physical, 2012, vol. 7, pp. 17-31.

[9] R. S. Timsit, "*Electrical conctact resistance: properties of stationary interfaces*", IEEE Transactions on Components and Packaging Technologies, 1999, vol. 22 (1), pp. 85-98.

[10] W. Y. Chang et al. "*A large area flexible array sensors using screen printing technology*", Journal of Display Technology, 2009, vol. 5 (6), pp. 178-183.

[11] J. G. Dabling et al. "*Static and cyclic performance evaluation of sensors for human interface pressure measurement*", 34th Annual International Conference of the IEEE EMBS, 2012, San Diego, California USA.

[12] S. Gong et al. "*A werable and highly sensitive pressure sensor with ultrathin gold nanowires*", Nature Communications, 2014, vol. 5 (3132).

[13] M. K. Abyaneh et al. "*Giant piezoreristive response in zinc-polydimethylsiloxane composites under uniaxial pressure*" Journal of Physics D: Applied Physics, 2008, vol. 41.

[14] Z. M. Dang et al. "*Supersensitive linear piezoresistive property in carbon nanotubes/silicone rubber nanocomposites*", Journal of Applied Physics, 2008, 104 (024114).

[15] S. Lee et al. "*A transparent bending-insensitive pressure sensor*", Nature Nanotechnology, 2016, vol.11.

[16] X. Xiao et al. "*High-strain sensors based on ZnO nanowire/polystyrene hybridized flexible films*", Advanced Materials, 2011, vol.23, pp. 5440-5444.

[17] X. X. Gong et al. "*Flexible strain sensor with high performance based on PANI/PDMS films*", Organic Electronics, 2017, vol. 42, pp. 51-56.

[18] T. W. Tombler et al. "*Reversible electromechanical characteristics of carbon nanotubes under local-probe manipulation*" Nature, 2000, 405, pp. 769-772.

[19] S. H. Bae et al. "*Graphene-based transparent strain sensor*", Carbon, 2013, vol. 51, pp. 236-242.

[20] G. Mattana et al. "*Woven temperature and humidity sensors on flexible plastic substrates for E-Textile Applications*", IEEE Sensors Journal, 2013, vol. 13 (10).

[21] R. C. Webb et al. "*Ultrathin conformal devices for precise and continuous thermal characterization of human skin*", Nature Materials, 2013, vol. 12.

[22] M. D. Dankoco et al. "*Temperature sensor realized by inkjet printing process on flexible substrate*", Materials science and Engineering B, 2016, vol. 205, pp. 1-5.

[23] T. Vuorinen et al. "*Inkjet-Printed Graphene/PEDOT:PSS Temperature Sensors on a Skin-Conformable Polyurethane Substrate*", Scientific Reports, 2016, 6 (35289).

[24] J. Jeon et al. "*Flexible Wireless Temperature Sensors Based on Ni Microparticle-Filled Binary Polymer Composites*", Advanced Materials, 2013, vol. 25, pp. 850-855.

[25] S. Khan et al. "*Screen printed flexible pressure sensors skin*", 25th Annual SEMI Advanced Semiconductor Manufacturing Conference (ASMC), 2014, pp. 219-224.

[26] R. S. Dahiya et al. “Deposition, processing and characterization of P(VDF-TrFE) thin films for sensing applications”, IEEE Sensors, 2008, pp. 490-493.

[27] Y. Yang et al. “*Single micro/nanowire pyroelectric nanogenerators as self-powered temperature sensors*”, ACS Nano, 2012, vol. 6, pp. 8456-8461.

[28] T. Sekitani et al. “*Bending experiment on pentacene field-effect transistors on plastic films*”, Applied Physics Letters, 2005, vol. 86.

[29] Z. Suo et al. “*Mechanics of rollable and foldable film on-foils electronics*”, Applied Physics Letters, 1999, vol. 74.

[30] V. Scenev et al. “*Origin of mechanical strain sensitivity of pentacene thin-film transistors*”, Organic Electronics, 2013, vol. 14, pp. 1323-1329.

[31] P. Cosseddu et al. “*Continuous tuning of the mechanical sensitivity of Pentacene OTFTs on flexible substrates: from strain sensors to deformable transistors*”, Organic Electronics, 2013, vol. 14, pp. 206-211.

[32] P. Cosseddu et al. “*Strain sensitivity and transport properties in organic field-effect transistors*”, IEEE Electron Device Letters, 2012, vol. 33 (1).

[33] S. Jung et al. “*Temperature sensor using thermal transport properties in the subthreshold regime of an organic thin film transistor*”, Applied Physics Letters, 2007, vol. 90.

[34] T. Q. Trung et al. “*Flexible and transparent nanocomposite of reduced graphene oxide and P(VDF-TrFE) copolymer for high thermal responsivity in a field-effect transistor*”, Advanced Functional Materials, 2014, vol. 24, pp. 3438-3445.

[35] G. Schwartz et al. “*Flexible polymer transistors with high pressure sensitivity for application in electronic skin and health monitoring*”, Nature Communications, 2013, vol. 4.

[36] R. S. Dahiya et al. “*Tactile sensing chips with POSFET array and integrated interface electronics*”, IEEE Sensors Journal, 2014, vol. 14 (10).

[37] S. Gupta et al. “*Device modelling for bendable piezoelectric FET-based touch sensing system*”, IEEE Transactions on circuits and systems, 2016, vol. 63 (12).

[38] M. Zirkl et al. “*An all printed ferroelectric active matrix sensor network based on only five functional materials forming a touchless control interface*” Advanced Materials, 2011, vol. 23, pp. 2069-2074.

[39] T. Someya et al. “*A large-area, flexible pressure sensor matrix with organic field-effect transistors for artificial skin applications*”, PNAS, 2004, vol. 101 (27).

[40] R. A. Nawrocki et al. "*300-nm imperceptible, ultraflexible, and biocompatible e-skin fit with tactile sensors and organic transistors*", Advanced Electronic Materials, 2016, vol. 2.

[41] S. Lai et al. "*Ultralow voltage pressure sensors based on organic FETs and compressible capacitors*", IEEE Electron Device Letters, 2013, vol. 34 (6).

[42] T. Someya et al. "*Conformable, flexible, large-area networks of pressure and thermal sensors with organic transistor active matrixes*", PNAS, 2005, vol. 102 (35).

[43] I. Graz et al. "*Flexible active-matrix cells with selectively poled bifunctional polymer-ceramic nanocomposite for pressure and temperature sensing skin*", Journal of Applied Physics, 2009, vol. 106.

[44] D. H. Kim et al. "*Epidermal electronics*", Science, 2011, vol. 333.

[45] W. H. Yeo et al. "*Multifunctional epidermal electronics printed directly onto the skin*", Advanced Materials, 2013, vol. 25, pp. 2773-2778.

[46] K. Takei et al. "*Flexible, printed tactile, friction, and temperature sensor array for artificial skin*", Transducers 2015.

[47] K. Takei et al. "*Printable flexible tactile pressure and temperature sensors with high selectivity against bending*", MEMS 2015.

[48] J. S. Lee et al. "*Highly sensitive and multifunctional tactile sensor using free-standing ZnO/PVDF thin film with graphene electrodes for pressure and temperature monitoring*", Scientific Reports, 2015, vol. 5.

[49] S. Zhao et al. "*Flexible bimodal sensor for simultaneous and independent perceiving of pressure and temperature stimuli*", Advanced Materials Technology, 2017.

3 OCMFETs as tactile sensors

In this Chapter the basic concepts of the Organic Charge Modulated Field Effect Transistor (the device used in this work) will be introduced. After a brief description of its working principle and applications, the experimental results as a tactile sensor, obtained in the first part of this work, will be provided.

3.1 Working principle of the OCMFET

In 2006, the microelectronic group of the University of Cagliari lead by Luigi Raffo and Annalisa Bonfiglio, proposed an original solid state device able to detect changes of electric charge in the range of a few electrons per nanometer [1].

This particular charge sensor (called *Charge Modulated Field Effect Transitor* or CMFET) can be used for the detection of multiple processes as, for instance, DNA hybridization [2]. It is basically a floating gate transistor, in which the transduction mechanism is based on the modulation of the field-effect of the transistor induced by variations of the electric charge in a particular area of the device, called *sensing area*.

The device is shown in Fig. 3.1: the floating gate, which is biased through a control capacitor (called *control gate*), has one part exposed to the environment acting as sensing area.

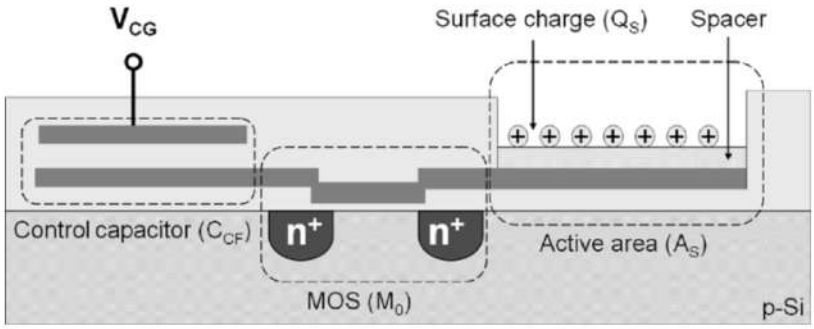

Fig. 3.1: Basic structure of the CMFET. [1]

If a specific process determines a variation of the total charge in the proximity of the sensing area, this induces a shift in the threshold voltage of the transistor. One of the main advantages of the CMFET working principle is that it can be implemented using different technological approaches as, for example, using organic electronics. The Organic-CMFET or OCMFET exploit the

innovative working principle of the inorganic one, together with the well-known advantages of the organic electronics.

As already mentioned, CMFETs and OCMFETs are floating gate transistors that can be used as charge sensors. An induced charge (Q_i) onto the sensing area generates an electric field that leads to a charge redistribution within the floating gate. Then, the induced charge under the FET structure is able to polarize the gate insulator and, consequently, change the charge carriers density in the channel of the transistor. The control gate-voltage (V_{CG}) and the electric charge, together, play a fundamental role in determining the voltage difference between the floating-gate and the source electrode (V_{FG}), which is usually grounded.

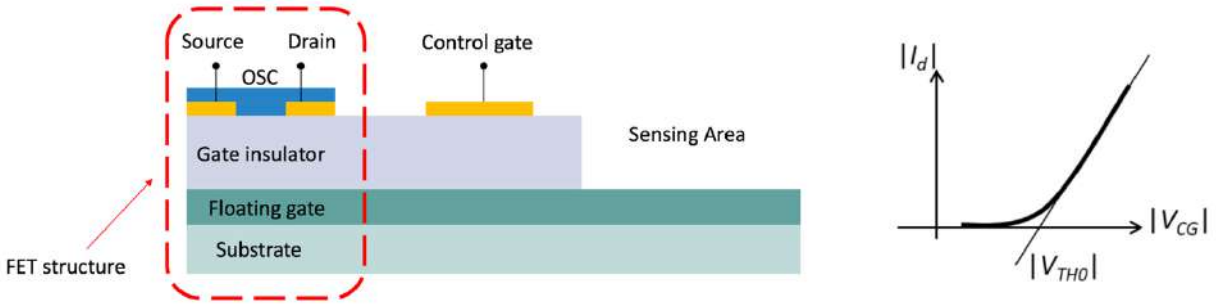

Fig. 3.2: OCMFET structure and transfer characteristic with no induced charges on the sensing area.

It is possible to derive the relationship between the control gate voltage, the induced charge and the transistor's effective threshold starting from Gauss' equation to the common node of the capacitors. The total charge Q_f in the floating gate can be written as:

$$Q_f = C_{CG}(V_{FG} - V_{CG}) + C_{SF}V_{FG} + C_{DF}(V_{FG} - V_D) + Q_i, \tag{3.1}$$

where V_D is the drain voltage, C_{CG} is the capacitance of the control capacitor, C_{SF} and C_{DF} are the parasitic capacitances between the floating gate and the source and the drain electrodes.

$$V_{FG}(C_{CG} + C_{SF} + C_{DF}) = (Q_f - Q_i) + C_{CG}V_{CG} + C_{DF}V_D, \tag{3.2}$$

$$V_{FG} = \frac{(Q_f - Q_i)}{C_{TOT}} + \frac{C_{CG}}{C_{TOT}}V_{CG} + \frac{C_{DF}}{C_{TOT}}V_D. \tag{3.3}$$

In a floating gate FET structure, it is possible to define the effective threshold voltage (V_{TFH}) as the value of the threshold voltage when the transistor is biased from the control gate, which is different from the value V_{TH} of the same transistor biased through the floating gate. In this kind of structure, we can consider the following relation:

$$V_{CG} - V_{THF} = V_{FG} - V_{TH}. \tag{3.4}$$

Consequently:

$$V_{CG} - V_{THF} = V_{FG} - V_{TH} = \frac{(Q_f - Q_i)}{C_{TOT}} + \frac{C_{CG}}{C_{TOT}}V_{CG} + \frac{C_{DF}}{C_{TOT}}V_D - V_{TH}. \tag{3.5}$$

The parasitic capacitances C_{SF} and C_{DF} depend on the overlap between the source/drain electrode

and the floating gate. It is possible to minimize this contribution with a particular fabrication technique called *self-alignment*, consequently the value C_{CG}/C_{TOT} could be considered 1.

$$V_{CG} - V_{THF} \cong \frac{(Q_f - Q_i)}{C_{TOT}} + V_{CG} + \frac{C_{DF}}{C_{TOT}} V_D - V_{TH}. \tag{3.6}$$

By solving the equation for V_{THF}:

$$V_{THF} \cong V_{TH} - \frac{C_{DF}}{C_{TOT}} V_D - \frac{(Q_f - Q_i)}{C_{TOT}}. \tag{3.7}$$

If we consider a change in the charge induced on the sensing area, assuming that the capacitances and Q_f do not vary and assuming that the transistor's biasing has not been changed, it is possible to define the effective threshold voltage shift as:

$$\Delta V_{THF} = \frac{\Delta Q_i}{C_{TOT}}. \tag{3.8}$$

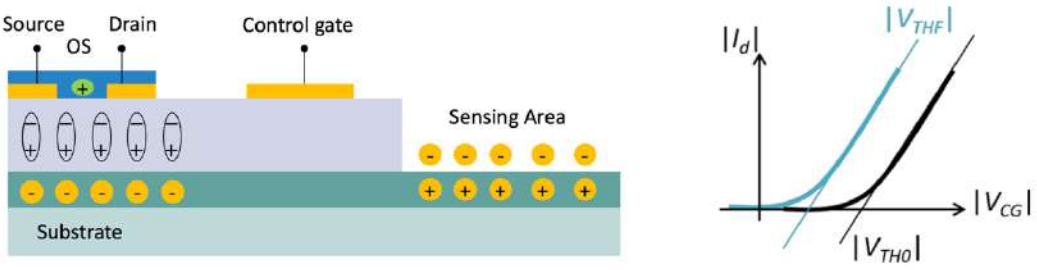

Fig. 3.3: Effect of the induced charges on the sensing area and shift of the threshold voltage in a OCMFET.

Thus, it's possible to use this structure as a transducer for any physical or biological process that can change the total charge accumulated on the sensing area. The most important advantages of this approach are:

i. differently than in other approaches based on transistors, the sensing element and the amplification element (the transistor) are here physically separated, preventing the external stimulus to damage the intrinsic characteristics of the semiconductor.

ii. The transduction mechanism is completely independent of the specific technological process, the choice of dielectric and the employed semiconductor, thus enabling the possibility to develop the same device concept with different fabrication technologies (not only organic, but also inorganic, or hybrid approaches).

This kind of structure has been successfully used for monitoring pH variations, DNA hybridization and the electrical activity of living cells, as reported in the following section.

3.2 State of the art

One of the first works based on the OCMFET structure as sensor is reported in Caboni et al. [3]. In this work, the authors presented a Pentacene-based OCMFET, made on a flexible plastic substrate, for the detection of chemical species in aqueous solution. The sensor (as shown in Fig. 3.4) consisted in two OCMFETs with common source and gate electrodes: one FET acted as a reference, the other one as the sensing device, which gave to the system the possibility to perform differential measurements. The system had also a PDMS fluidic, which was needed to guide the liquid solution toward the sensing areas. To achieve the OCMFET sensitivity to pH, the gold sensing area was functionalized with amino-terminated molecules, which are able to get protonized or de-protonized in response to pH changes in the bulk of the solution.

For pH > 7 the amino-terminated molecules acquire protons thus getting a positive net charge According to the OCMFET working principle, widely explained in Section 3.1, an accumulation of positive charges on the sensing area cause a redistribution of charge in the floating gate and, in particular, an induction of positive charges under the FET structure. Consequently, the transistor is led to a switching off due to a depletion of positive charge in its channel, given that the employed semiconductor is a p-type. In Fig. 3.4 the sensor response to different pH values is shown.

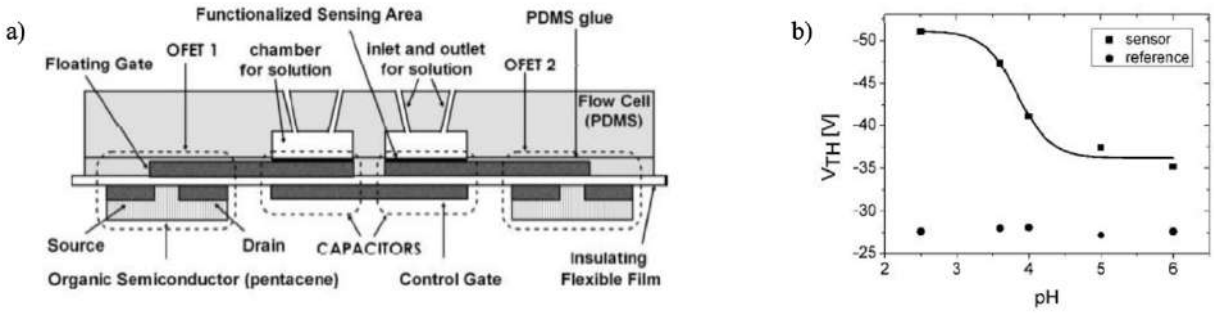

Fig. 3.4: a) OCMFET differential system structure and b) Shift of the threshold voltages for different pH measurements. [3]

In Demelas et al. [4] is presented a sensor able to detect the DNA hybridization in liquid. The device was fabricated onto a flexible PET substrate and the dielectric layer was a Parylene C thin film deposited by chemical vapour deposition process (CVD). Differently to the approach presented in [3] the fluidic was not employed in this case, and the device layout was modified in order to have the possibility to directly immerse the sensing areas in a liquid solution. The system comprised two OCMFETs (one acted as the sensor, and the other one as the reference) in order to perform differential measurements.

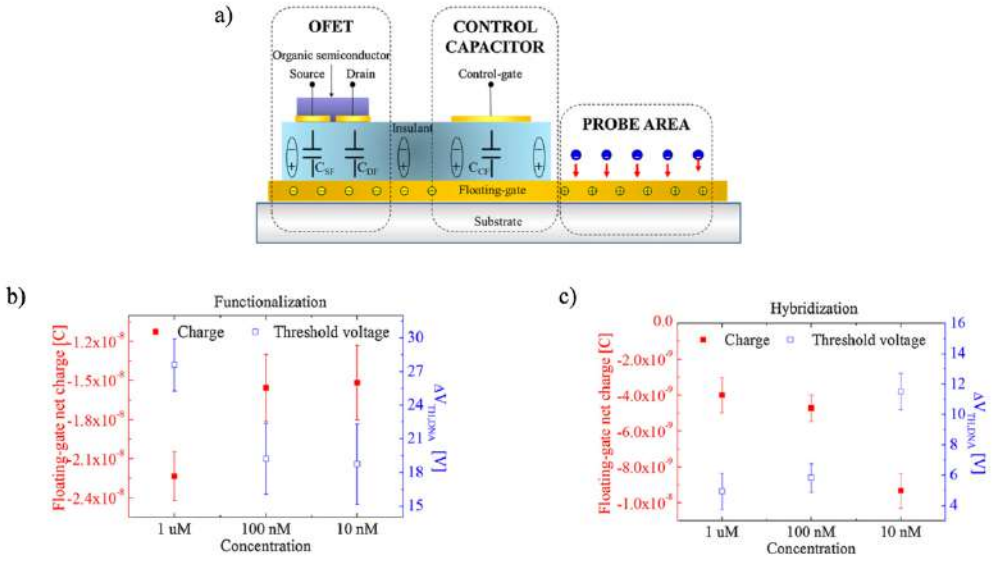

Fig. 3.5: a) OCMFET structure for DNA sensing. b) and c) Shift of the threshold voltage for different DNA concentration after the functionalization and hybridization. [4]

The device was employed as a DNA hybridization sensor. Since DNA has a net negative charge, the effect of the immobilization of single DNA strands onto the sensing area is the variation of the distribution of charges in the floating gate, and a subsequent shift of the transistor's threshold voltage due to a negative charge induced under the FET structure which cause an accumulation of positive charge in the transistor channel. During the hybridization step, the complementary strands get bond with the complementary immobilized ones, increasing the net negative charge induced on the sensing area and thus further shifting the threshold voltage. In Fig. 3.5 the structure and the experimental results are shown.

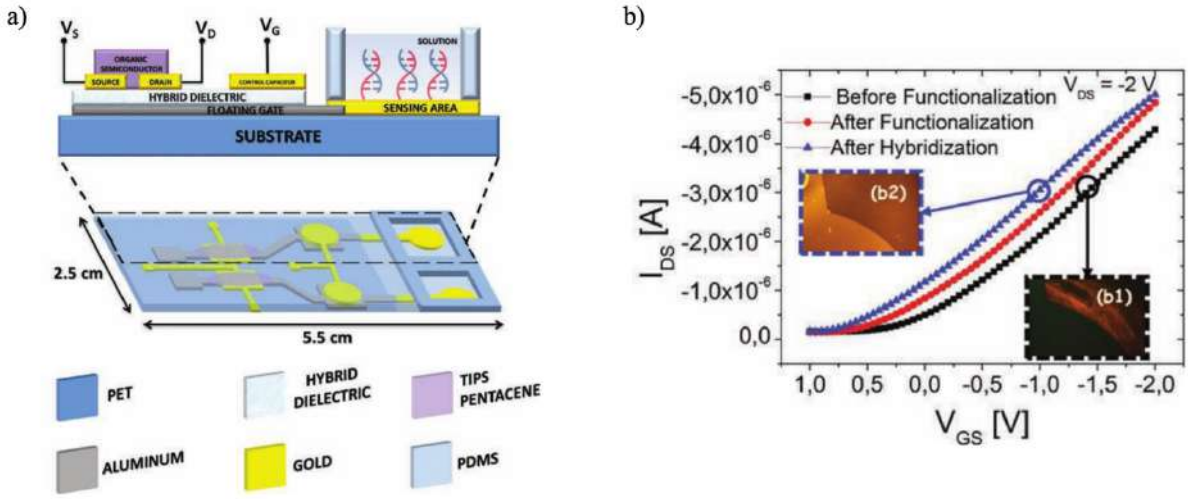

Fig. 3.6: a) Schematic representation of two OCMFETs (one act as sensor and one act as reference) for DNA sensing. b) Transfer characteristics of the sensor before and after functionalization and after hybridization. It is possible to appreciate the low-voltage behaviour of the transistor. [5]

One of the biggest limitations of this approach is that the devices operated with high voltage, this can affect the stability of biomolecules in aqueous solution and, also, the portability of the devices. To overcome this problem, Lai et al. [5] proposed a DNA-hybridization sensor based on OCMFET structure that can operate at very low voltage thanks to a particular hybrid FET's dielectric: the use an aluminium floating gate, instead of a gold one as the sensors reported in [4], permits to employ a combination of a very thin layer of aluminium oxide (AlOx) with a 150 nm thick layer of Parylene C film as gate insulator. This determines a significant increase of the gate capacitance of the structure and, consequently, a significant reduction of the device operating voltages. The sensor showed a very high sensitivity (~0.1 nM) with a good reproducibility (see Fig. 3.6).

Very recently, the OCMFET structure has been used for monitoring, *in vitro,* the electrical activity of living cells [6]. As already explain in Chapter 1, the electrical activity of cells is based on the charge variation related to the rapid ionic displacement occurring across the cell membrane during an action potential. An interesting work, reported in [6], have recently demonstrated that this phenomenon can be easily sensed with an OCMFET structure. Thanks to the biocompatibility of the employed materials, it was possible to grow the cells culture over the sensing area and record their activity as shown in Fig. 3.7.

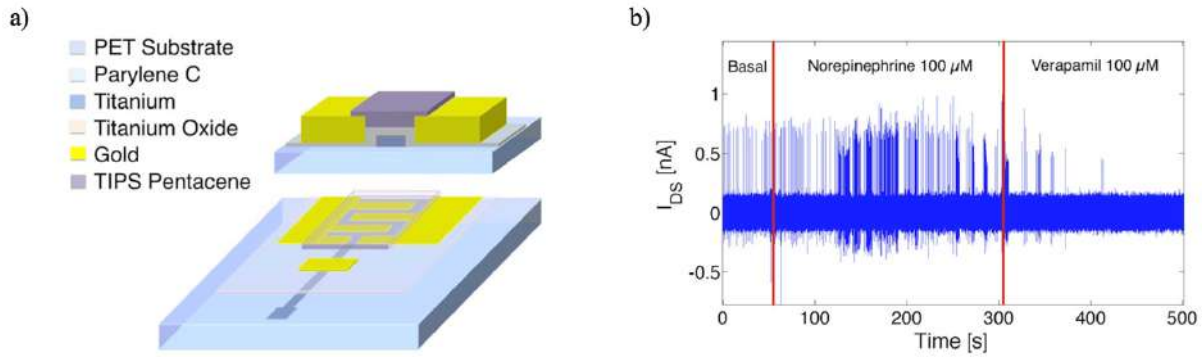

Fig. 3.7: a) Schematic representation of an OCMFET as transducer of the electrical activity of electrogenic cells. b) Dynamic response of the sensor during a normal basal cell's activity, and during an accelerated and suppressed cell's activity. [6]

3.3 OCMFET as temperature sensor

In Chapter 2 were presented different tactile sensors based on piezoelectric/pyroelectric materials. As widely discussed, pyroelectricity is the ability, of some materials, to generate a voltage in response to a temperature variation.

This voltage is related to a modification of the total dipole moment of the molecules, and, in addition, a charge separation is created, meaning that opposite charges are accumulated on the opposite faces of these materials. By exploiting the pyroelectric properties of a polymeric material

(called PVDF), we have developed an efficient temperature sensor for tactile and wearable applications [8] – [9]. Hereafter, the fabrication procedure of this kind of devices is reported together with the experimental results.

3.3.1 Materials and methods

The fabrication process started with the preparation of the plastic substrate. A highly flexible 175 μm thick *poly(ethyletherephtalate)* (PET) substrate was chosen for its mechanical properties and its optical properties (it is completely transparent) and was carefully rinsed with *acetone*, *isopropyl alcohol* (or isopropanol) and deionized water.

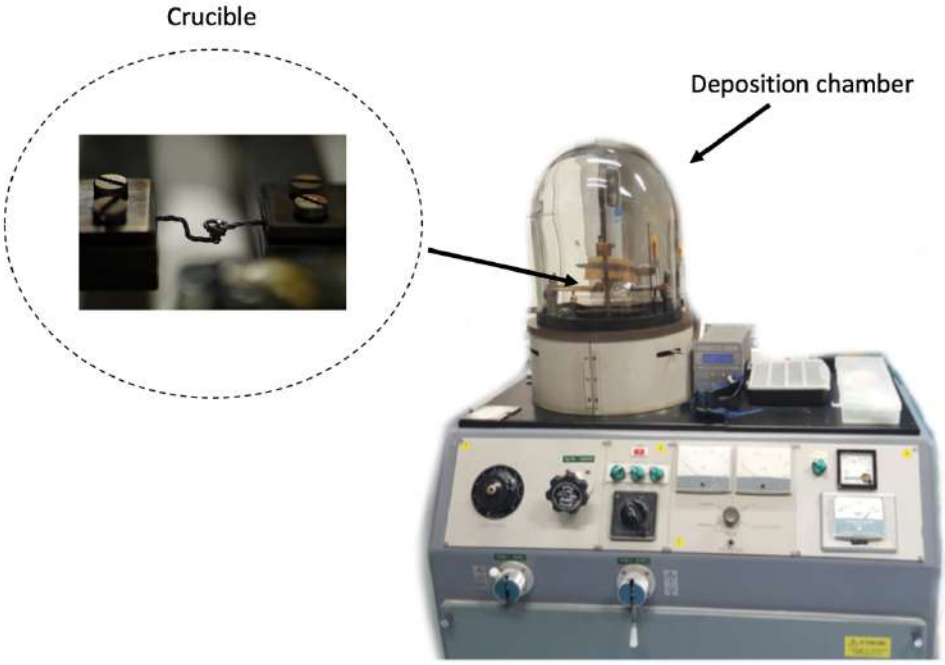

Fig. 3.8: Thermal evaporator unit used in this thesis

An aluminium floating gate electrode (~100 nm thick) was deposited all over the substrate by thermal evaporation: this particular technique is usually used for the deposition of metals (Au, Al, Ti, Ag etc.) and semiconductors (Pentacene, N1400 etc.). The material to be evaporated was placed inside a small tungsten crucible, which is connected to electrodes that can pass high current through it. For this reason, the metal can sublimate by Joule effect and can be deposited onto the substrates put over the crucible.

The patterning of the floating gate electrode was made by standard photolithography: a positive photoresist layer (AZ1518, from Microposit) was deposited onto the plastic metalized substrate by spin coating. After a soft baking step, which was necessary to evaporate the solvent, a photolithographic mask was placed onto the substrate and the system was exposed to UV light for

about 2 minutes. The exposure step is followed by the development of the photoresist layer, in a NaOH solution. The last step is the etching of the metal layer that is not covered by the photoresist, in order to exactly reproduce the mask layout, with an HF solution.

After this process, the gate dielectric is deposited. In order to achieve low operating voltages, we have decided to employ a technique already developed in our labs and reported in [7]. This dielectric film is characterized by the combination of two different, ultrathin, insulating films, namely a thin native aluminium oxide layer (of about 5 nm) and a thin layer of Parylene C (∼150 nm). The metal oxide layer was growth by thermal treatment (50 °C for 12 hours) and the Parylene C was deposited by chemical vapour deposition (CVD) process using a PDS2010 LabCoater from Special Coating Systems. Before the deposition of Parylene C, in order to enhance its adhesion to the metalized substrates, a small amount of sylane (A-174 Sylane) was deposited in the deposition chamber in order to create an adhesion promoter layer. During the deposition process, little PDMS patches were placed over the sensing area which must not be covered by the Parylene C layer.

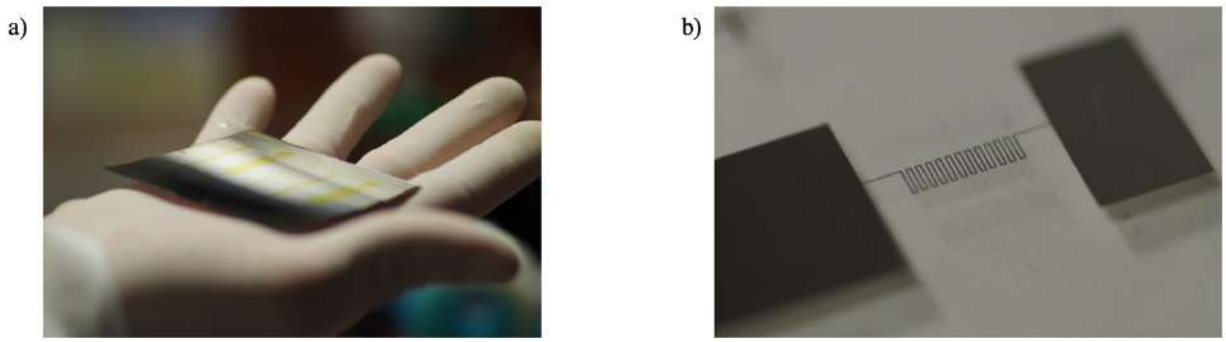

Fig. 3.9: a) Metalizzed PET substrate with photoresist before the metal etching with HF. b) Interdigitated structure for the transistor's channel

This particular hybrid gate dielectric, allowed the low voltage operation of the transistor, due to a high gate capacitance (∼16 nF/cm^2).

Before the realization of source, drain and control gate electrodes, in order to minimize the overlap between source/drain electrodes and the floating gate contact, it has been used a particular technique called *self-alignment*. As already mentioned in section 3.1, the shift of the effective threshold voltage in an OCMFET is expressed by:

$$\Delta V_{THF} = \frac{\Delta Q_i}{C_{TOT}}. \tag{3.8}$$

The overlap between source/drain electrodes and the floating gate, would entail the generation of parasitic capacitance that can cause the reduction of the OCMFET sensitivity due to an increase of the C_{TOT}. Moreover, it is known that parasitic capacitance can significantly reduce the transistor's cut-off frequency, i.e. the frequency for unity current gain, which is expressed by:

$$f_T = \frac{g_m}{2\pi(C_G + C_{par})}. \tag{3.9}$$

In Lai et al. [10] it has been demonstrated that thanks to a simple photolithographic self-alignment process, parasitic capacitances were significantly reduced of more than one order of magnitude. Consequently, as shown in Fig. 3.10, it is possible to increase the transistor's cut-off frequency.

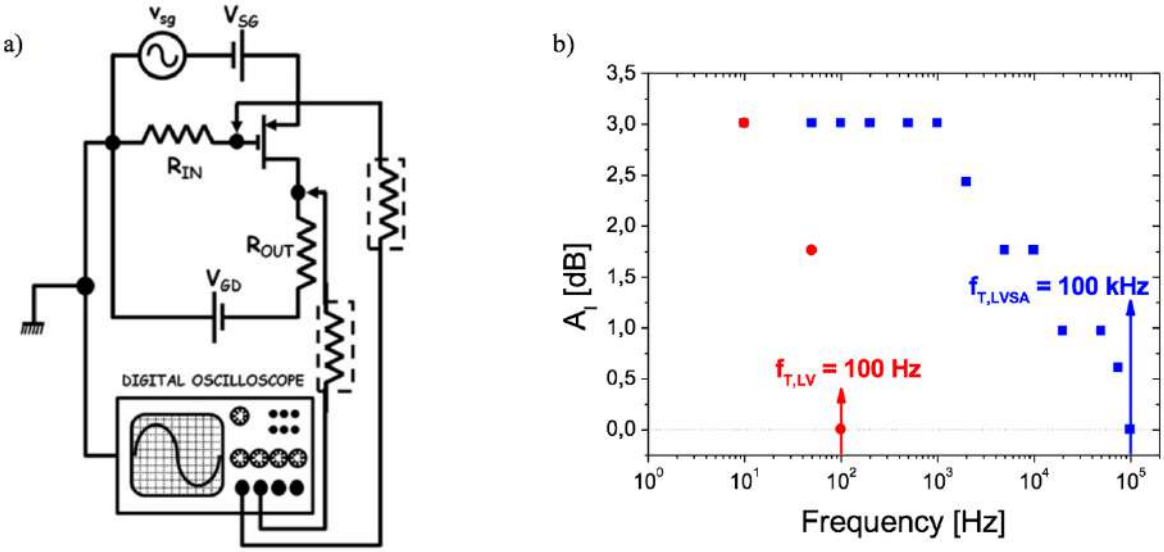

Fig. 3.10: a) Measurement setup for the evaluation of the cut-off frequency. b) Transfer function for the self-aligned OFET (blue points) and no self-aligned OFET (red points) and their cut-off frequency. [10]

This technique, widely descripted in Fig. 3.11, exploit the transparency of the PET substrate and the Parylene C, in order to use the floating gate as a mask during the photolithography process for the realization of source and drain electrodes. At first a layer of positive photoresist was deposited over the Parylene C and a photolithographic mask was placed over it. Then the sample was exposed to UV light through the back side and the front side of the transparent substrate (see Fig. 3.11 – Step 4): the photoresist not cover by the mask and by the floating gate was developed and then etched by NaOH solution. After this step, the photoresist covered only the part over the gate insulator in correspondence of the transistor channel (see Fig. 3.11 – Step 6).

The last step of the fabrication process was the deposition of source and drain contacts in the transistor area and of the control capacitors. Thanks to the good interface with p-type organic semiconductor (as Pentacene or Pentacene TIPS for instance), gold was employed for all these components. The metal was thermally evaporated in vacuum ($\sim 10^{-5}$ Torr) over the Parylene C. By rinsing the device with acetone, the gold deposited onto the photoresist was removed, thus defining the transistor channel reproducing the geometry of the underlying gate electrode. Finally, the source, drain and control gate electrode were patterned by photolithography, according to the same procedure already introduced for the floating gate. As only relevant difference, the chemical

etching of gold was performed using a potassium iodide (KI) solution (40:4:1 H_2O:KI:I_2). An interdigitated structure was used for the channel in order to increase the width/length ratio (W/L = 630) and, consequently, the transistor output current.

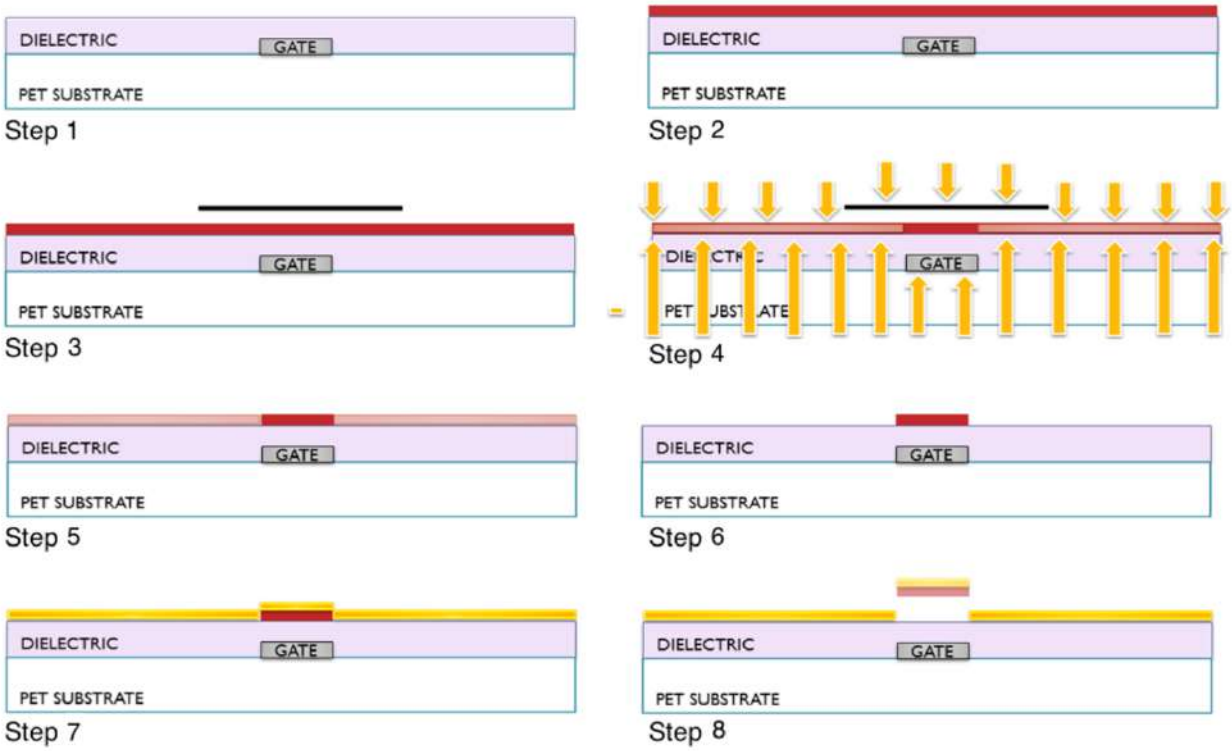

Fig. 3.11: Different steps for the self-alignment technique. Step 1: cleaning of the substrate. Step 2: deposition of the photoresist over the Parylene C. Step 3: placing of a mask over the sample. Step 4: exposure of the sample to UV light. Step 5-6: only the photoresist expose to UV light is developed and etched by NaOH solution. Step 7: deposition of gold over all the sample. Step 8: the photoresist is removed using acetone (lift-off step). After the lift-off the gold is removed from the channel regions.

TIPS Pentacene (6,13-Bis(triisopropylsilylethynyl)pentacene) was used as p-type organic semiconductor. A solution of 0.5 wt% in toluene was dropcasted on the channel area. After deposition, the device was annealed at 80 °C on a hot plate for 30 minutes in order to increase the crystallinity of the film and to remove all the residual solvent.

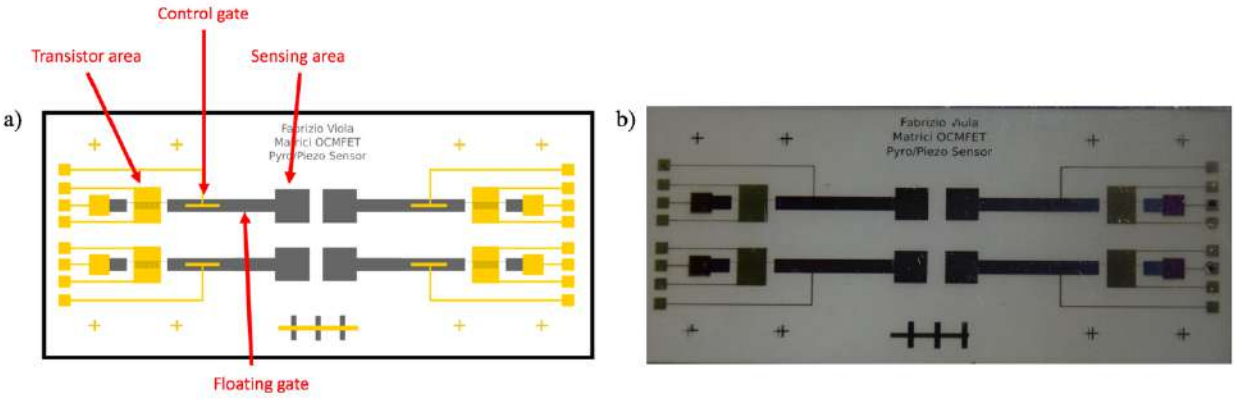

Fig. 3.12: a) Schematic representation and b) image of four OCMFET devices.

In the first part of this thesis, a 28 μm-thick PVDF film, already poled, (Measurement Specialties Inc.-MEAS) was sandwiched between two metal layers in order to form a capacitor (Area = 1 × 1 cm^2, C = 380 pF/cm^2), and connected by a metal wire with the floating gate of the transistor. The two electrodes were made of silver and patterned by inkjet printing.

3.3.2 Experimental results

In Fig. 3.13, the typical measurement setup for temperature measurements is shown. A Keithley 2636 SourceMeter, controlled by a custom Matlab® scripts, was employed to bias the devices and acquire the corresponding currents. During the temperature measurements, the sensing area was wire connected with a PVDF capacitors which was placed over a Peltier cell powered by a Power Supply. The Peltier cell works thanks to the Peltier effect i.e. the possibility to create a temperature difference by transferring heat between two electrical junctions when a DC voltage is applied between them. The real temperature of the PVDF and the Peltier cell was monitored through a RTD sensor.

First, the devices were characterized at room temperature (about 22°C) without the PVDF connected with the floating gate, in order to evaluate the electrical performances (mobility, hysteresis and leakage current) of the OCMFETs.

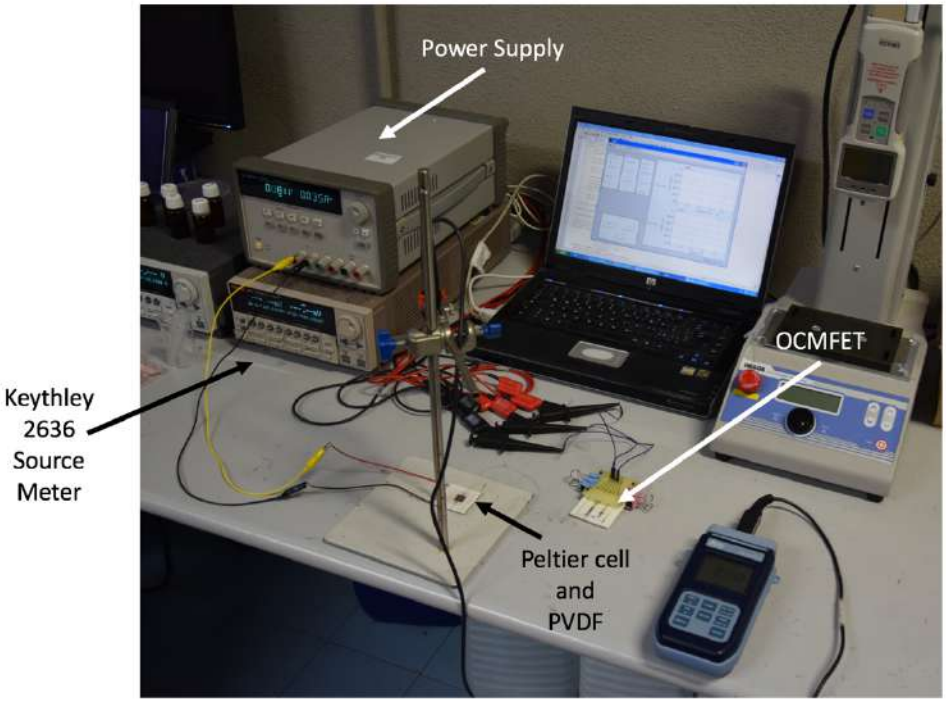

Fig. 3.13: Experimental setup for temperature measurements.

In Fig. 3.14 are reported output and transfer characteristics of one device, thanks to the high

capacitance coupling due to the ultrathin double layer gate dielectric, the OCMFET can be operated at very low voltage (in this case V_{th} = – 0.35 V) giving rise to very good electrical performances, with a semiconductor mobility of 0.2 cm^2/Vs, almost negligible hysteresis, remarkably small leakage current, generally around 100 pA. A preliminary experiment was done in order to prove that the devices response indeed depends on the orientation of the PVDF film.

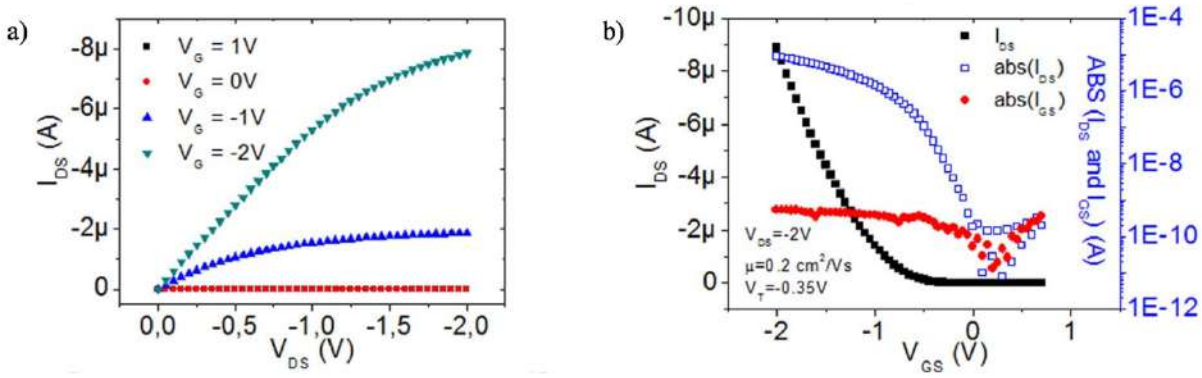

Fig. 3.14: a) output and b) transfer characteristics of the low voltage OCMFET. [8]

As introduced in Chapter 2, a thermal/mechanical stress can generate a voltage in a pyro/piezoelectric material due to an accumulation of opposite charges in the opposite faces of the material. For this reason, if the sensing area of the floating gate is connected with one plate of the PVDF capacitor we should observe a shift of the threshold voltage in one specific direction, whereas, if the sensing area is connected to the opposite plate of the PVDF capacitor, the same external stimulus must induce a shift of the threshold voltage in the opposite direction of the previous case.

This particular *flipping test* has been made in order to understand if the variations in the output current I_{DS} observed in the fabricated OCMFETs are related to the pyro/piezoelectric properties of the materials instead of other undesired effects. In this case the PVDF capacitor was placed on a Peltier cell (starting T = 22 °C) and connected using the DOWN configuration (i.e. in which the floating gate was connected with the PVDF face named “DOWN”).

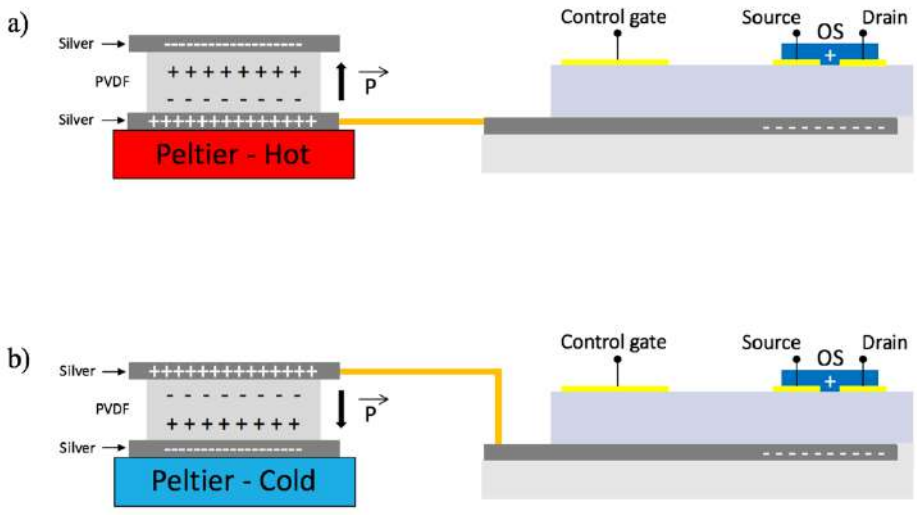

Fig. 3.15: Flipping test. a) PVDF connected to the OCMFET with the "UP" configuration and b) with the "DOWN" configuration.

At first it has been cooled down to 0 °C, thus inducing negative charges on the PVDF bottom electrode; as a result, a marked increase of the current was observed. Afterwards, the temperature was restored and as a consequence the current came slowly back to its previous value. Interestingly, when T is increased up to 36 °C and 38 °C a decrease of the current can be observed, which, again, has been found to be fully reversible, as it came back to its initial value when T has been restored to 22 °C.

On the other hand, when the UP configuration was employed (i.e. in which the floating gate was connected with the PVDF face named "UP"), increasing the temperature leads to a clear increase of the current; this evidence can be justified only by the fact that changing the connections with the PVDF capacitor, the same thermal stimulus induces a different sign of charges into the OTFT channel.

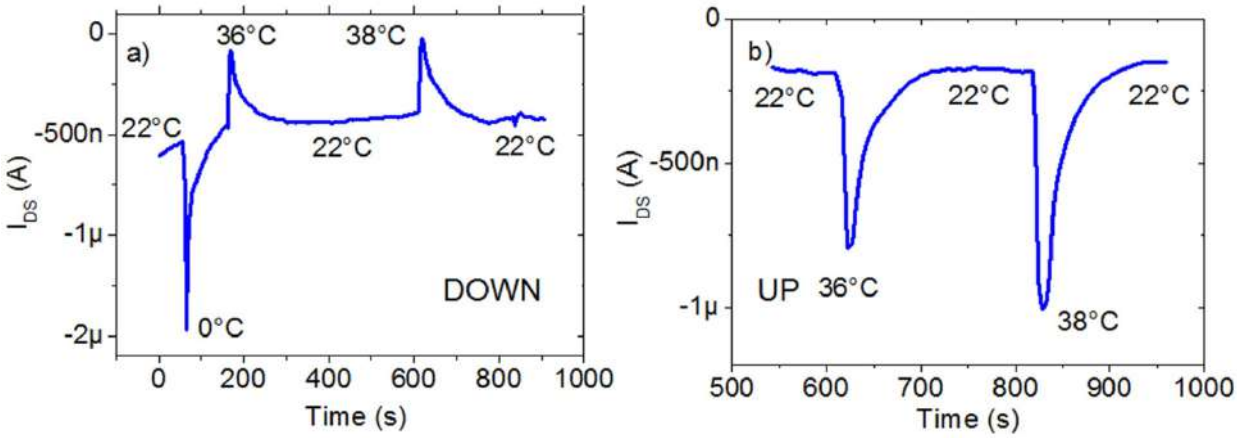

Fig. 3.16: Current variations induced by external thermal stimuli on the same device connected a) in the DOWN configuration and b) in the UP configuration. [8]

A more detailed thermal characterization was subsequently performed using the UP configuration

for monitoring positive T and the DOWN configuration for negative T, i.e. in order to operate the devices in over-threshold regime in both cases. In this set of experiments, the PVDF capacitor was placed on the Peltier cell, and the temperature was increased (decreased) step by step, measuring, at the same time, the output current.

As can be seen in Fig. 3.17, each temperature step induces a variation of the current, reaching a plateau once the induced temperature on the PVDF gets constant. From this characterization, it is possible to estimate the current variations induced by each T. In Fig. 3.18, we report the results obtained for each device on which we have performed at least 5 cycles for each temperature step. As expected, an increase of the device output current was observed for both positive and negative temperature variations with respect to the room temperature, set in all measurements at 22 °C.

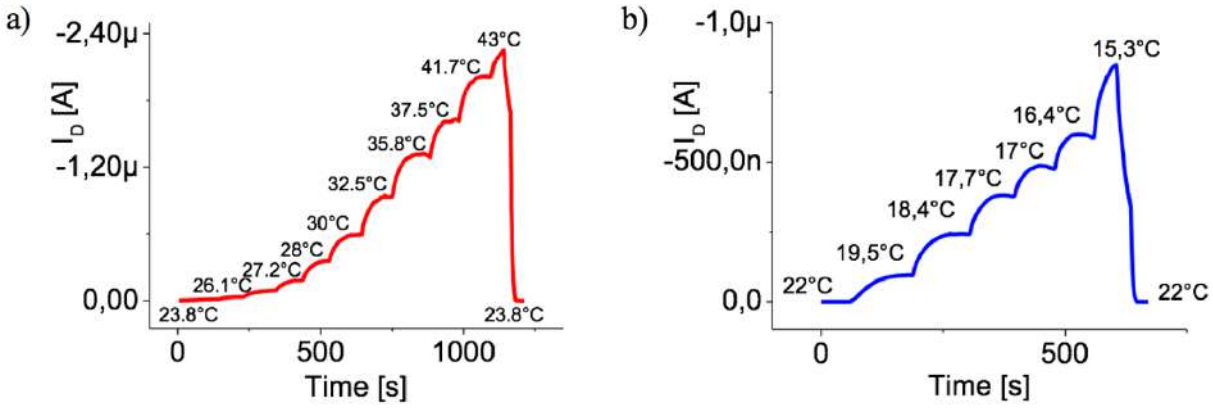

Fig. 3.17: a) and b) Output current variations induced by temperature. [8]

The electrical characterization demonstrates that the response to positive and negative temperature variations gives rise to a very reproducible, linear response, with a constant slope in the whole range of temperatures. Therefore, from this preliminary characterization, we can conclude that a temperature range from 10 °C up to 42 °C, typically requested in tactile sensing applications, can be reliably monitored with this approach.

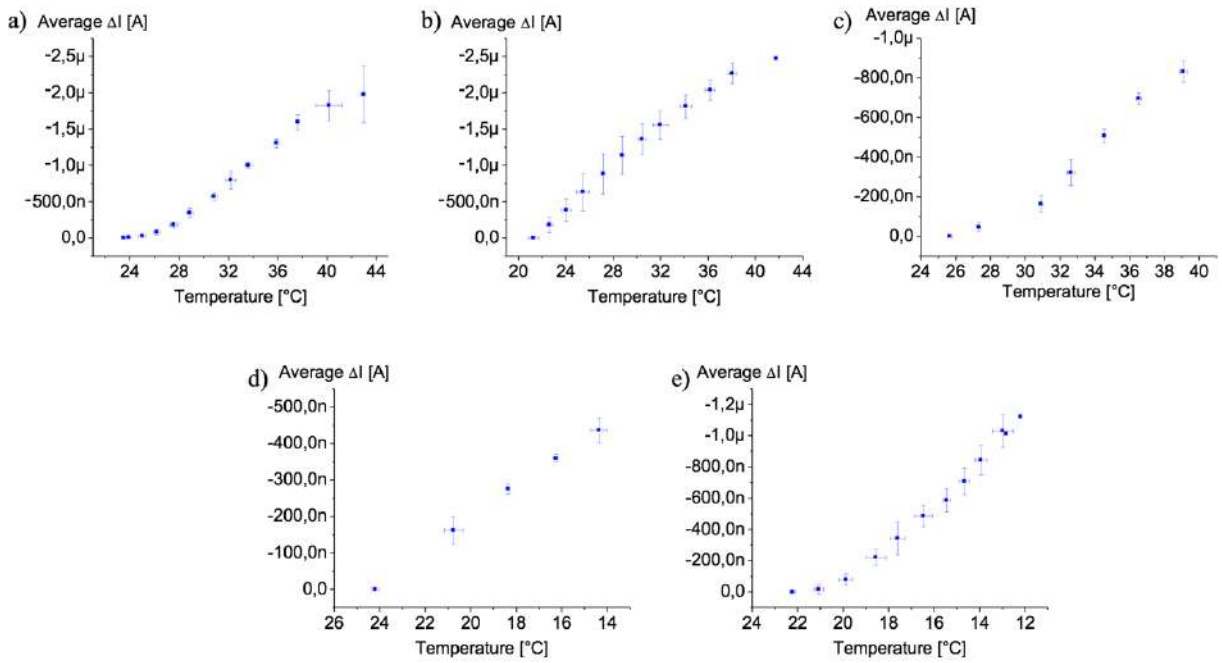

Fig. 3.18: Calibration curves of different sensors. In a), b) and c) are reported measurement made with the device in UP configuration, while d) and e) measures have been obtained with the device in DOWN configuration.

Afterwards, we compared the dynamic response of the OCMFET as temperature sensor with these of an infrared thermometer (PyroCouple PC21MT-1 - CALEX Electronics Limited). The results are reported in Fig. 3.19, in which the current variations induced by temperature are plotted together with the measured sensing area temperature.

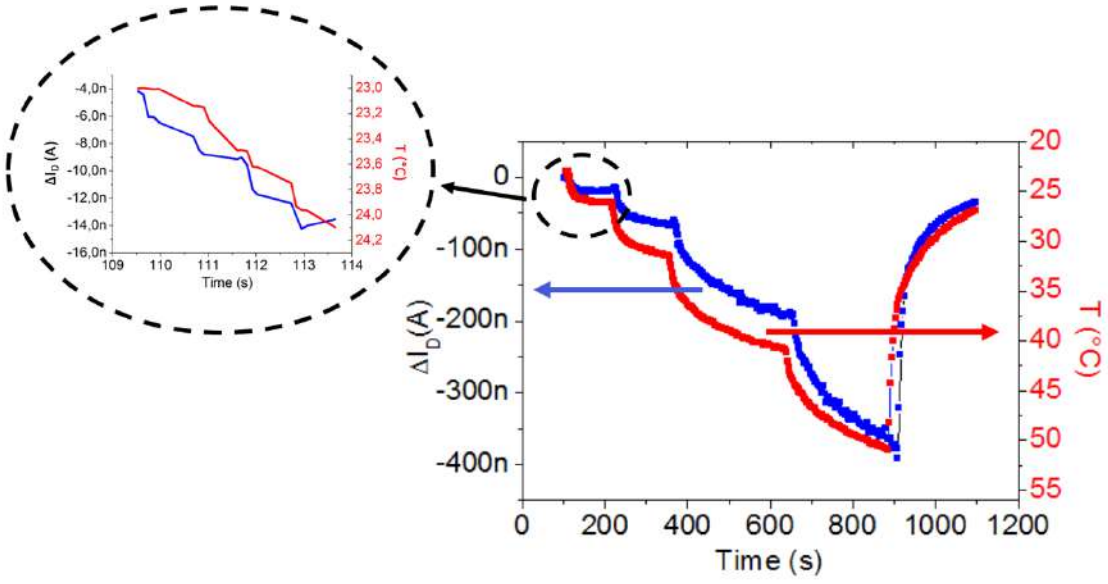

Fig. 3.19: Output current variations induced by temperature (blue curve) and temperature variations measured on the sensing area (red curve). [9]

From this graph it can be clearly observed a clear response of the sensor to each temperature variation. The long time required by the system to reach a steady state is mainly dictated by the

dynamics of the Peltier cell. However, apart from a small delay due to data acquisition, the dynamic of the device response very nicely reproduces the real temperature variation (induced by the Peltier cell) on the sensing area, meaning that the response time of the pyro-OCMFET is comparable to the one of the commercial infrared thermometer used for these experiments. In addition, our sensor is able to detect very small temperature variation (see the insert in Fig. 3.19) with a resolution comparable to the infrared thermometer (< 0.2 °C).

3.4 OCMFET as static force sensor

As widely discussed in Chapter 2, all the pyroelectric materials are also piezoelectric i.e. they accumulate charge on their opposite faces when they are subject to any kind of mechanical stresses. These materials exhibit a good high-frequency response and a high sensitivity and, consequently, are particularly suited for sensory applications. By exploiting the working principle of the OCMFET structure, which is a charge sensor, with the piezoelectric property of PVDF, we have also developed a tactile static force sensor [12], by using the same materials and the same fabrication process of the reported temperature sensor.

3.4.1 Materials and methods

According to the fabrication process reported in section 3.3.1, the core of the device was a floating gate OTFT biased through a control capacitor and connected to the transducer material element via the floating gate. The floating gate was fabricated by depositing and patterning a thin aluminium layer over a flexible poly(ethylene therephtalate) (PET) film. After that, an ultrathin insulating layer was fabricated by using a hybrid organic/inorganic structure, composed by a combination of alumina and Parylene C. Gold Source and Drain and also the control gate were then patterned on the insulating film using a standard photolithographic process.

The 6,13-Bis(triisopropylsilylethynyl)pentacene (TIPS pentacene, Sigma-Aldrich) was used as p-type organic semiconductor. A solution of 0.5 wt% in toluene was drop-casted on the channel area. After deposition, the device was annealed at 80°C on a hot plate for 30 minutes in order to increase the crystallinity of the film and to remove all the residual solvent. The control gate electrode was used for setting the working point of the sensor.

3.4.2 Experimental results

The device working principle is very simple: when an external mechanical force is applied on the PVDF layer, the charge displacement in the piezoelectric film, described in by Equation 2.8 induces a charge separation in the floating gate electrode, which, in turn, causes a modulation of the transistor threshold voltage:

$$D_i = d_{im}\sigma_m, \tag{2.8}$$

where **D** is the *electric displacement*, **d** is the *piezoelectric coefficient* and σ is the applied mechanical stress. As a consequence, a channel current variation can be detected at each force event. The change in the carrier density is dictated by the sign of charges induced into the floating gate, which depends on which of the two electrodes of the PVDF capacitor is connected with the floating gate.

In Fig. 3.20, the typical measurement setup for force measurements is shown. A Keithley 2636 Source Meter, controlled by a custom Matlab® scripts, was employed to bias the devices and acquire the corresponding currents. During the force measurements, the sensing area was wire connected with a PVDF capacitors which was placed under a mechanical indenter, showed in Fig. 3.20, connected with a dynamometer (IMADA – Force Gauge) which was used to apply controlled force on the PVDF surface.

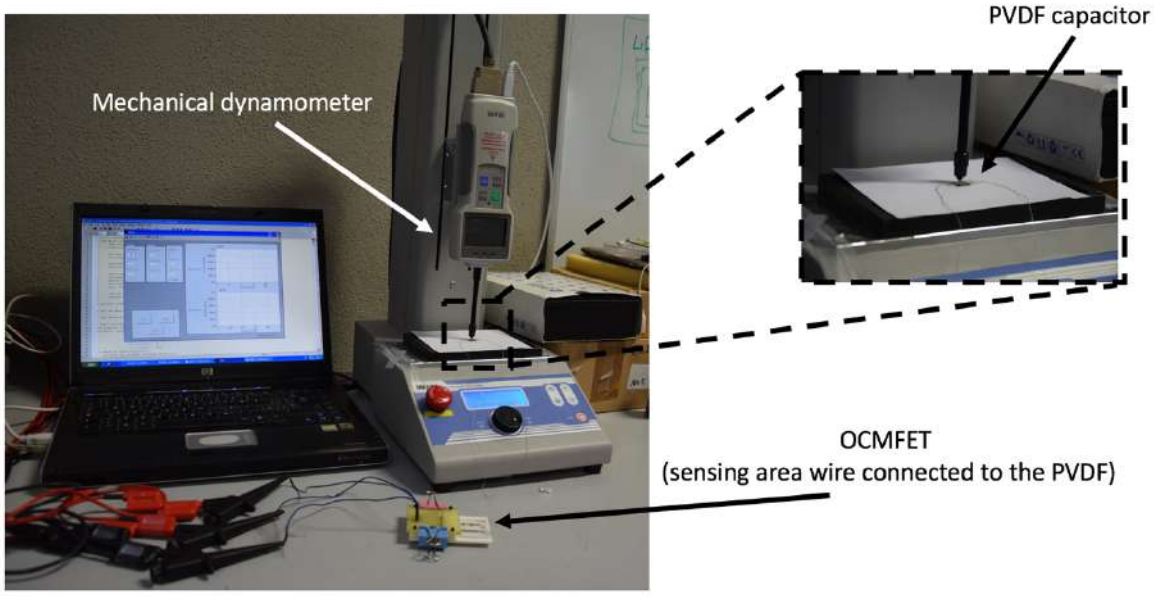

Fig. 3.20: Experimental setup for force measuremets.

As shown in Fig. 3.21, in order to mechanically decouple the OTFT device with the PVDF film, the piezoelectric polymer was wire connected with the sensing area of the OCMFET. In this way

only the PVDF film was mechanically stimulated during all the measurements, allowing us to attribute the variation of the output current of the transistor as a result of force applied on the PVDF film.

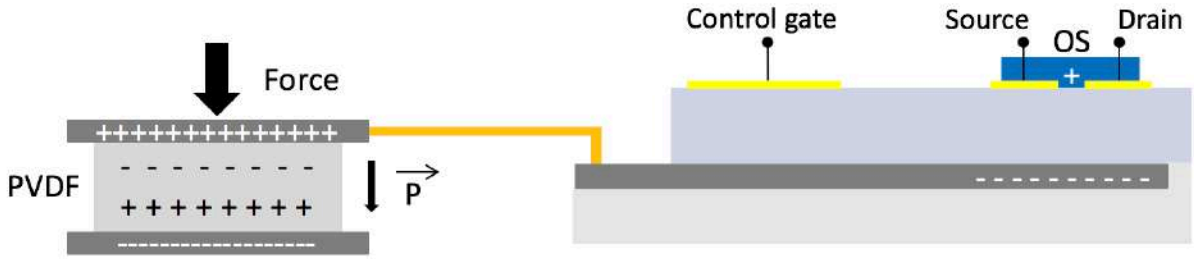

Fig. 3.21: Schematic representation of the force sensor based on an OCMFET integrated with a piezoelectric polymer.

At first, the devices were characterized without the PVDF connection with the floating gate, in order to evaluate the electrical performances (mobility, hysteresis and leakage current) of the OCMFET (see Fig. 3.22).

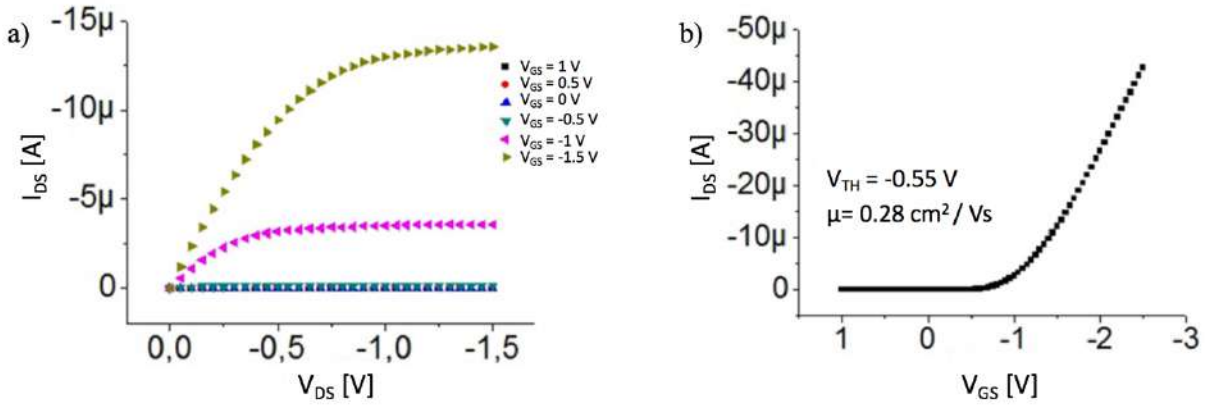

Fig. 3.22: a) Output and b) transfer characteristics of the low voltage OCMFET. [12]

All the measurements were performed by biasing the device with a constant V_{DS} and a constant V_{GS}. The voltage V_{GS} was applied via the control gate electrode in order to set a similar working point to each transistor. In all the performed measurements a preload of 0.5 N was applied to the PVDF sensing element and, as shown in Fig. 3.23, the applied force was increase step by step and the output current was recorded.

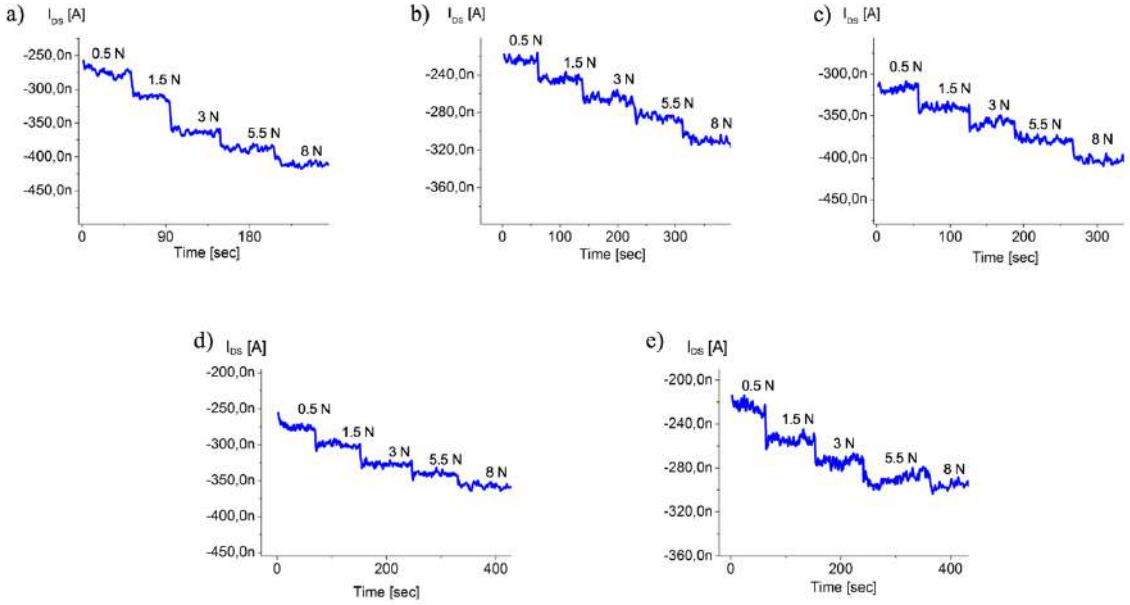

Fig. 3.23: a) - e) Dynamic response of different tactile force sensors.

The electromechanical characterization demonstrates that the proposed approach can be used for detecting static forces within a range from 0.5 N up to 8 N. Moreover, the response shown in Fig. 3.24 is approximately linear over the tested range, with a good reproducibility. The sensitivity of the sensors is ~ 8 nA/N.

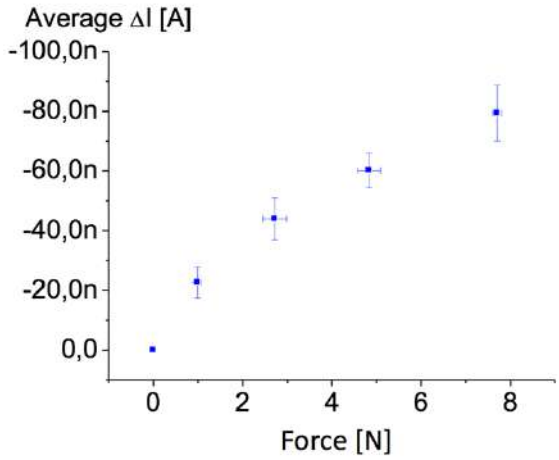

Fig. 3.24: Statistics of the calibration curves obtained from the electromechanical characterization in the range from 0.5 N to 8 N. [12]

3.5 OCMFET as dynamic force sensor

In Chapter 1 it has been descripted the human's somatosensory system with a particular focus on the characteristic of thermoreceptors and mechanoreceptors. In particular, mechanoreceptors can

be divided into two categories, depending on the kind of the forces that can sense: SA units can usually detect static forces and RA units dynamic forces in the range between [40 – 400 Hz].

Consequently, e-skin must have the capability to detect not only static forces, as the approach that we presented in [12], but also dynamic forces. As already discussed in section 3.3.1, self-aligned OCMFETs can achieve high cut-off frequency (∼100 KHz), which makes it particularly suitable for high frequency applications. In addition, PVDF transducers exhibit a high electromechanical transduction frequency bandwidth (from 0.001 Hz to 1 GHz) as reported in the Meas. Spec. PVDF datasheet [11]. For this reason, we have investigated the possibility to exploit the properties of PVDF piezoelectric polymer coupled with OCMFET structures, in order to develop a dynamic tactile force sensor for e-skin applications [13].

3.5.1 Materials and methods

PVDF samples have been fabricated using already stretched and poled, 110 μm thick PVDF films from Measurement Specialties Inc.- MEAS (nominal capacitance: 110 pF/cm^2). Two inkjet printed silver ink electrodes (1 cm^2 each) have been realized onto both sides of the film with a Dimatix material printer 2831, using a commercial silver ink (Cabot conductive ink CCI-300) and the film was post-baked at 60 °C for 48 h. This low-temperature post-printing step allowed obtaining conductive silver ink electrodes (with a measured bulk resistivity of 150 mΩ cm) without affecting the PVDF film ferroelectric properties. As shown in Fig. 3.26, in order to perform the electromechanical characterization, and to mechanically decouple the OCMFET structure and the sensing PVDF film, the latter was mounted onto a custom PCB and wire-connected, either the top or the bottom contact of the PVDF film, to the floating gate of the OCMFET using a coaxial cable while the other contact was left floating. Finally, a 5 mm-thick PDMS layer was glued on top of the PVDF film for stress transmission and sensor protection.

OFET devices were fabricated onto a 175 mm thick polyethylene terephtalate (PET) sheet. The aluminum floating gate and the self-aligned gold source, drain, and control gate contacts have been realized using a standard photolithographic process, while the gate dielectric was made of a thin layer (about 5 nm) of native Al_2O_x and a layer of Parylene C (Specialty Coating System) deposited through chemical vapour deposition at room temperature. At the end, a droplet of a 6,13-Bis(triisopropylsilylethynyl) pentacene solution in anisole (1% wt) is deposited directly over the transistor channel region in order to obtain a bottom-gate/bottom-contact OFET structure (see Fig. 3.25).

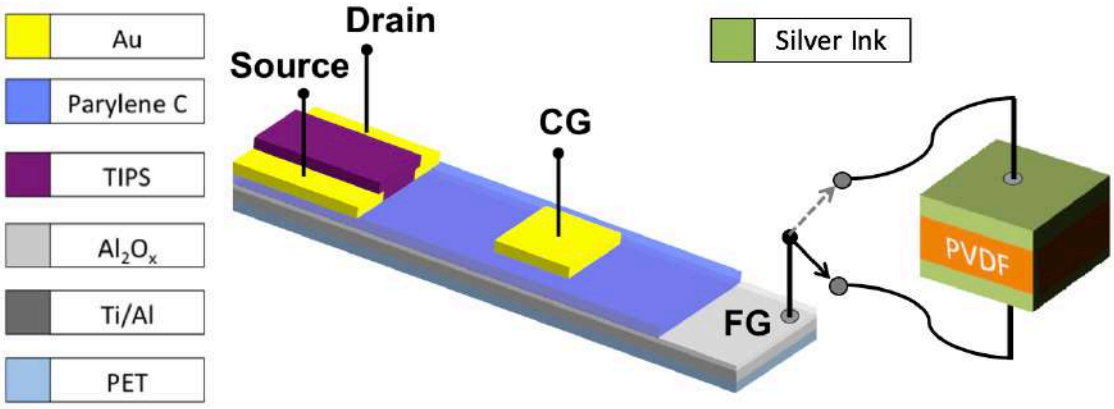

Fig. 3.25: Structure of the sensor and employed materials, the OCMFET floating gate is connected to either top or the bottom contact of the PVDF film. [13]

The experimental setup for sensor mechanical stimulation, showed in Fig. 3.26, consisted of a rigid frame with a lower fixed plate to which an electromechanical shaker (Brüel&Kjaer, Minishaker Type 4810 with Power Amplifier Type 2706) was assembled. The patterned PVDF film was rigidly coupled to the shaker. The upper head of the frame included a soft (spherical) indenter and a piezoelectric force transducer (ICP Force Sensor, Model 208C02 from PCB Piezotronics Inc.). The whole upper head can be positioned through adjusting screws at various distances with respect to the lower plate. Regulations of this screw also defines the amount of mechanical preload on the PVDF sensor (which was 4 N for all the performed experiments). The loading chain is formed, accordingly, by: shaker, PVDF film, indenter, and force transducer. All these elements have been accurately aligned before any test.

Forces at different frequencies and amplitudes were applied directly on the PDMS patch covering the PVDF film using the shaker controlled by a waveform generator, and the transistor output current was conditioned by a custom readout electronics that also contains a biasing circuit for OFET polarization ($V_{DS} = V_{GS} = -2$ V for all the devices). The conditioned OFET output and the applied force were simultaneously acquired using a National Instruments board. All the reported experiments have been performed in stable ambient conditions, i.e. at the same light, temperature, and humidity conditions. Moreover, during the experiments, both the OCMFET and the PVDF film were placed inside a Faraday cage in order to minimize the effect of surrounding electromagnetic fields.

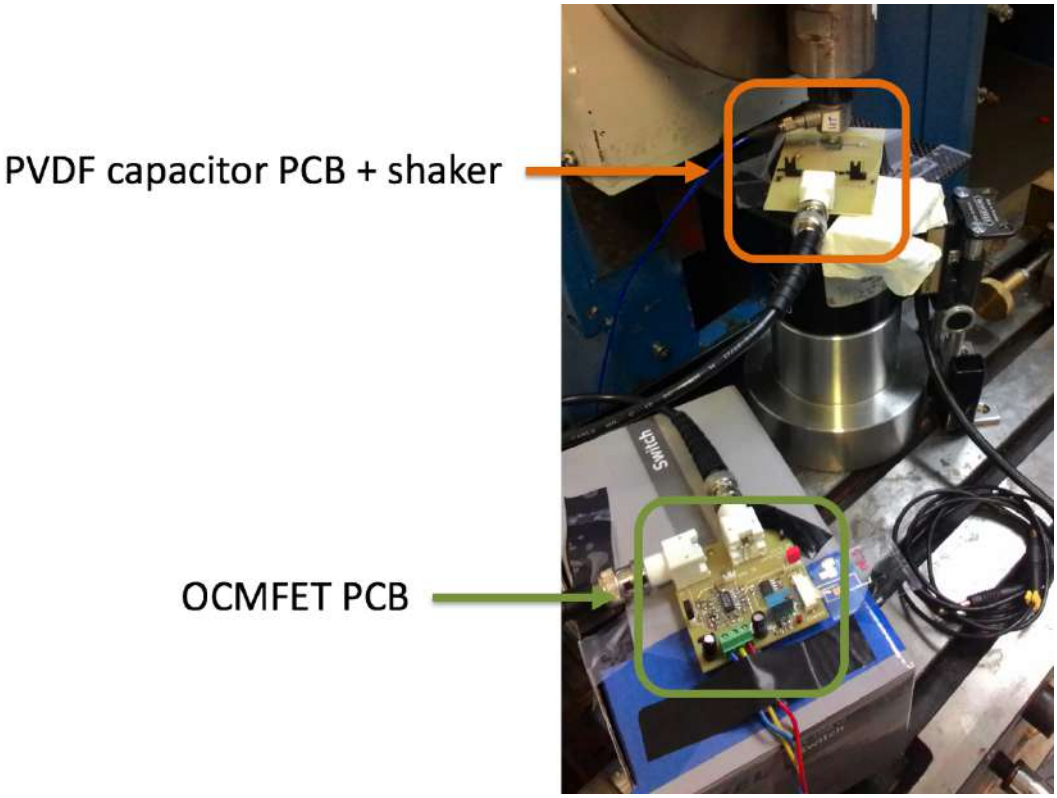

Fig. 3.26: Experimental setup. The PVDF capacitor is mounted on a PCB under the mechanical indenter of the shaker and connected to the floating gate of the OCMFET, which is mounted to a second PCB far from the dynamometer.

3.5.2 Experimental results

Before the actual experiments, each transistor has been fully characterized (using either a Keithley 2636A or an HP4142b) in order to evaluate its electrical performance.

At first, in order to validate the proposed sensing mechanism (i.e. the direct charge transduction), all device currents have been preliminarily monitored while either the top or the bottom contact of the PVDF film was connected to the floating gate (flipping test). During a mechanical stimulation, two equal and opposite charges are induced on the two opposite sides of the PVDF film: as a consequence, a threshold voltage shift is induced in the OCMFET device, since

$$\Delta V_{TH} = \frac{\Delta Q_{PVDF}}{C_{TOT}}, \tag{3.9}$$

where ΔQ_{PVDF} is the time varying charge induced by the PVDF during mechanical stimulation and C_{TOT} is the sum of the PVDF capacitance, the control gate capacitance, and the parasitic capacitances due to the superposition between source, drain, and floating gate.

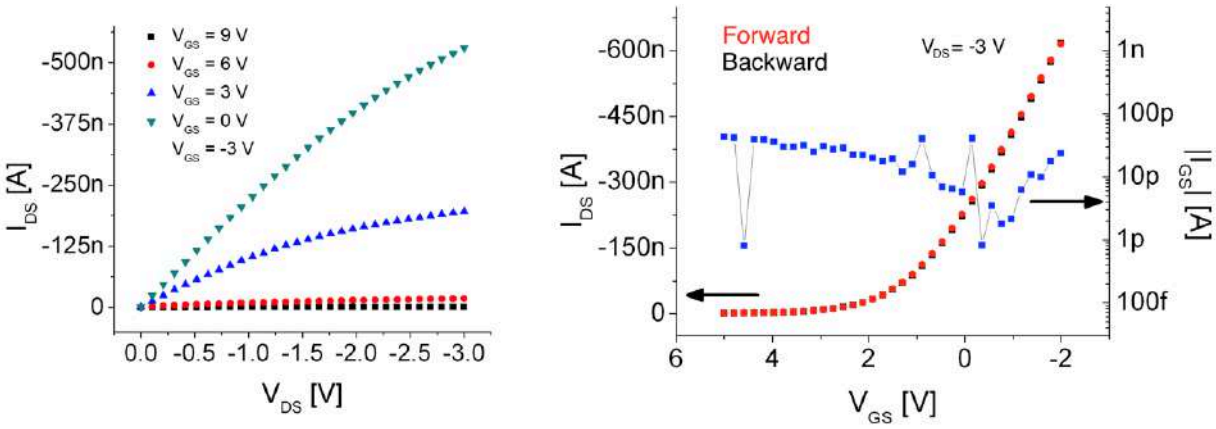

Fig. 3.27: Output and transfer characteristics of OCMFET device for pressure sensing. The device shows no hysteresis and low leakage current. [13]

According to the PVDF side connected to the floating gate, a different sign of threshold voltage shift is induced on the transistor. The obtained results are reported in Fig. 3.28.

From these plots, two important results can be highlighted. First of all, in both cases it can be clearly observed that the sensor is capable to perfectly follow the input mechanical signal applied by the shaker to the PVDF film. Most importantly, it can be also noticed that, by connecting the floating gate of the OCMFET to the two different PVDF electrodes, the phase of the sensor response is shifted by 90°, according to the fact that the induced opposite charge in the floating gate leads to a threshold voltage shift in the opposite direction. This is very important because it demonstrates that the output signal is actually a transduction of the charge induced by the mechanical stimulation of the PVDF film.

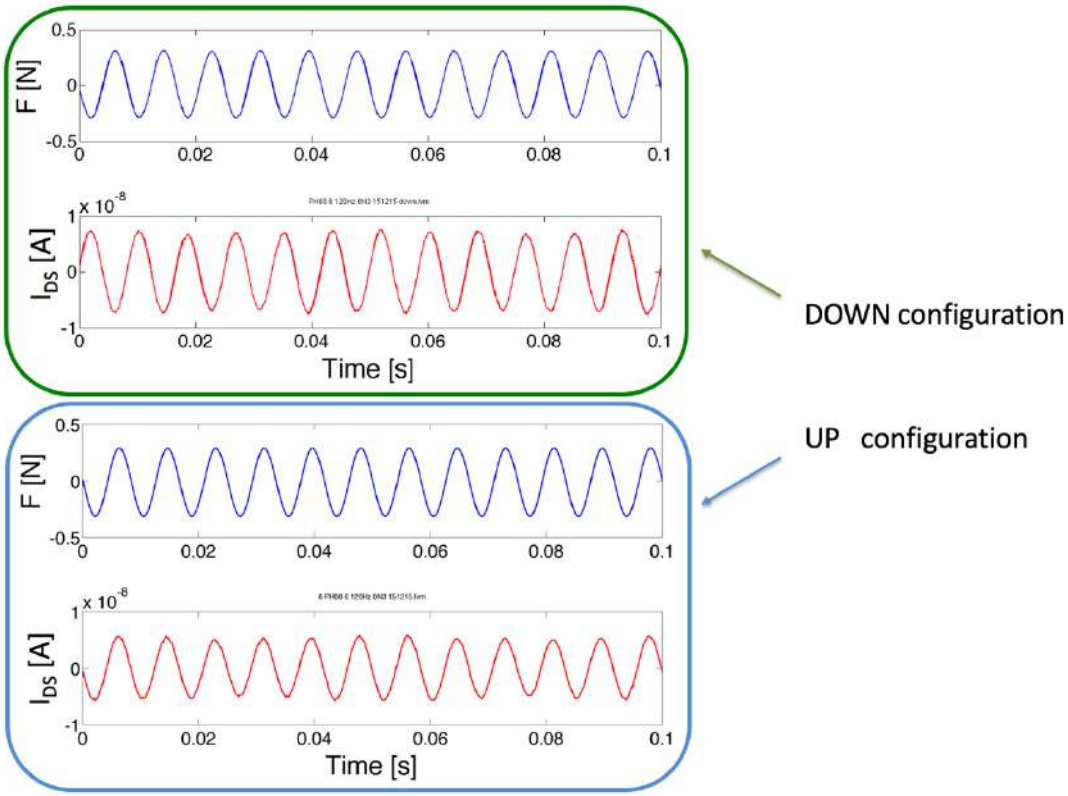

Fig. 3.28: Flipping test, respectively PVDF bottom and top contact connected to the floating gate. [13]

A detailed electromechanical characterization was afterwards performed, by fixing the frequency of the applied mechanical stimulus and changing its amplitude and vice versa. As can be observed from the calibration curve reported in Fig. 3.29 (error bars represent the standard deviation over ten I_{DS} peak-to-peak values), the OCMFET tactile sensor presents a linear response in a wide force range (20 mN – 3.5 N). From the calibration curves, acquired for different frequencies, the sensor sensitivity has been measured. Interestingly, it has been observed that the OCMFET sensitivity is almost constant within a frequency range 20 – 240 Hz, as showed in Fig. 3.29. Finally, the OCMFET-PVDF device has been also tested using mechanical stimuli at higher frequencies. The obtained results clearly demonstrate that the sensor is able to detect very small forces, as low as 20 mN, corresponding to an applied pressure of 300 Pa, and up to 500 Hz, as depicted in Fig. 3.30.

However, it was also noticed that in this range of frequency, the sensitivity is much higher than that obtained in the previous reported range. We assume that this could be due to resonance phenomena such as structural vibrations of the system for that specific frequency.

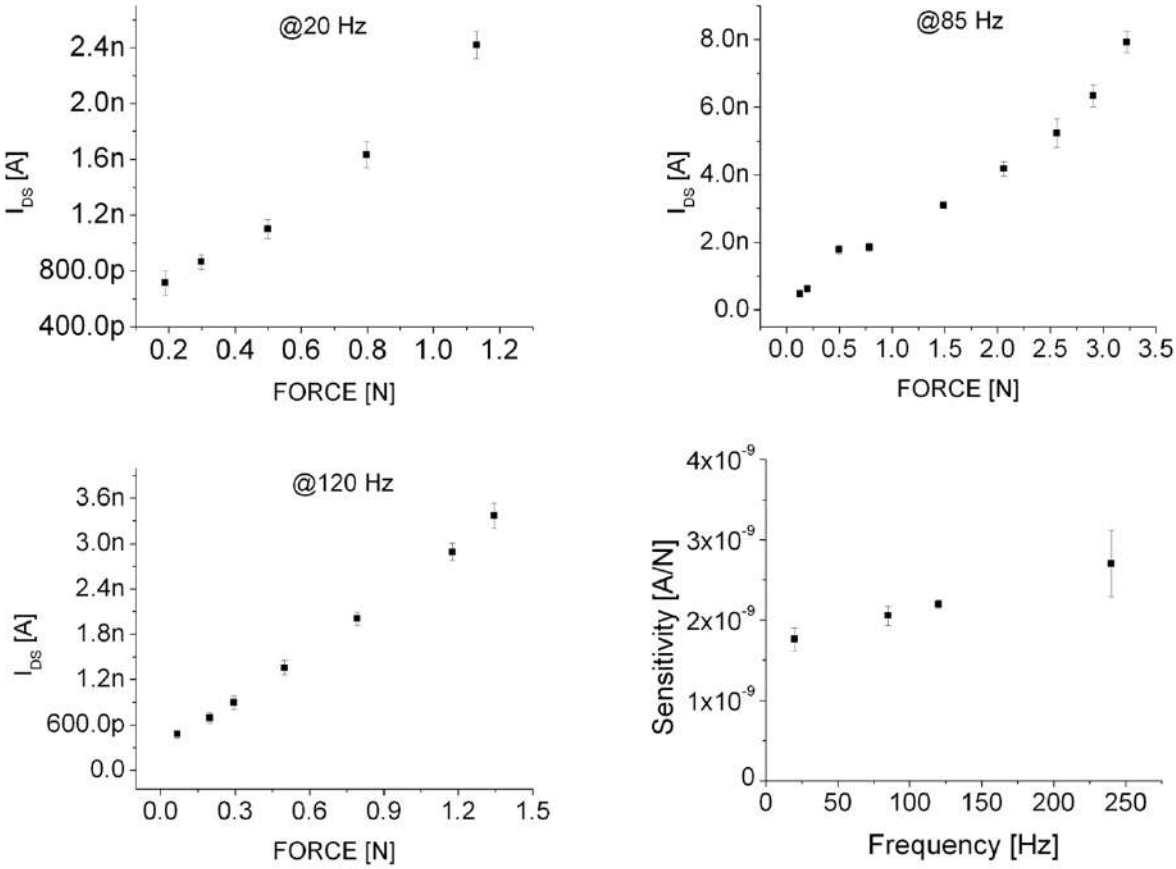

Fig. 3.29: OCMFET response versus applied Force and sensitivities. Errors bars represent the standard deviations (each point has been obtained from 10 peak-to-peak values). [13]

The proposed device is able to transduce applied pressure as low as 300 Pa in a wide frequency range with good reliability. Thanks to the peculiar structure of the OCMFET, the piezoelectric material and the actual amplifying transistor can be physically decoupled, thus making this approach highly adaptable to different design solutions and materials.

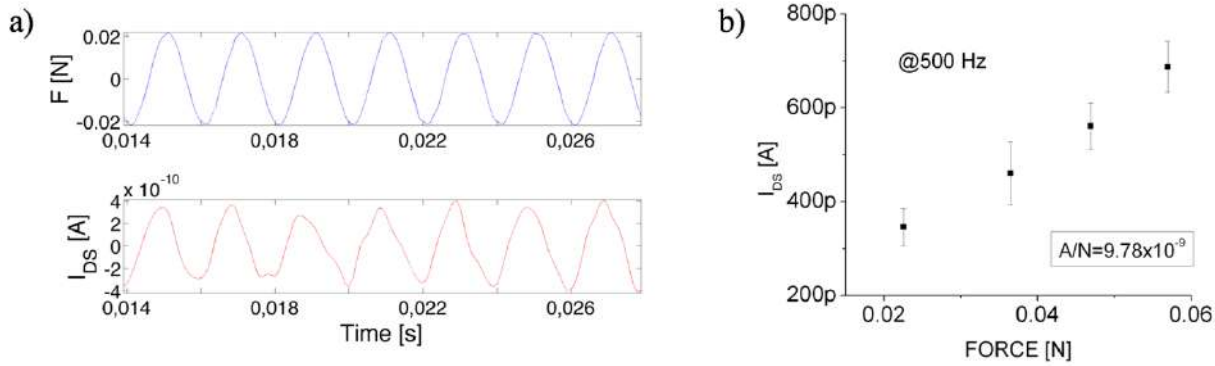

Fig. 3.30: a) Minumum detectable force at 500 Hz, the sensor has been able to sense forces down to 20mN, corresponding to an applied pressure of 300 Pa. b) I_{DS} vs Force, at the maximum frequency of the mechanical stimulation. [13]

3.6 OCMFET as bimodal sensor

In [8], [9], [12] and [13] we reported temperature and force sensors for e-skin applications. We have investigated and demonstrated that our sensors have the following characteristics:

- force resolution, ~ 20 mN.
- Force range, [0.02 – 10] N.
- Bandwidth, [0 – 500] Hz.
- Response time, ~ 2 msec.
- Thermal resolution, ~ 0.2 °C.
- Temperature range, [0 – 55] °C.

These characteristics are comparable to those of the human somatosensory systems, widely discussed in Chapter 1. However, the transduction mechanism of our approach is the same for the temperature sensors and for the force sensors: by exploiting the piezoelectric and the pyroelectric properties of the PVDF, is possible to shift the OCMFET threshold voltage and the output current. This could be a problem in order to discriminate the two different responses. Referring to the sensitivities of the OCMFET based thermal sensor (S_T ~ 115 nA/°C) and the OCMFET based mechano sensor (S_F ~ 10 nA/°C) it is possible to see that the two responses lie in a very different range. This can be explained by taking into account the two most important parameters of the PVDF: the pyroelectric constant and the piezoelectric constant which are related to the change in the PVDF polarization in response to variations of temperature and mechanical stress, respectively. In the specific case of the PVDF film used in these works, the pyroelectric constant **p** and the piezoelectric constant **d** are given in its datasheet [11]:

$$\mathbf{p} = 30 * 10^{-6} \frac{C}{m^2 * °C}$$

$$\mathbf{d} = -33 * 10^{-12} \frac{C}{m^2 * Pa}.$$

In the limited range of tactile applications, the pyroelectric constant is bigger than the piezoelectric constant and, consequently, the induced charge in the floating gate, and the threshold voltage shift, are very different in the two cases.

Exploiting these different shifts of threshold voltage, we have tried to demonstrate that such a sensor is capable to detect, a clearly distinguish, temperature and force variations at the same time. In order to do that, as shown in Fig. 3.31, the PVDF has been placed on a Peltier cell, inside the sample holder of the mechanical indenter and then wire connected with the floating gate of the

OCMFET. In this way the temperature of the sensing element can be varied and at the same time a measurable force can be exerted, and measured, on it.

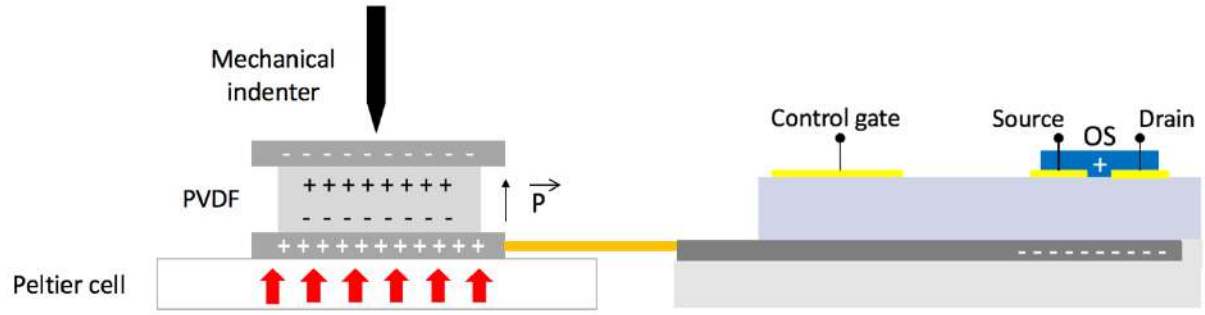

Fig. 3.31: Schematic representation of the bimodal sensor based on an OCMFET integrated with a ferroelectric polymer.

The obtained results are reported in Fig. 3.32. At first, the temperature of the sensing element has been linearly increased from 21°C up to 33° C. This temperature variation induced a clear, linear, output current decrease. Interestingly enough, during this amount of time, the PVDF has been mechanically stimulated by using three different forces (i.e. 1, 3 and 5 N). As can be seen, the output current of the sensor varies proportionally to the intensity of the applied force.

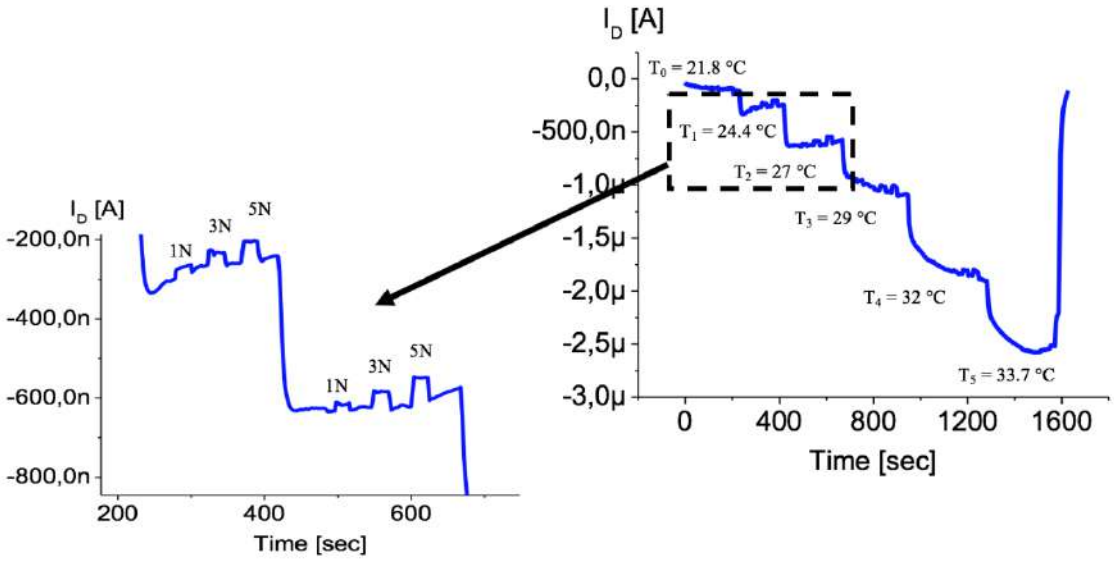

Fig. 3.32: a) Dynamic response of the sensor to the application of temperature and force stimuli on the PVDF.

Such responses are easily distinguishable as they induce an output current variation in the opposite direction of the one induced by temperature, due to a different sign in the piezoelectric constant and pyroelectric constant. In addition, the ΔI_{DS} due to a mechanical stresses, in the limited range of tactile applications, are more than 10 times smaller than those obtained during thermal stresses, as reported in Fig. 3.33. Moreover, the response to the applied force does not seem to be significantly affected by the temperature of the sensing area.

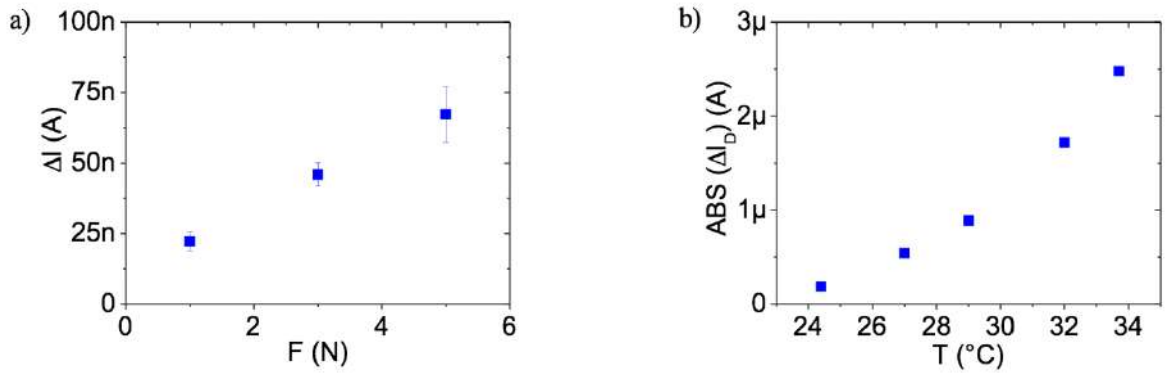

Fig. 3.33: a) Electromechanical and b) electrothermal characterization of the bimodal sensor.

3.7 Inkjet printed OCMFET as physical sensor

In previous sections, we reported tactile sensors developed with technological processes effective for laboratory-scale production. As widely introduced in Chapter 1, the development of tactile sensors for artificial skin applications, which is thoroughly considered in the field of biomedical applications, requires large-area coverage, intrinsic flexibility and lightness-in-weight that cannot be completely ensured by standard electronic processes and materials.

Moreover, when low costs are targeted, large area production processes are required instead of laboratory-scale production processes. For these reasons, it has been investigated the possibility to fabricate these kind of sensors with large area techniques, i.e. inkjet printing and chemical vapour deposition, that can be easily up-scaled to an industrial size.

3.7.1 Materials and methods

The OCMFET structure is shown in Fig. 3.34. Devices were fabricated over 125 μm-thick polyimide substrates (Kapton®, Goodfellow). Substrates were cleaned by subsequent rinse of acetone, isopropyl alcohol and deionized water. Oxygen plasma activation was performed using a Gambetti Tucano equipment, under a vacuum of 0.2 mbar with a RF power of 60W applied for 30 seconds. Plasma activation was used to increase wettability of the Kapton®'s surfaces. The OCMFET floating gate was obtained by inkjet printing a silver-nanoparticles ink (Cabot CI-330, Cabot) using a Dimatix Inkjet Printer DM2831 (Fujifilm Dimatix), equipped with 16-nozzles cartridges with a single drop volume of 1 pL. Inkjet printing was performed using a single nozzle, with a drop spacing of 25 μm, a firing voltage of 25 V and a tickle frequency of 5 kHz. Silver ink sintering was performed in oven at a temperature of 220°C for 10 seconds. As previously reported

in Lai et al. [14], the combination of surface activation, minimum ink employment and relatively high sintering temperature allows obtaining uniform, continuous and conductive silver patterns with a thickness comparable with those obtained in physical deposition processes (in the range of 200 nm).

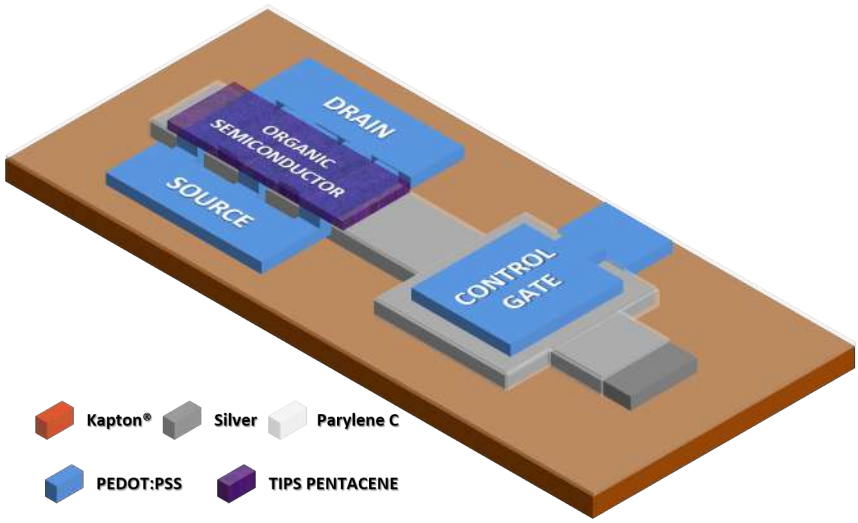

Fig. 3.34: Structure of the OCMFET.

This feature is fundamental when low voltage OFETs would be fabricated: indeed, low voltage operation can be obtained by decreasing the gate insulator thickness (i.e., increasing the capacitance per unit area of the gate dielectric), but effective and reliable insulation over large areas of relatively thick and poorly uniform printed patterns is almost impossible. As the floating gate pattern has been optimized, CVD was used to deposit a thin layer (200 nm) of Parylene C using a PDS2010 unit (Specialty Coating Systems). CVD is an industrial technique, that can be easily integrated with inkjet printing but also up-scaled to roll-to-roll processes, allowing the deposition of uniform, thin insulator layers over large area with a significant reliability. The final capacitance per area unit obtained was 9 nF/cm^2.

Source, drain and control capacitor were inkjet printed with the same equipment employed for the floating gate, using a poly(3,4-ethylenedioxythiophene):polystyrene sulfonate (PEDOT:PSS)-based commercial ink (PJET HC, Heraeus). A cartridge with 16 nozzles and a single drop volume of 1 pL was employed also in this case; a drop spacing of 20 µm was employed, while firing voltage, number of nozzles, tickle frequency and number of printed layers were varied according to the defined pattern. During the printing, the temperature of the platen was set to 60°C. In the transistor area, an average aspect ratio of 180 was obtained (W/L = 18mm/100µm, being W the channel width and L the channel length) using an interdigitated pattern. A control capacitor of 3.5 x 3.5 mm^2 was deposited. After the printing, PEDOT:PSS was dried in oven at 120°C for 15 minutes to improve insolubility to the organic solvents used for the subsequent fabrication steps.

After that, Ethylene Glycol (EG, Sigma-Aldrich) was inkjet printed to the PEDOT:PSS surface using the DMP2831, using a 16-nozzle cartridge with a 10 pL volume for single drop, employing two nozzles, a firing voltage of 40 V, a drop spacing of 50 µm and a tickle frequency of 7 kHz. EG was used to further improve insolubility of PEDOT:PSS, but also to enhance conductivity and to improve its work function, thus reducing its oxidation. EG was dried over the DMP2831 platen at 60°C for 30 minutes. 6,13-Bis(triisopropylsilylethynyl)pentacene (TIPS pentacene, Sigma-Aldrich) was chosen as p-type, organic semiconductor. A solution containing 1wt% of TIPS pentacene in anisole (Sigma-Aldrich) was prepared and used as ink with a 10pL cartridge; TIPS pentacene was inkjet-printed using a drop spacing of 30 µm, 5 nozzles, a firing voltage of 40 V and a tickle frequency of 7 kHz. The deposited pattern was let drying at room temperature over the platen of the DMP2831.

Polyvinylidene fluoride (PVDF) was used as ferroelectric material. A 28 µm-thick PVDF film, already poled (Measurement Specialties Inc.-MEAS) was sandwiched between two metal layers in order to form a capacitor (area = 5x5 mm^2, C_{INS}= 110 pF/cm^2), and connected by a metal wire with the floating gate of the transistor. The two electrodes were made of silver and patterned by inkjet printing using a 16-nozzle cartridge with 10 pL volume for single drop, drop spacing 20 µm, firing voltage 30 V and tickle frequency 5 kHz and dried in oven at 60 °C.

3.7.2 Experimental results

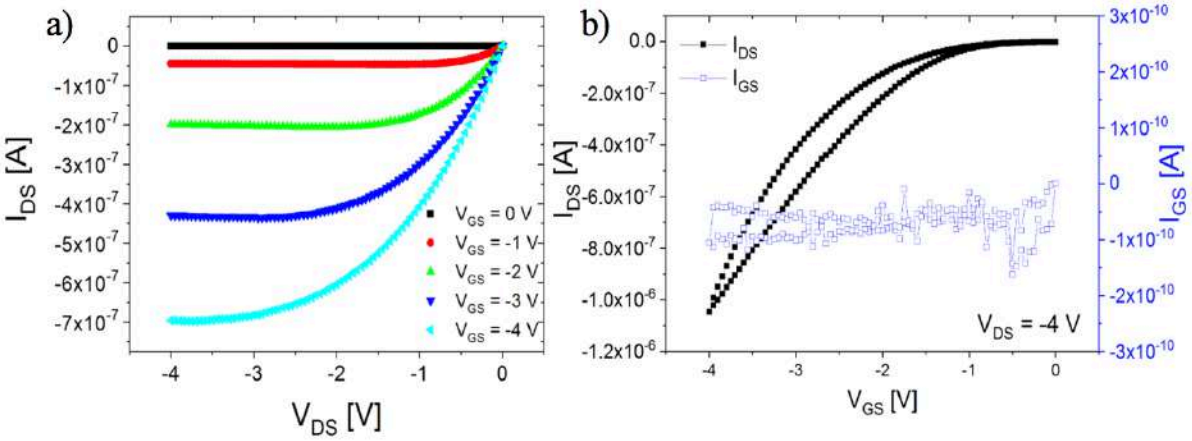

Fig. 3.35: Typical output a) and transfer b) characteristic curves of fabricated OCMFETs.

In Fig. 3.35, typical output and transfer characteristic curves of the OCMFET are reported. Twenty devices have been successfully fabricated and tested; in only one device a short-circuit between the control gate and the floating gate was observed, thus impeding its employed as OCMFET. A total process yield of 95% was thus obtained, which is particularly relevant for fabrication with

academic laboratory facilities. Devices have an average threshold voltage of 0.8±0.1 V, thus being capable to operate at low voltages ($|V_{DS}, V_{GS}|$ below 5 V). Average charge carrier mobility in saturation regime, as extracted by the square-root of the transfer characteristic curve, is $(7\pm2)\times10^{-2}$ $cm^2V^{-1}sec^{-1}$; leakage current is in the range of a few tens of pA.

This last aspect is particularly important in OCMFET structures: a too high leakage current flowing between the control gate and the source would indicate that the insulation of the floating gate is scarce, i.e. that the charge in the floating gate may vary during the measurement, thus affecting the reliability of the measurement. From transfer characteristic curve, a limited hysteresis can be also noticed, thus proving the good characteristics of injection from source/drain contacts and the organic semiconductor, and of the semiconductor/insulator interface.

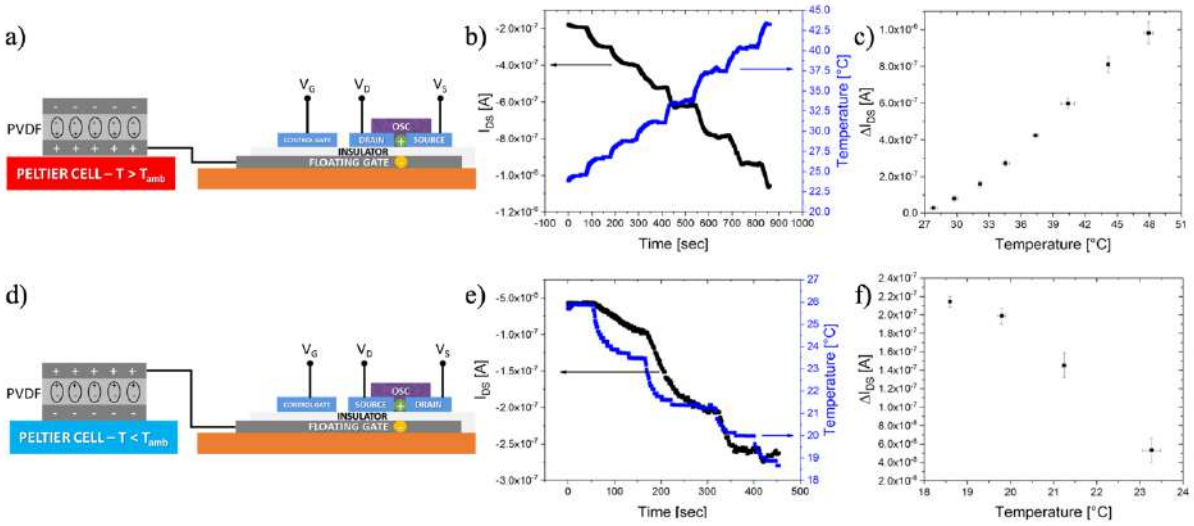

Fig. 3.36: a) connection of the OCMFET with the PVDF capacitor for temperature sensing test with $T > T_{amb}$; b) example of current variation (black curve) recorded in real-time for increasing temperatures, monitored by an optical pyrometer (blue curve); c) calibration curve as absolute current variation vs. temperature (each point averaged over 5 measurements); d) connection of the OCMFET with the PVDF capacitor for temperature sensing test with $T < T_{amb}$; e) example of current variation (black curve) recorded in real-time for decreasing temperatures, monitored by an optical pyrometer (blue curve); f) calibration curve as absolute current variation vs. temperature (each point averaged over 5 measurements).

The floating gate was connected with a plate of the PVDF capacitor by means of a metal wire, while the other plate was left floating during the experiment Fig. 3.36 a). Since PVDF has a non-zero polarization vector, the choice of the plate connected to the floating gate change the way the OCMFET will respond to temperature variations, provided by a Peltier cell; the entity of temperature variations was monitored in real-time using an optical pyrometer. Fig. 3.36 b) shows the variation of the output current recorded in real-time while the temperature of the Peltier cell was progressively increased with respect to the room temperature (T_{amb} = 27°C).

It is possible to observe that the current increases, with a dynamic similar to the one of the cell, as acquired by the optical pyrometer. In Fig. 3.36 c), the calibration curve showing the absolute

current variation as a function of the temperature is reported: data are an average over five different measurements. A good linearity of the response and a significant reproducibility were obtained; a sensitivity of about 50 nA/°C was obtained. When temperatures lower than T_{amb} are considered, a current reduction would therefore be obtained: in order to transduce reduction of the temperature with respect to T_{amb} with current increase (i.e., with an increase of the signal-to-noise ratio), the floating gate can be connected to the other plate of the PVDF capacitor, as shown in Fig. 3.36 d).

In this way, as temperature decreases induce a positive charge on the top plate, holes can be attracted in the transistor channel, thus determining a current increase. Fig. 3.36 e) and f) show the results of characterization for $T < T_{amb}$: also in this case, a dynamic comparable to those of the optical pyrometer was obtained, and the response resulted quite reproducible. Differently from the previous experiment, an evident saturation of the response can be observed for the lower value of temperature considered (T = 18.5°C): this reduced linearity range can be ascribed to the charge carrier density induced by the top plate in the transistor channel at $T = T_{amb}$, that determines a shift of the transistor working point near to the saturation of the response. In conclusion, an overall linear range of the current variation between 19-50°C, with reproducible response over multiple experiments, was obtained, proving the reliability of the device performances in conditions which are relevant for several biomedical applications such as the fabrication of artificial skin.

In addition, the device has been tested for pressure sensing in the case of small pressure applied (in the range of $10^2 \div 10^3$ Pa), which is particularly interesting for biomedical applications. Pressure was applied to the capacitor using copper weights, each with a weight of 2.3g and an area of 100 mm^2, thus completely covering the area of the compressible capacitor; multiple weights were used during measurements. A plastic sheet was used to prevent a direct contact between the weights and the top plate of the capacitor, and to set the preload of the structure. In Fig. 3.37 a), the current variation in the transistor structure recorded in real-time during the application of an increasing pressure is shown. For weight values below 4.6 g (corresponding to a pressure of about 130 Pa), the current variation is almost linear with a sensitivity of about 25 nA/g, then a sub-linear response can be noticed as the limit of compression for the capacitor is approached. When such a limit is reached (weight ≥ 9.2g, i.e. pressure ≥ 190 Pa), no significant current variations are observed, with only small transient variations recorded related to the capacitive currents induced when capacitance changes. After a maximum weight of 13.8 g (corresponding to a pressure of 380 Pa) was applied, the weights were removed one by one: the device progressively reduces the current, coming back to the previous current values. In Fig. 3.37 c), the percentage variation of the output current is reported as a function of the applied pressure (blue squares); in the same plot, the percentage capacitive variation (black squares) recorded by means of an impedance analyzer on

the capacitor subjected to the same pressure values employed during the FET characterization, is reported. Also in this case, an evident amplification in the stimuli transduction is obtained; the correct choice of capacitor area and applied voltage, and the correct design of the transistor structure, allowed obtaining an average amplification of about 24% at full pressure scale, well beyond what previously reported [15].

The obtained results demonstrate that printed OCMFETs were capable to operate at low voltages, which is a fundamental requirement for correct and safety employment in biomedical applications, and for an actual portability of the devices. The fabricated devices were tested as temperature and pressure sensors by coupling them with pyroelectric elements and compressible capacitors. As temperature sensor, devices demonstrated good and reproducible responses and a sensitivity of 50 nA/°C in the range 18.5-50°C, which is relevant in several biomedical applications. As pressure sensor, the capability of the device to operate in the pressure range $10^2 \div 10^3$ Pa with reproducible performances was demonstrated. These benchmarks finally demonstrate that the proposed technology is valuable for the development of sensing platforms for biomedical applications with cost-effective techniques, that can be easily up-scaled to an industrial size.

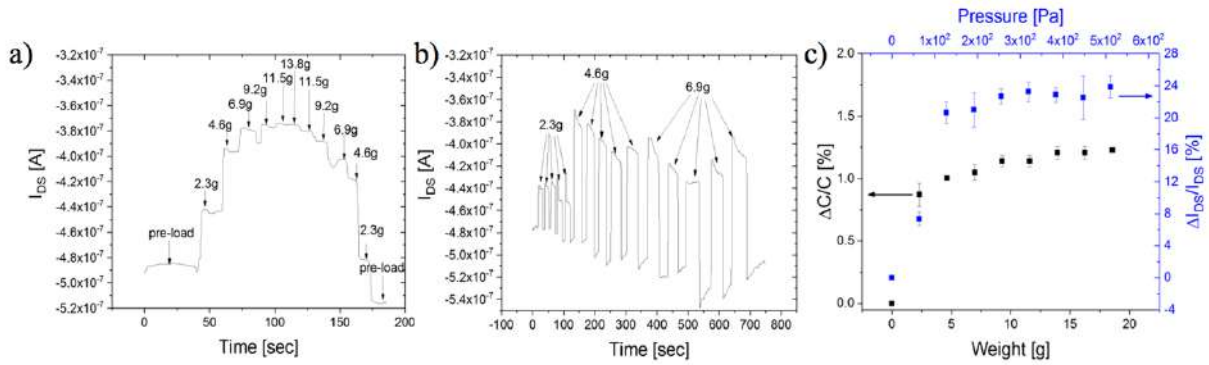

Fig. 3.37: a) I_{DS} output current recorded in real-time, while an increasing weight was applied to capacitor; b) the same experiment was repeated by subsequently applying and removing different weights for five times each; c) capacitive variation (black squares, left Y axis) and corresponding current variation in the organic FET (blue squares, right Y axis) as a function of increasing weight; corresponding pressure values are reported on the top X axis.

Bibliography

[1] M. Barbaro et al. "*A charge-modulated FET for detection of biomolecular processes: conception, modeling, and simulation*", IEEE Transactions on Electronic Devices, 2006, vol. 53 (1).

[2] M. Barbaro et al. "*Fully electronic DNA hybridization detection by a standard CMOS biochip*", Sensor and Actuators B, 2006, vol. 118, pp. 41-46.

[3] A. Caboni et al. "*Organic-based sensor for chemical detection in aqueous solution*" Applied Physics Letters, 2009, vol. 95 (12).

[4] M. Demelas et al. "*An organic, charge-modulated field effect transistor for DNA detection*", Sensor and Actuators B: Chemical, 2012, vol. 171-172.

[5] S. Lai et al. "*Ultralow voltage, OTFT-based sensor for label-free DNA detection*", Advanced Materials, 2013, vol. 25, pp. 103-107.

[6] A. Spanu et al. "*An organic transistor-based system for reference-less electrophysiological monitoring of excitable cells*", Scientific Reports, 2015, 5(8807).

[7] P. Cosseddu et al. "*Ultra-low voltage, organic thin film transistors fabricated on plastic substrates by a highly reproducible process*", Applied Physics Letters, 2012, vol. 100 (093305).

[8] P. Cosseddu, F. Viola et al. "*A temperature transducer based on a low-voltage organic thin-film transistor detecting pyroelectric effect*", IEEE Electron Device Letters, 2014, vol. 35 (12).

[9] F. Viola et al. "*Flexible Temperature sensors based on Charge Modulated Organic Thin Film Transistors*" Ph.D. Research in Microelectronics and Electronics (PRIME), 2015.

[10] S. Lai et al. "*Towards high frequency performances of ultra-low voltage OTFTs: Combining self-alignment and hybrid, nanosized dielectrics*", Organic Electronics, 2013, vol. 14, pp. 754-761.

[11] Measurement Specialties, "Piezo Film Sensors – Technical Manual", www.msiusa.com .

[12] P. Cosseddu, F. Viola et al. "*Tactile sensors with integrated piezoelectric polymer and low voltage organic thin-film transistors*", IEEE Sensors, 2014.

[13] A. Spanu, L. Pinna, F. Viola et al. "*A high-sensitivity tactile sensor based on piezoelectric polymer PVDF coupled to an ultra-low voltage organic transistor*", Organic Electronics, 2016, vol. 36, pp. 57-60.

[14] S. Lai et al. "*Combining inkjet printing and chemical vapor deposition for fabricating low voltage, organic field-effect transistors on flexible substrates*", Thin Solid Films, 2017, vol. 631, pp. 124–131.

[15] S. Lai et al. "*Ultralow voltage pressure sensors based on organic FETs and compressible capacitors*", IEEE Electron Device Letters, 2013, vol. 34 (6).

4 Ultra thin OCMFETs as tactile sensors

This final Chapter reports about the optimization of the OCMFET architecture, required to achieve the best performances in terms of sensitivity, and the approach we have developed for the realization of ultra-conformable artificial skin patches.

4.1 Structure optimization

As widely discussed in Chapter 3, the OCMFET is floating gate OFET biased through a control capacitor (control gate), which allows setting the transistor's working point. A key feature of the OCMFET is its elongated floating gate, which allows keeping the sensing area, i.e. the part of the floating gate upon which the actual transduction happens, far from the transistor area. The OCMFET can be employed as a tactile sensor by simply coupling the sensing area with a piezoelectric/pyroelectric material. The OCMFET transduction principle is related to the OFET's threshold voltage (V_{TH}) variation induced by a charge variation (ΔQ_T) induced under the transistor region by the presence of a charge onto the sensing area Q_S:

$$\Delta V_{TH} = -\frac{\Delta Q_T}{C_{SUM}}, \tag{4.1}$$

where C_{SUM} is the sum of the capacitances in the structure, i.e. the control capacitor's capacitance and the parasitic contributions due the superposition between the floating gate and the source and drain contacts. As this last term could be influenced by the layout of the floating gate electrode, we have investigated the possibility to tune the OCMFET sensitivity by acting on its layout-related parameters.

A direct relation of the OCMFET sensitivity to the areas composing the floating gate can be directly derived by considering the charge variation ΔQ_T that occurs under the transistor's area due to the presence of a charge variation ΔQ_S onto the sensing area (A_S). In particular, ΔQ_S determines superficial charge density variations $\Delta\sigma$ in the remaining parts of the floating gate, namely the transistor's area (A_T), the external areas (A_{EXT}) and the portion of the floating gate beneath the control gate (A_{CG}) shown in Fig. 4.1:

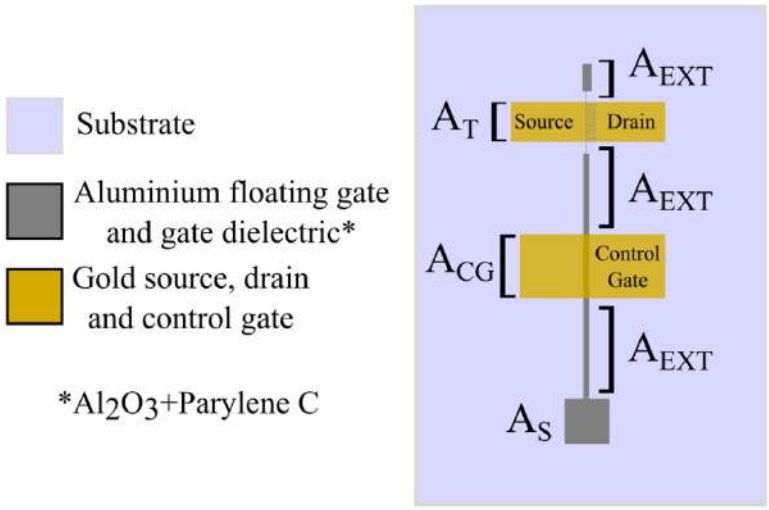

Fig. 4.1: Schematic representation of an OCMFET and its different areas.

By using the charge conservation principle applied to the floating gate:

$$\Delta Q_S = -(\Delta Q_T + \Delta Q_{EXT} + \Delta Q_{CG}) = -(\Delta\sigma_T A_T + \Delta\sigma_{EXT} A_{EXT} + \Delta\sigma_{CG} A_{CG}). \quad (4.2)$$

Since the charge under the control gate is fixed by the control gate voltage V_{CG} and the control capacitor is much larger than other capacitances in the structure, and by considering the parasitic areas A_{PAR}(i.e. the areas where there is a superposition between the floating gate and the drain and source contacts) negligible due to the source/drain self-alignment fabrication process, at steady state ΔQ_S may affect the transistor's area A_T and the external area A_{EXT} (i.e. the floating gate portions in which no direct potential is applied and which interconnect the remaining areas A_T, A_{CG} and A_S), Equation 4.2 can be written as:

$$\Delta Q_S = \Delta\sigma_s A_S = -(\Delta\sigma_T A_T + \Delta\sigma_{EXT} A_{EXT}), \quad (4.3)$$

being $\Delta\sigma_S$ the superficial charge density variation under the sensing area.

4.1.1 External areas (A_{EXT}) contribute on OCMFET sensitivity

At first, in order to optimize the OCMFET sensitivity with a proper design of the sensor architecture, we have investigated the dependence of the floating gate layout on the sensor response. Three different OCMFET structures with different external areas A_{EXT} (but same transistor and control gate areas) have been fabricated, the values of the different areas are reported in Table 4.1.

According to the fabrication process reported in section 3.3.1, the different floating gate were fabricated by depositing and patterning a thin aluminium layer over a flexible poly(ethylene therephtalate) (PET) film. After that, an ultrathin insulating layer was fabricated by using a hybrid

organic/inorganic structure, composed by a combination of alumina and Parylene C. Gold Source and Drain and also the control gate were then patterned on the insulating film using a standard photolithographic process. The 6,13-Bis(triisopropylsilylethynyl)pentacene (TIPS pentacene, Sigma-Aldrich) was used as p-type organic semiconductor. A solution of 1 wt% in anisole was drop-casted on the channel area. The control gate electrode was used for setting the working point of the sensor.

By coupling one plate of a PVDF capacitor to the sensing area, a charge perturbation is induced in the floating gate of the OCMFET (due to the PVDF intrinsic ferroelectric polarization) thus leading to a modulation of the charge carriers concentration in the OFET channel, and consequently to a variation of the threshold voltage.

OCMFET	A_T [cm^2]	A_{CG} [cm^2]	A_S [cm^2]	A_{EXT} [cm^2]	A_{FG} [cm^2]
Structure 1	1×10^{-2}	2.65×10^{-2}	2.5×10^{-1}	4.635×10^{-1}	7.5×10^{-1}
Structure 2	1×10^{-2}	2.65×10^{-2}	2.5×10^{-1}	9.635×10^{-1}	12.5×10^{-1}
Structure 3	1×10^{-2}	2.65×10^{-2}	2.5×10^{-1}	16.635×10^{-1}	19.5×10^{-1}

Table 4.1: Dimension of the different areas for each type of OCMFET employed.

By measuring the OCMFET transfer characteristics, the shift of the threshold voltage was evaluated for the three types of devices with three different floating gate areas before and after the connection of the PVDF capacitor, as shown in Fig. 4.2.

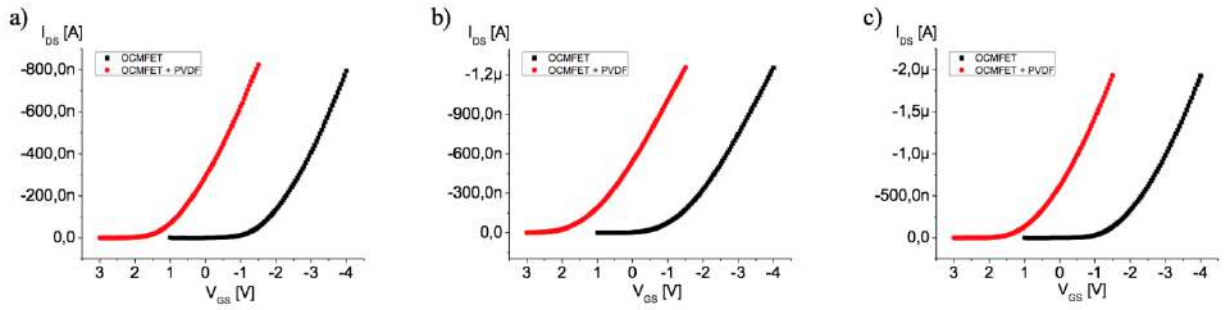

Fig. 4.2: Transfer characteristics of OCMFET before (black points) and after (red points) the coupling with the PVDF capacitor. In a) are shown transfer characteristics of one OCMFET with Structure 1, in b) are shown transfer characteristics of one OCMFET with Structure 2, in c) are shown transfer characteristics of one OCMFET with Structure 3.

As shown in Fig. 4.3, no statistically significant correlation between ΔV_{TH} and the size of the floating gate external area (in the investigated range) has been found.

A possible explanation of the obtained results reported in Fig. 4.3 is that the charge redistribution in the floating gate may be influenced by the potentials applied to the OCMFET electrodes (V_D, V_S and V_{CG}). Consequently, by assuming the floating gate behavior as the one of

an ideal metal, in this sensing configuration, a negligible charge re-distribution is expected in the external areas far from the sensing area, the transistor's area, and the control gate area. Under these considerations, it is possible to state that ΔQ_S can affect the charge redistribution only in the transistor region and Equation 3 can be simplified as follows:

$$\Delta Q_S = -\Delta Q_T \Rightarrow \Delta\sigma_S A_S = -\Delta\sigma_T A_T. \quad (4.4)$$

Then, using Equation 4.1 and Equation 4.4 is possible to derive the following expression for the threshold voltage modulation:

$$\Delta V_{TH} = -\frac{\Delta Q_T}{C_{SUM}} = -\frac{\Delta\sigma_S}{C_{SUM}} A_S, \quad (4.5)$$

being $C_{SUM}=C_{CG}+C_{PARASITIC}$ the sum of the capacitances present in the structure (namely the control gate capacitance C_{CG} and the parasitic capacitances $C_{PARASITIC}$ between source, drain, and floating gate). In particular, the term $\Delta\sigma_S/C_{SUM}$ represents the basic transduction mechanism performed by the OCMFET structure.

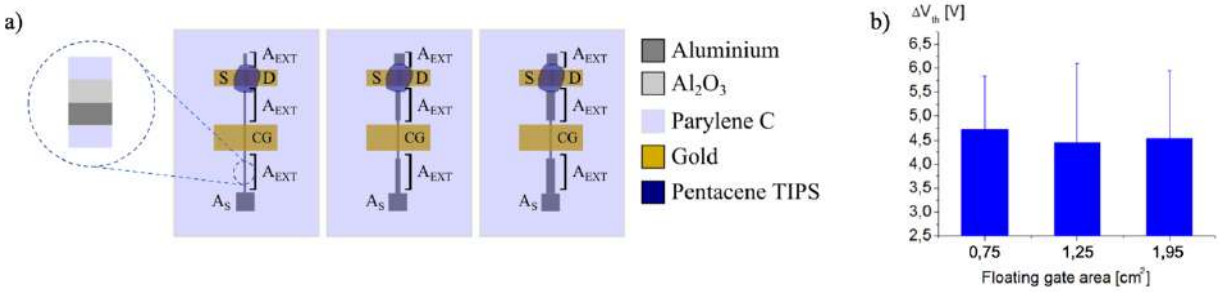

Fig. 4.3: a) Schematic representation of OCMFETs with different floating gate and employed materials. The transistor and the control gate area are the same for the three devices. b) Shift of the threshold voltage in OCMFET before and after the connection between the floating gate and the PVDF. No correlation has been observed between ΔV_{TH} and floating gate area.

4.1.2 Sensing areas (A_S) contribute on OCMFET sensitivity

In order to evaluate the validity of the simple model proposed, and in order to evaluate the dependence of the sensitivity on the sensing area dimension (as thoroughly explained in Equation 4.5), three different kinds of devices with different sensing areas (but same external, control gate and transistor areas) have been fabricated.

OCMFET devices were fabricated onto a 175 mm thick polyethylene terephtalate (PET) sheet. The aluminum floating gate and the self-aligned gold source, drain, and control gate contacts have been realized using a standard photolithographic process, while the gate dielectric is made of a thin layer (about 5 nm) of native Al_2O_x and a layer of Parylene C (Specialty Coating System) deposited through chemical vapour deposition at room temperature. At the end, a droplet of a 6,13-

Bis(triisopropylsilylethynyl) pentacene solution in anisole (1% wt) was deposited directly over the transistor channel region in order to obtain a bottom-gate/bottom-contact OCMFET structure. The values of the areas of the different parts of the floating gate are reported in Table 4.2.

OCMFET	A_T [cm^2]	A_{CG} [cm^2]	A_{EXT} [cm^2]	A_S [cm^2]
Structure 1	1×10^{-2}	2.65×10^{-2}	4.635×10^{-1}	4×10^{-2}
Structure 2	1×10^{-2}	2.65×10^{-2}	4.635×10^{-1}	2.5×10^{-1}
Structure 3	1×10^{-2}	2.65×10^{-2}	4.635×10^{-1}	10×10^{-1}

Table 4.2: Dimension of the different areas for each type of OCMFET employed.

Differently from the previous experiment, we have evaluated the shift of the output current I_{DS} instead of a direct measure of the threshold voltage. The different sensing areas were coupled with PVDF capacitors placed on a Peltier cell. The experimental setup was the same of the experiment reported in Chapter 3: we have recorded the variations of the I_{DS} during different temperature changes in the PVDF material.

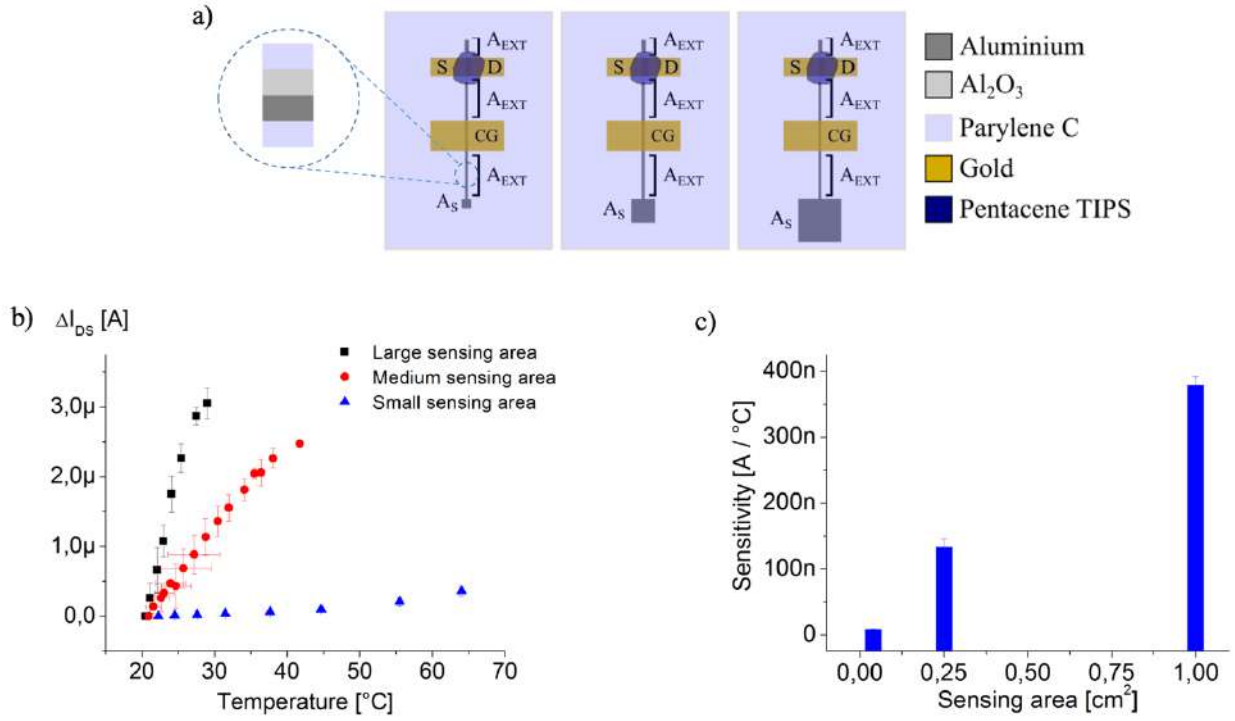

Fig. 4.4: a) Schematic representation of OCMFETs with different floating gate and employed materials. The sensing area are different for the three devices. b) Variation of the output currents in OCMFET upon the application of thermal stresses. c) Sensitivities VS sensing area for each structure employed.

The experimental results, shown in Fig. 4.4, confirmed the validity of the simple model proposed. It is important to underline that by changing the size of the sensing area is possible to finely tune the device sensitivity depending on the application requests.

4.2 OCMFET on ultrathin substrate

As widely discussed in Chapter 1, the increasing diffusion of portable and wearable technologies results in a growing interest in electronic devices having features such as flexibility, conformability, and lightness. A great interest has been focussed on devices that can be conformably transferred onto different substrates, thus resulting in the development of new technologies for the fabrication of flexible systems especially for sensing applications as, for instance, artificial skin. In order to do that, it is necessary to employ structure which are able to withstand very small curvatures, and that are characterized by small stiffness coefficients. The general approach used by many groups consists in the use of elastomeric materials which are generally characterized by very small young moduli and very low stiffness, and are widely recognized to be a suitable class of materials for the realization of conformable and stretchable electronic devices and systems.

A different approach consists in the employment of very thin substrates. As widely explain in Chapter 2, the surface strain induced ε by a mechanical deformation (see Equation 4.6), as well as the stiffness S of the structure (see Equation 4.7) are strongly related to the thickness of the substrate.

$$\varepsilon \propto t, \tag{4.6}$$

$$S \propto t^3, \tag{4.7}$$

in which ε is the surface strain, S is the stiffness and t the thickness of the substrate.

As a consequence, reducing the substrate thickness will lead, for a fixed bending radius, to reduce the induced surface strain, as reported in the plot showed in Fig. 4.5:

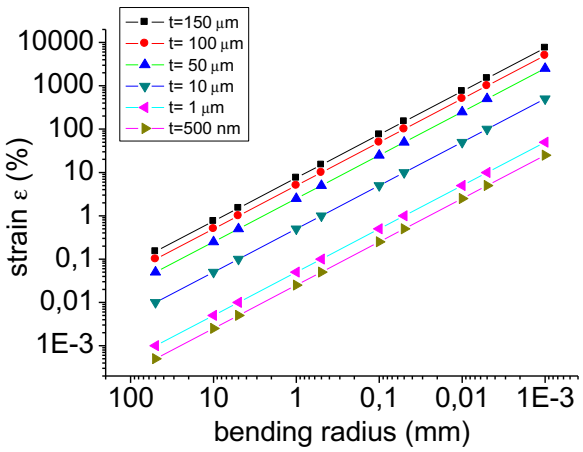

Fig. 4.5: Relationship between superficial strain and bending radius for different substrates with different thickness according to Equation 4.7.

In other words, reducing the thickness allows obtaining a much more robust structure, that, due to the reduced stiffness, can be conformably transferred onto complex surfaces, with surface corrugations in the order of tens of micrometers.

In our case, starting from a work developed in our lab several years ago [1] we have decided to employ as substrate for our devices an ultra-thin Parylene C film. The advantages of the use of nanometric sheets of Parylene C as a substrate of devices are well known in literature, in particular:

- it can be deposited over large areas with standard techniques as chemical vapor deposition (CDV).
- It can be deposited in a very reproducible way, especially in terms of thickness.
- It is fully biocompatible.
- It has interesting properties as thermal and mechanical stability, transparency, robustness to most diffused chemical agents.

Thanks to these properties they are able to stay as free-standing membranes and to conform to different substrates with different morphology and shapes: as reported in Chapter 2, the fabrication of an OTFT on top of a nanofilm represent a very innovative approach for the envisioned application of these devices in the field of ultra-conformable electronics.

4.2.1 Materials and methods

The fabrication process started with the preparation of the carrier substrates. A highly flexible *polyethylene naphthalate* (PEN) substrate was chosen for its mechanical properties and its optical properties (it is completely transparent) and was carefully rinsed with *acetone*, *isopropyl alcohol* (or isopropanol) and deionized water. Before the Parylene C deposition, a soap solution (2 wt.%

in water) was spin-coated onto the carrier substrates. The amphoteric molecules constituting the soap allow reducing the adhesion of the subsequently deposited layer to the carrier substrate, thus facilitating its removal at the end of the fabrication process.

Parylene C was then deposited on the carrier substrate by means of Chemical Vapour Deposition (CVD) using a Labcoater 2 SCS PDS 2010 (Specialty Coating System) in order to obtain a flexible ultra-thin (thickness ≅ 900 nm) supporting layer.

The aluminium floating gate electrode (∼100 nm thick) was deposited all over the Parylene C nanofilm by thermal evaporation. The material to be evaporated was placed inside a small tungsten crucible, which is connected to electrodes that can pass high current through it. For this reason, the metal can sublimate by Joule effect and can be deposited onto the substrates put over the crucible. In the deposition chamber there were vacuum conditions (∼10^{-5} Torr) and, consequently, oxygen and water molecules concentrations were very low and they could not chemically react and interact with the metal.

The patterning of the floating gate electrode was made by standard photolithography: a positive photoresist layer (AZ1518, from Microposit) was deposited onto the plastic metalized substrate by spin coating. After a soft baking step, which was necessary to evaporate the solvent, a photolithographic mask was placed onto the substrate and the system was exposed to UV light for about 2 minutes. The exposure step is followed by the development of the photoresist layer, in a NaOH solution. The last step is the etching of the metal layer that is not covered by the photoresist, in order to exactly reproduce the mask layout, with an HF solution.

The hybrid gate dielectric was a double layer composed by a thin native aluminium oxide layer (of about 5 nm) and a second thin layer of Parylene C (∼150 nm). The metal oxide was grown by thermal treatment (50 °C for 12 hours) and the Parylene C was deposited by chemical vapour deposition (CVD) process. Before the deposition of Parylene C, in order to enhance its adhesion to the metalized substrates, a small amount of sylane (A-174 Sylane) was deposited in the deposition chamber in order to create a layer of adhesion promoter. During the deposition process, little PDMS patches were placed over the sensing area which must not be covered by the Parylene C layer. As already discussed in Chapter 3, this particular hybrid gate dielectric, allowed the low voltage operation of the transistor, due to a high gate capacitance.

The last step of the fabrication process was the deposition and the definition of the layout of source and drain contacts in the transistors' area and of the control capacitors. Thanks to the good interface with p-type organic semiconductor (as Pentacene or Pentacene TIPS for instance), gold was employed for all these components. The metal was thermally evaporated in vacuum (∼10^{-5} Torr) over the Parylene C and then patterned by photolithography, according to the same procedure

already introduced for the floating gate. As only relevant difference, the chemical etching of gold was performed using a potassium iodide (KI) solution (40:4:1 H_2O:KI:I_2). An interdigitated structure was used for the channel in order to increase the width/length ratio (W/L = 630) and, consequently, the transistor's output current.

TIPS Pentacene (6,13-Bis(triisopropylsilylethynyl)pentacene) was used as p-type organic semiconductor. A solution of 0.5 wt% in toluene was dropcasted on the channel area. After deposition, the device was annealed at 80 °C on a hot plate for 30 minutes in order to increase the crystallinity of the film and to remove all the residual solvent.

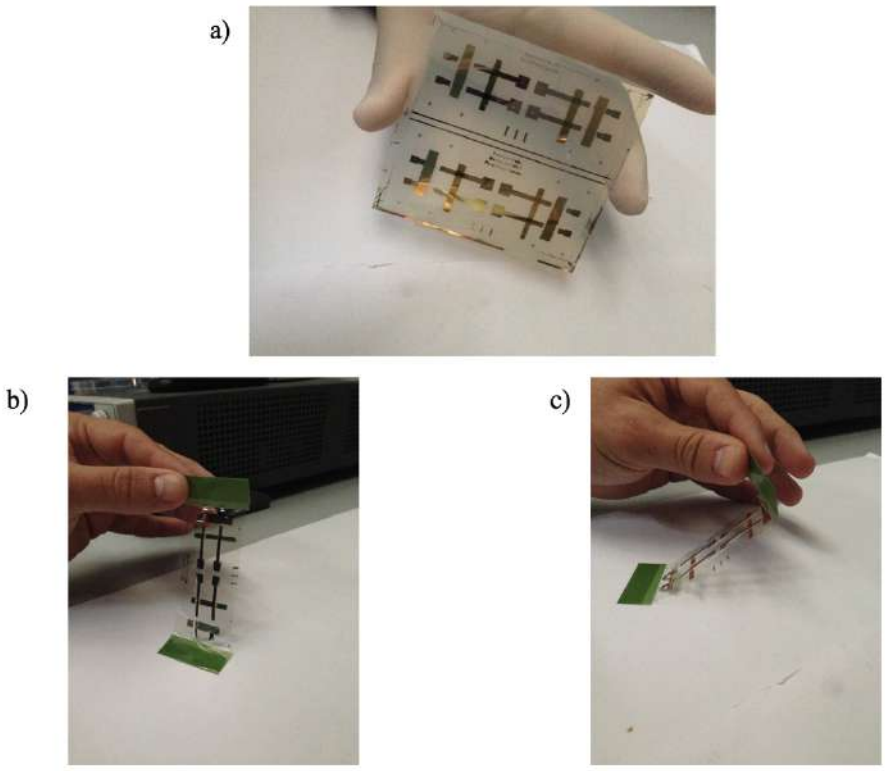

Fig. 4.6: a) OCMFET on ultrathin Parylene C substrates before the peel off from PEN carrier substrate. b) and c) Free standing devices after the peel off.

A 28 µm-thick PVDF film, already poled (Measurement Specialties Inc. – MEAS; Area = 5 x 5 mm^2) and stuck over the sensing area of the transistor using a conductive silver ink.

The complete devices were finally released from the carrier substrate by a dry peeling with the aid of an adhesive tape frame.

4.2.2 Experimental results

A Keithley 2636 SourceMeter, controlled by a custom Matlab® scripts, was employed to bias the devices and acquire the corresponding currents. During the temperature measurements, the PVDF capacitors which, were stuck over the sensing areas, were placed over a Peltier cell powered by a

Power Supply. On the other hand, during the force measurements, the sensing area were placed under a mechanical indenter connected with a dynamometer (IMADA ZP-50N) which was used to apply controlled force on the PVDF surface.

First, the device was characterized at room temperature (about 22°C) without the PVDF connected with the floating gate, in order to evaluate the electrical performances of the OCMFET before and after the peel off.

As shown in Fig. 4.7, thanks to the high capacitance coupling due to the ultrathin double layer gate dielectric, the OCMFET can be operated at very low voltage giving rise to very good electrical performances.

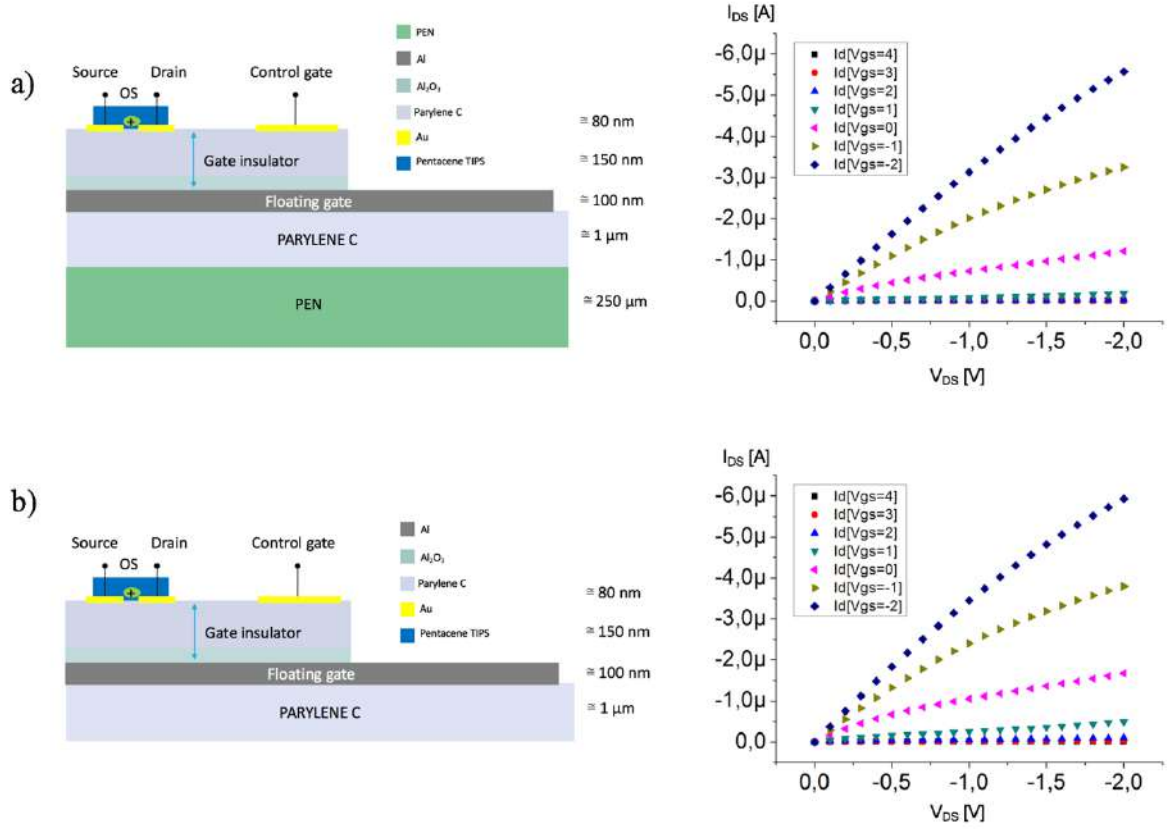

Fig. 4.7: a) Schematic representation and output characteristic of an OCMFET before the peel off. b) Schematic representation and output characteristic of an OCMFET after the peel off.

After the peel-off process, the transistor characteristics were maintained: the threshold voltage showed a shift to more positive values and, in general, we recorded an increase of the hysteresis and a worsening of the field effect. As reported in [2], these effects can be ascribed to the mechanical stress during the peel off process which caused a delamination of the nanosheet which can affect the capacitive coupling between the control gate and the floating gate. However, all these effects did not preclude the correct functionality of the OCMFETs.

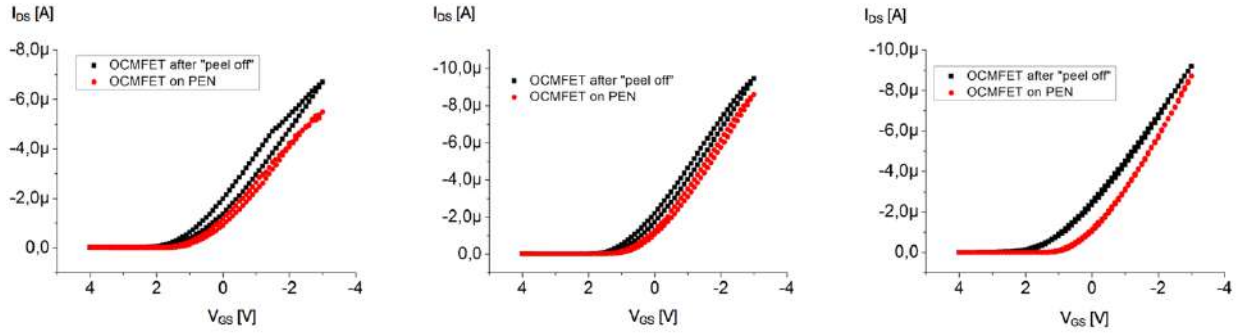

Fig. 4.8: Transfer characteristics of the devices before and after the peel off.

Preliminarily, the devices have been characterised separately as force and temperature sensors. As shown in Fig. 4.9, the temperature was increased (or decreased) step by step while monitoring the output current of the OCMFET. As it can be seen, each temperature step, according to the working principle previously explained in Chapter 3, induces a variation of the output current I_{DS}, which eventually reaches a plateau as the temperature stabilizes. In Fig. 4.9 (a-d) are shown the dynamic responses of different sensors for the same heat temperature variations, Fig. 4.9 (e) illustrates the statistics of the electro-thermal characteristics of different sensors. The response is almost linear with a very good reproducibility.

In Fig. 4.10 (a-e) are shown the sensor responses to cold temperature and the statistics of the electro-thermal characterization, even in this case the devices showed a reproducible and linear responses.

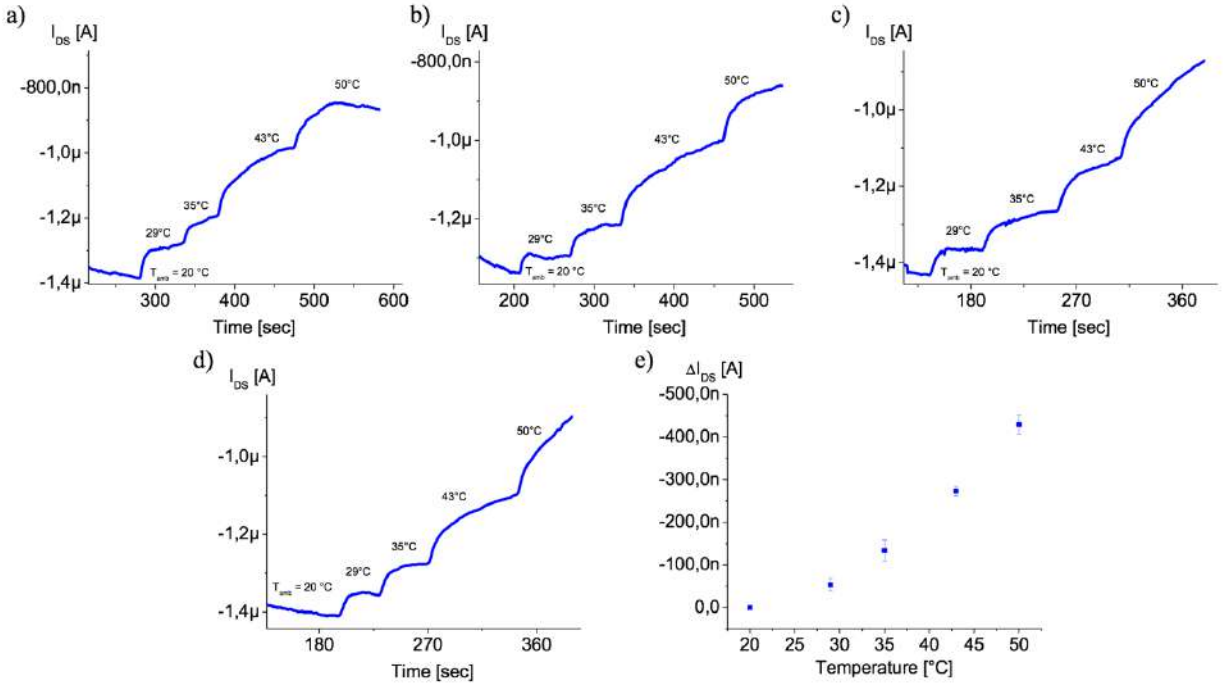

Fig. 4.9: a-d) OCMFET I_{DS} current variations upon the application of a thermal stress onto the PVDF capacitor coupled to the floating gate. e) Calibration curves of the sensor.

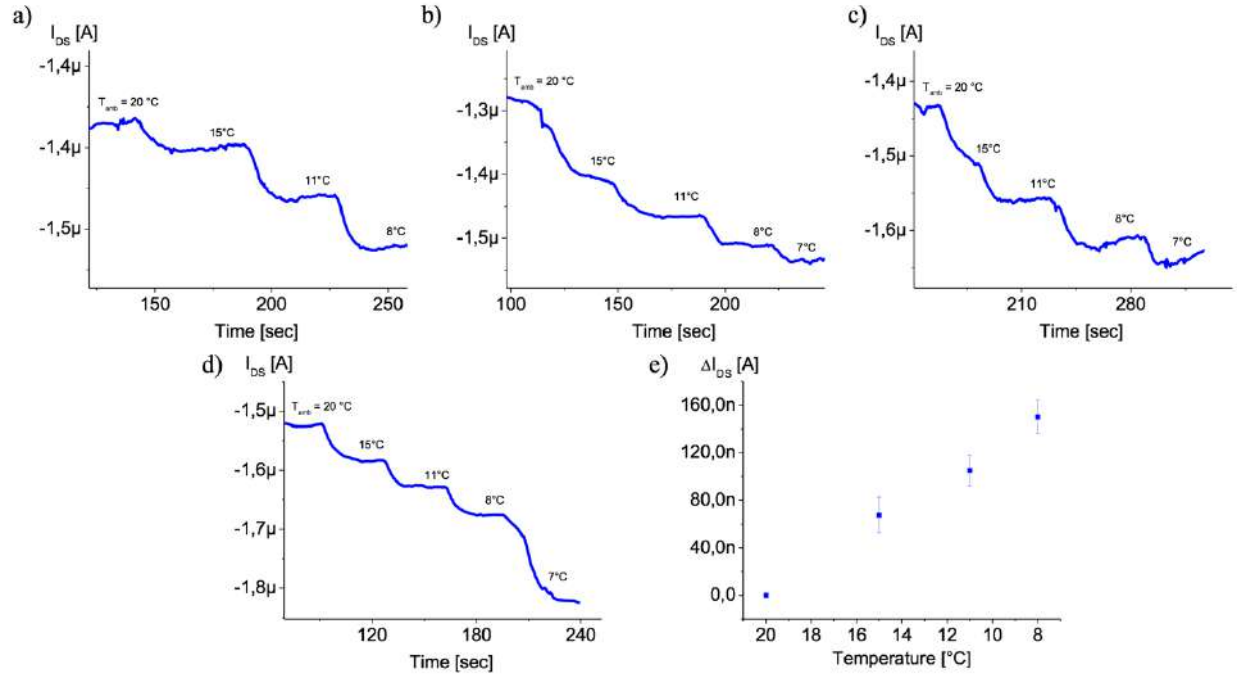

Fig. 4.10: a-d) OCMFET I_{DS} current variations upon the application of a thermal stress onto the PVDF capacitor coupled to the floating gate. e) Calibration curves of the sensor.

Depending on the side of the PVDF which is in contact with the sensing area, it is possible to obtain opposite shifts of the threshold voltage for the same thermal stimuli. As shown in Fig. 4.11, by changing the side of the PVDF on the sensing area, the variations of the drain current are exactly opposite to those obtain in Fig. 4.9.

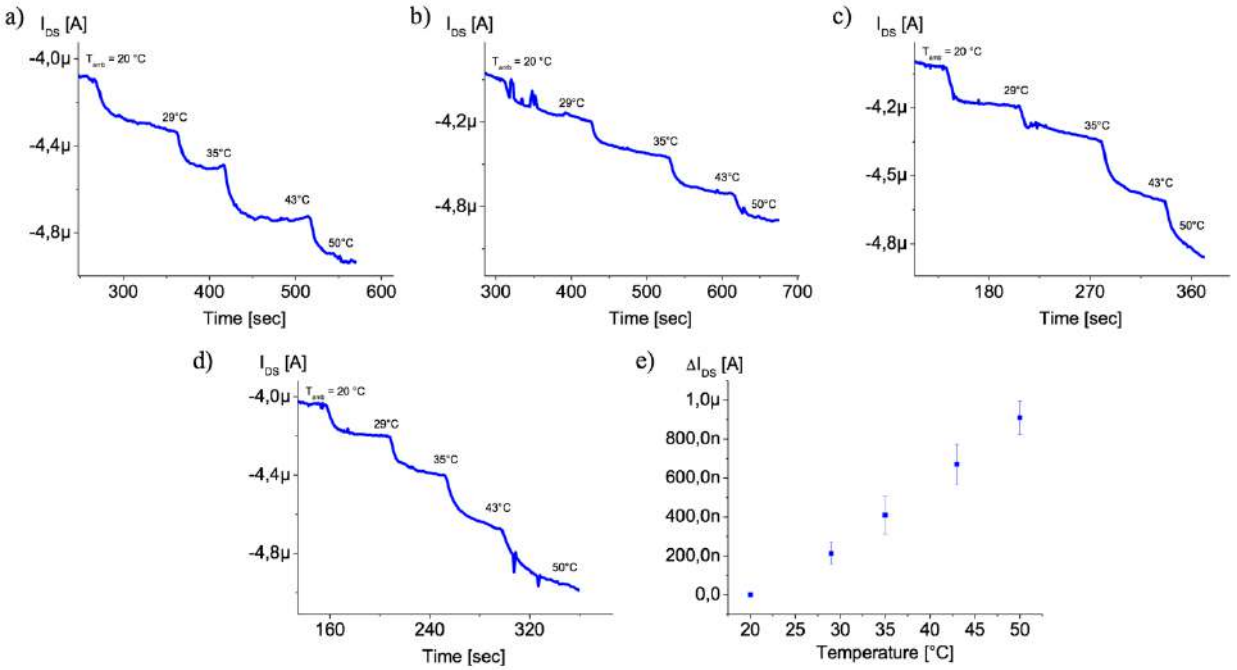

Fig. 4.11: a-d) OCMFET I_{DS} current variations upon the application of a thermal stress onto the PVDF capacitor coupled to the floating gate. e) Calibration curves of the sensor.

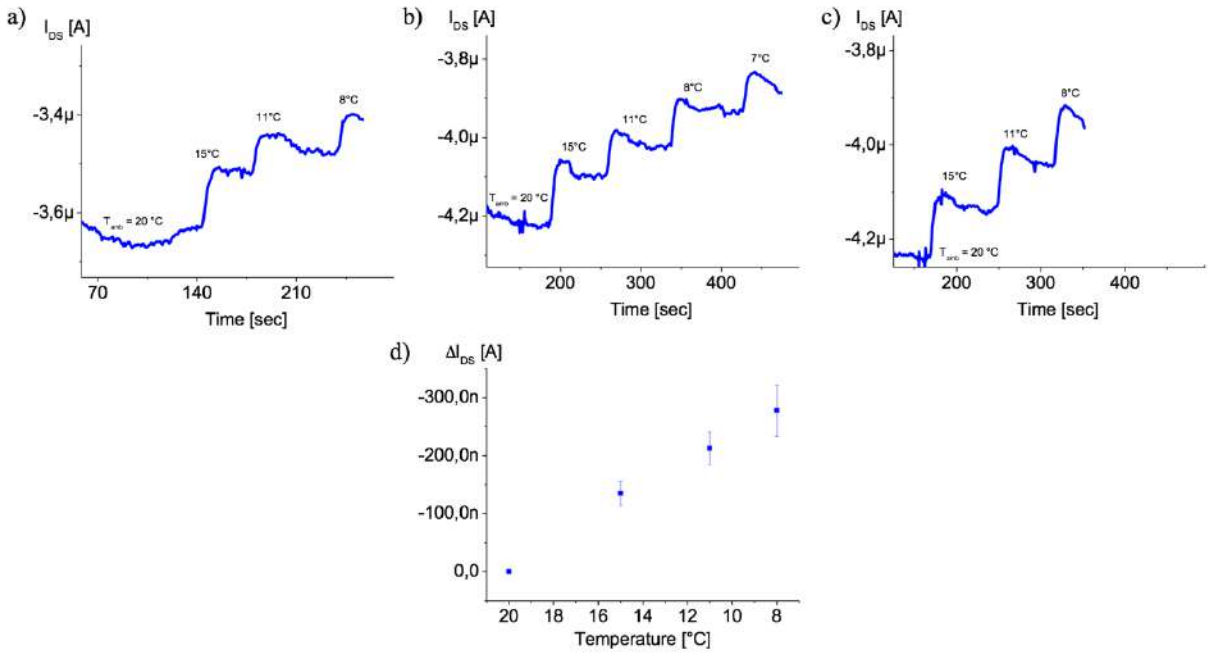

Fig. 4.12: a-c) OCMFET I_{DS} current variations upon the application of a thermal stress onto the PVDF capacitor coupled to the floating gate. d) Calibration curves of the sensor.

This electro-thermal characterization demonstrates that the proposed approach can be used for temperature monitoring within a range from 8 – 50 °C, which is the typical temperature range requested for tactile applications. Interestingly enough, also in this case a clear linear and reproducible response to the applied thermal stimulation has been obtained.

In addition to the thermal characterization, a complete mechanical characterization has been also performed. Similarly to the previously described thermal transduction mechanism, thanks to the piezoelectric property of the PVDF it is possible to obtain a threshold voltage shift in response to a mechanical stress exerted on the PVDF capacitor, thus obtaining a modulation of the output current I_{DS}.

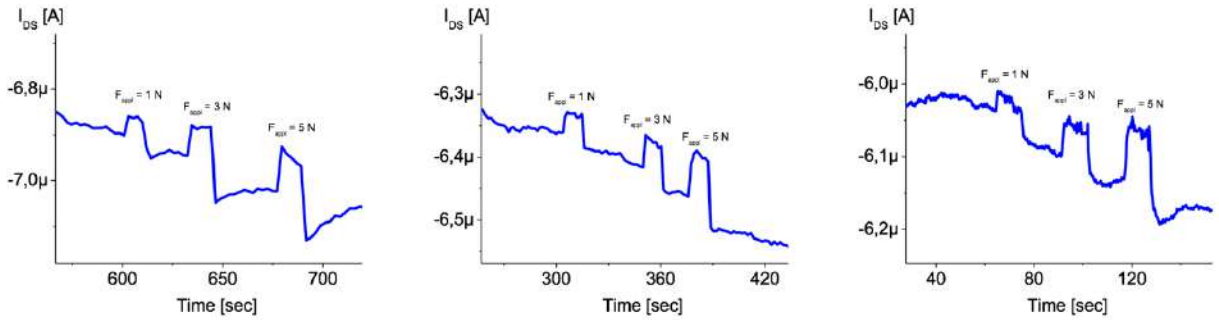

Fig. 4.13: OCMFET I_{DS} current variations upon the application of a mechanical stress onto the PVDF capacitor coupled to the floating gate.

The force can be precisely measured by using a dynamometer, so that a reliable calibration curve could be derived. In Fig. 4.14 the complete electromechanical characterization of the sensor is reported. As can be observed, the sensor is able to detect applied forces ranging from 1 up to 5 N,

which represents the required target range for tactile applications; moreover, the obtained response is linear and highly reproducible.

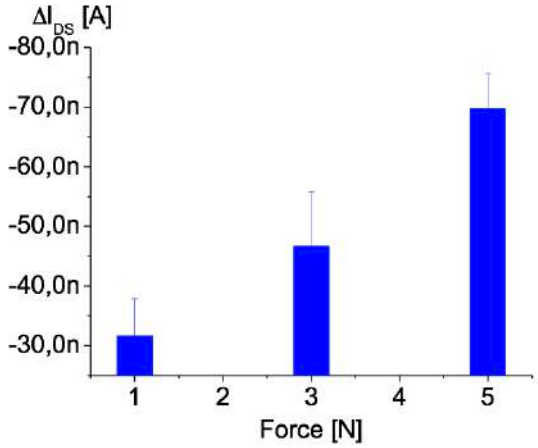

Fig. 4.14: Electromechanical characterization of the sensor.

In order to further prove that such approach could be employed in real applications, we demonstrated that the sensor is capable of discriminating temperature and force variations applied at the same time. In order to do that, the sensing area of the OCMFET has been placed on a Peltier cell, which in turn was placed on the sample holder of the mechanical indenter. In this way, the temperature of the sensing area can be monitored while, at the same time, a measurable force is exerted on the same area.

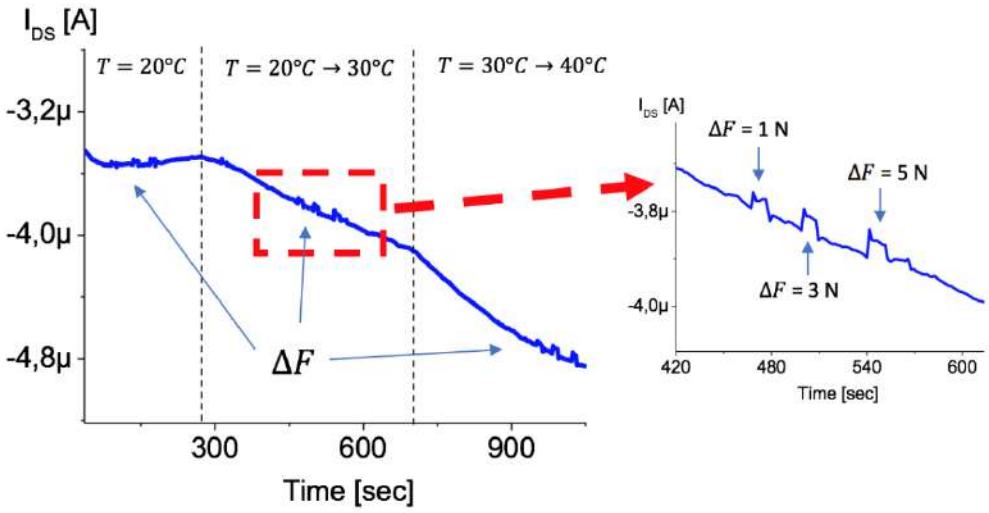

Fig. 4.15: Dynamic response of the sensor to the simultaneous application of temperature and force stimuli on the PVDF.

At first, the sensing area has been kept at a constant temperature (T = 22 °C) while being mechanically stimulated by using three different forces (i.e. 1, 3, and 5 N); as expected, the output current of the sensor varies proportionally to the intensity of the applied force. Afterwards, the temperature in the sensing area has been increased from 22 °C up to 50 °C. This temperature variation induced a clear, linear, output current decrease. As the temperature varied, the sensing

area has been simultaneously mechanically stimulated, by using the same forces applied in the preliminary mechanical characterization (i.e. 1, 3, and 5 N).

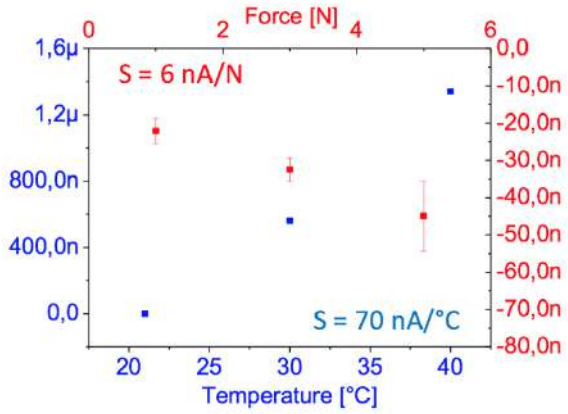

Fig. 4.16: Characterization of the sensor and sensitivities.

As can be seen in Fig. 4.15 a, also during the thermal stimulation the sensor is able to reproducibly respond to the applied pressures (see inset). As shown in Fig. 4.16, the two sensitivities (to thermal and mechanical stimuli), which are defined respectively as

$$S_T = \frac{\partial I_{DS}}{\partial T}, \tag{4.8}$$

$$S_F = \frac{\partial I_{DS}}{\partial F}, \tag{4.9}$$

lie in a very different range, namely S_T = 70 nA/°C and S_F = 6 nA/N. Referring to the typical force range requested for tactile applications [0.01 – 10 N], it is possible to assume that for temperature variations > 0.86 °C the related output current variation will be higher than the variation of the I_{DS} elicited by the maximum employed pressure stimulus. In this case the two responses are easily distinguishable. Moreover, the response to the applied force does not seem to be significantly affected by the temperature of the sensing area.

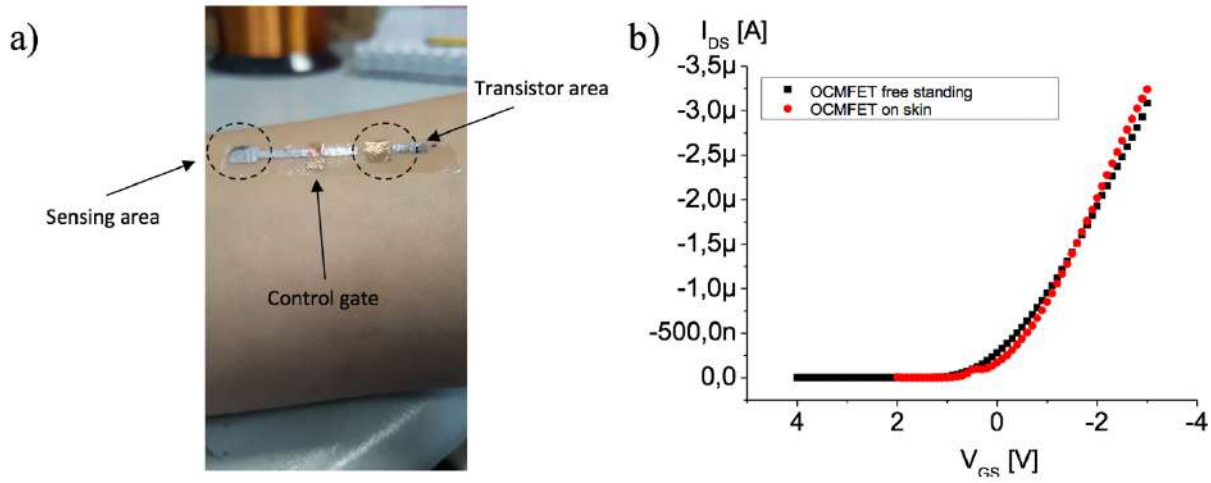

Fig. 4.17: a) OCMFET on skin, the device showed a good conformability. b) Electrical characterization of the device before and after the peel off.

In order to prove the suitability of the proposed sensor architecture for tactile applications, the sensor was transferred onto the skin and its response to a thermal stimulus was measured. As can be observed from Fig. 4.17 (a), thanks to the very small thickness of the employed substrate, the fabricated sensor structure can be conformably transferred onto the human skin like a sort of tattoo.

Moreover, as shown in Fig. 4.17 (b), the intrinsically electrical characteristics of the OCMFET (with no sensing element on the sensing area) do not change before and after placing it onto the skin. Then, after the coupling of the PVDF with the sensing area, a qualitative test has been performed to evaluate the capability of the sensor to discriminate temperature variations. In particular, both a warm and a cold object were put in the proximity of the sensing area while monitoring the sensor's output current.

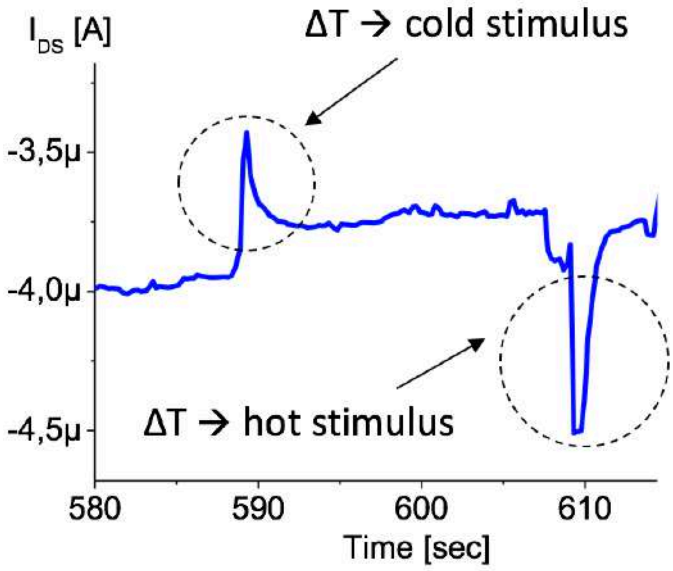

Fig. 4.18: Preliminary results of the temperature sensor on skin.

As can be clearly noticed in Fig. 4.18, when a warm stimulus is induced, according to what has been observed in the previous experiments, an output current increase is obtained; on the contrary, when a cold stimulus is applied, a marked current decrease is recorded, thus clearly demonstrating that not only the intrinsic electrical performances of the transistor are preserved, but also the sensing capability of the OCMFET are maintained after transferring such micrometric sensing system directly onto the human skin.

4.3 Bimodal sensors on ultrathin substrate

As already mentioned in Chapter 1, the minimum detectable temperature variation, requested for artificial skin applications, is 0.05 °C. Consequently, the biggest limitation of the previous approach is that is not possible to discriminate the two stimuli for temperature variations lower than 0.86 °C and is not possible to meet the previous requirement.

To overcome this problem, we here propose an alternative approach based on the combination of poly-vinylene difluoride-trifluoroethylene (PVDF-TrFE, a PVDF copolymer) sensing elements coupled with OCMFETs structures. With this approach it is possible to clearly discriminate between temperature and pressure stimuli simultaneously applied, thus suggesting the possibility of realizing multimodal sensing surface for applications in several fields, ranging from robotics to wearable electronics.

Before the description of the fabrication process of the sensors and the illustration of the experimental results, is necessary to explain the advantages of using the PVDF-TrFE instead of the PVDF. According to [3] PVDF and its copolymers are *electrets* i.e. dielectric materials capable of quasi-permanent storing electric charges at their surfaces or in their bulk, due to a result from oriented dipoles.

PVDF can crystallizes mainly to three structures:

I. Form I (also called β-form or β-phase).
II. Form II (also called α-form or α-phase).
III. Form III (also called γ-form or γ-phase).

In the β-form the hydrogen and fluorine atoms of the PVDF are symmetric respect to the carbon chain axis and by a properly polarization procedure (or poling procedure) it is possible to give to the material a large quasi-permanent polarization and the ferroelectricity (see Fig. 4.19).

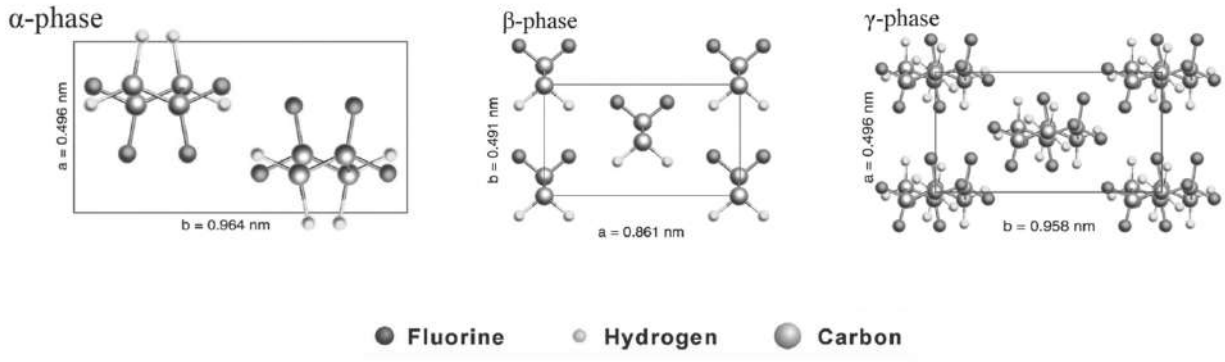

Fig. 4.19: Representation of the different phases of the PVDF and its copolymers. [4]

On the other hand, in the α-form PVDF do not show neither pyroelectricity and piezoelectricity and is a paraelectric material. In general, PVDF crystallized from the melt into to the paraelectric Form II, and it is necessary to stretch it in order to obtain the β-form [5] and then it must be poled in order to give to it the ferroelectric behaviour.

The main advantages of PVDF-TrFE is that it crystallized from the melt in the β-form and, consequently, is not needed a mechanical stretched before the poling procedure in order to achieve the ferroelectric behaviour.

Moreover, the industrial PVDF sheet used for all the experiments had a total thickness of 28 μm which is more than 25 timer higher to that of the OCMFET. In order to fabricated a fully ultra conformable and ultrathin tactile sensor it is necessary to significantly reduce the thickness of the sensing element.

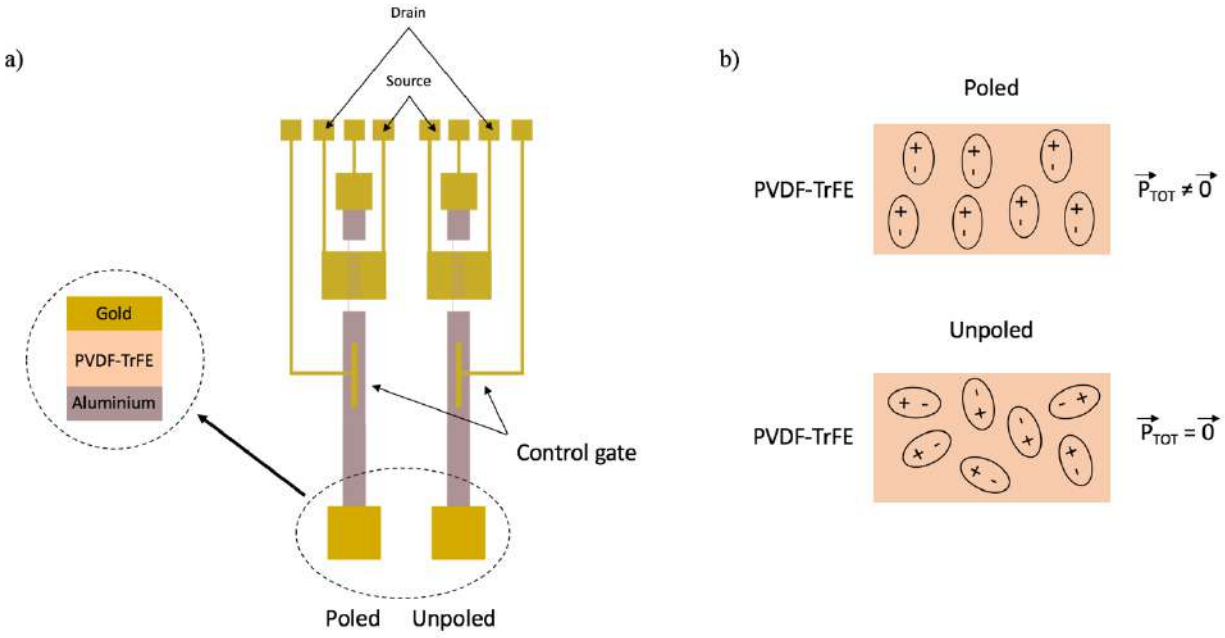

Fig. 4.20: a) Schematic representation of OCMFETs with PVDF-TrFE spin coated onto the sensing area. b) Representation of the electric dipoles in a PVDF-TrFE poled and unpoled.

The possibility to discriminate between force and temperature is achieved thanks to a system consisting in a "pixel" containing two OCMFETs: one with a poled PVDF-TrFE layer spin-coated onto the sensing area and one with the same spin-coated PVDF-TrFE layer, but unpoled (Fig. 4.20): the OCMFET with unpoled PVDF-TrFE on the sensing area is completely insensitive to temperature stimuli, while a residual sensitivity to the mechanical stimulus is due to a capacitance modulation of the OCMFET activity as already demonstrated in Lai et al. [6]. In this way, it is possible to obtain a device that is sensitive to pressure but not to temperature.

By fabricating a pixel structure containing two devices, one only sensitive to pressure and the other sensitive to both, it is possible to discriminate between the two stimuli by simply considering the difference between the two signals.

4.3.1 Materials and methods

The fabrication process of the OCMFETs structure is the same to that explain in Section 4.2.1: a highly flexible *polyethylene naphthalate* (PEN) substrate was used as carrier substrate. A soap solution (2 wt.% in water) was spin-coated onto the PEN substrates in order to facilitate the peel off procedure of the Parylene C which was deposited on the carrier substrate by means of Chemical Vapour Deposition (CVD) in order to obtain a flexible ultra-thin (thickness ≅ 900 nm) supporting layer. The aluminium floating gate electrode (∼100 nm thick) was deposited all over the Parylene C nanofilm by thermal evaporation and patterned by standard photolithography.

The hybrid gate dielectric was a double layer composed by a thin native aluminium oxide layer (of about 5 nm) and a second thin layer of Parylene C (∼150 nm). During the deposition process, little PDMS patches were placed over the sensing area which must not be covered by the Parylene C layer. Gold source, drain and control gate electrodes were deposited and patterned over the gate insulator and TIPS Pentacene (6,13-Bis(triisopropylsilylethynyl)pentacene) was used as p-type organic semiconductor. A solution of 1 wt% in anisole was dropcasted on the channel area.

4.3.2 PVDF-TrFE deposition and poling

As already introduced in Section 4.3, one of the advantages of PVDF-TrFE, instead of the PVDF, is that it crystallized from the melt directly in the β-form. In literature are reported several works in which are described different deposition techniques such as spin coating [7], printing techniques [8] – [9] etc.

The main advantage of using spin coating technique is the better uniformity of the deposited film and the possibility to change the film thickness by finely tune the spin parameters as the *spin speed* and the *spin time*.

PVDF-TrFE shows an excellent solubility in most of the polar organic solvents as *methyl ethyl ketone* (MEK), *dimethyl sulfoxide* (DMSO), *dimethylformamide* (DMF), *n-methyl-2-pyrrolidone* (NMP) etc., consequently a wide range of formulations and resulting film thicknesses are possible.

At first, the formulation and spin coating parameters for a reliable deposition in thin films using have been assessed. Before the deposition of the PVDF-TrFE directly onto the sensing area, we realized simple capacitors in order to understand the better formulation in terms of thickness, film uniformity and how optimize the poling procedure.

Different formulations were considered to obtain the most uniform film: PVDF-TrFE 10wt% in three different organic solvents (NMP, DMSO and RER500 which is a mixture of MEK and Ethyl Lactate) were investigated. After the deposition, all the samples were annealed at 140°C for two hours to increase the crystallinity of the ferroelectric β-phase of the film [9].

From AFM analysis in Fig. 4.21: AFM 2D and 3D images of PVDF-TrFE in RER500. it was possible to observe that the PVDF-TrFE in RER500 has a globular structure with porous region between the globes, on the other hand the morphology obtained with formulations in NMP and DMSO, show in Fig. 4.22 and Fig. 4.23, is rod-like with an higher uniformity.

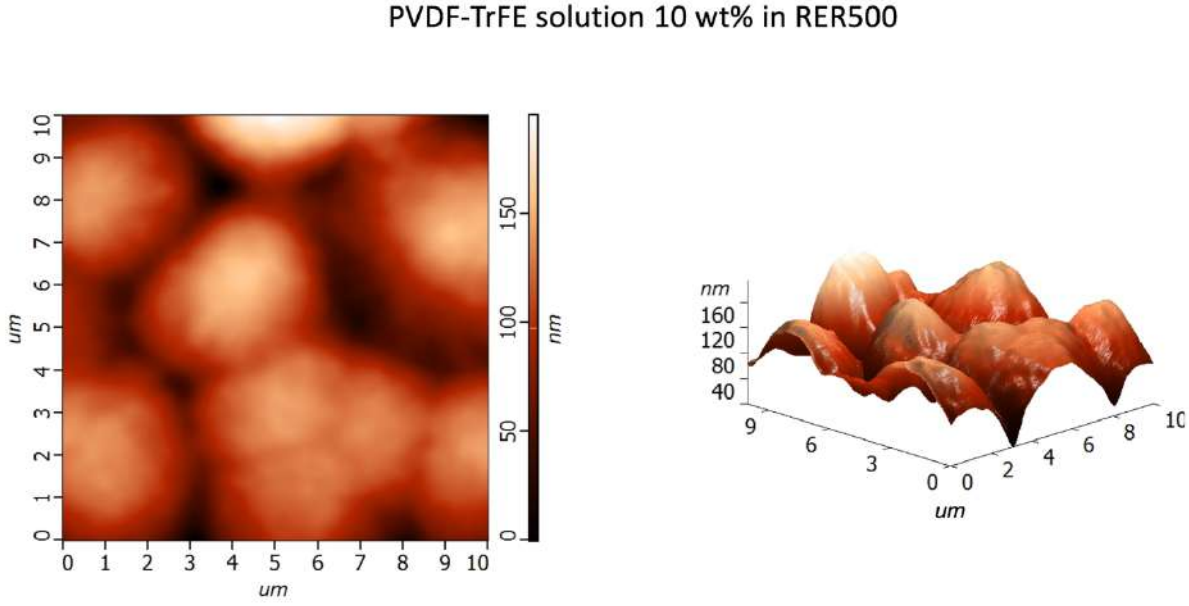

Fig. 4.21: AFM 2D and 3D images of PVDF-TrFE in RER500.

AFM has been employed for evaluating the average roughness (RMSR) of the surfaces. As reported in Table 4.3, the RMSR of the spin coated films of the NMP and DMSO formulations is limited in the order of 20 nanometes. On the other hand, RMSR of the PVDF-TrFE in RER500 is more than 5 times bigger than those of DMSO and NMP formulation.

We suppose that the higher RMSR and the different morphology of the PVDF-TrFE in RER500 is due to a lower boiling point of the employed organic solvent (~79.6 °C) than that of NMP (~202 °C) and DMSO (~189 °C) which caused a more rapid drying of the solvent and the formation of non-uniform globular morphology.

Formulation	RMSR	Thickness
PVDF-TrFE 10wt% in RER500	101,165 nm	4,33 µm ± 0,25 µm
PVDF-TrFE 10wt% in NMP	26,9362 nm	1,13 µm ± 0,25 µm
PVDF-TrFE 10wt% in DMSO	14,9383 nm	2,98 µm ± 0,39 µm

Table 4.3: RMSR and thickness of the different PVDF-TrFE formulations used.

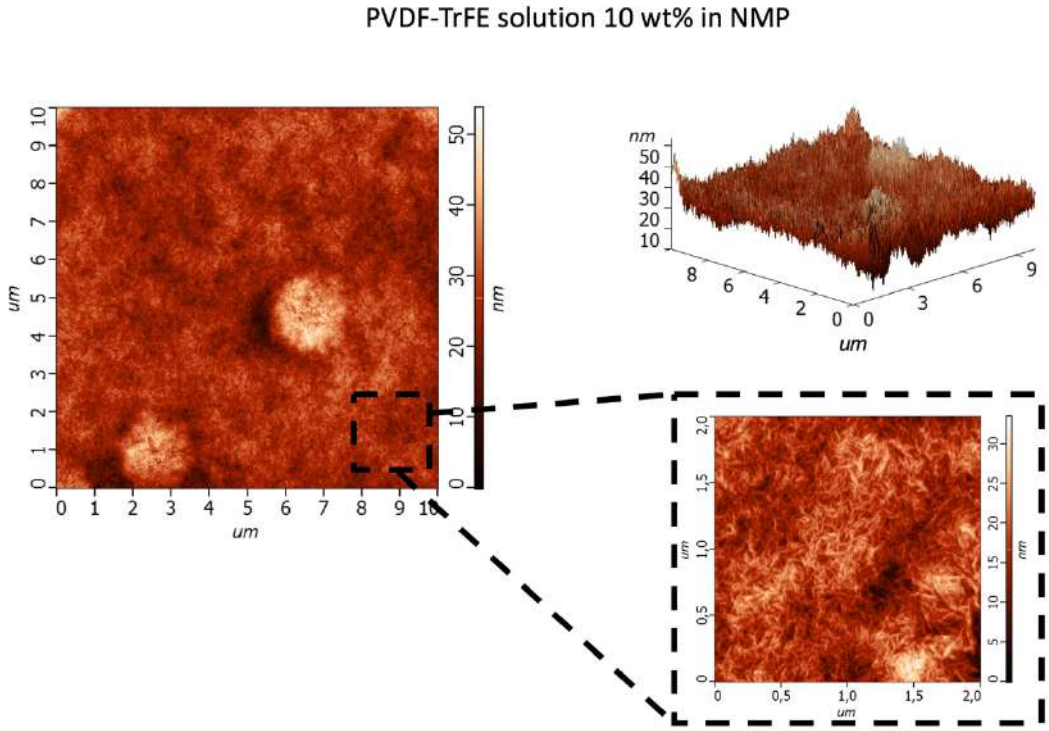

Fig. 4.22: AFM 2D and 3D images of PVDF-TrFE in NMP.

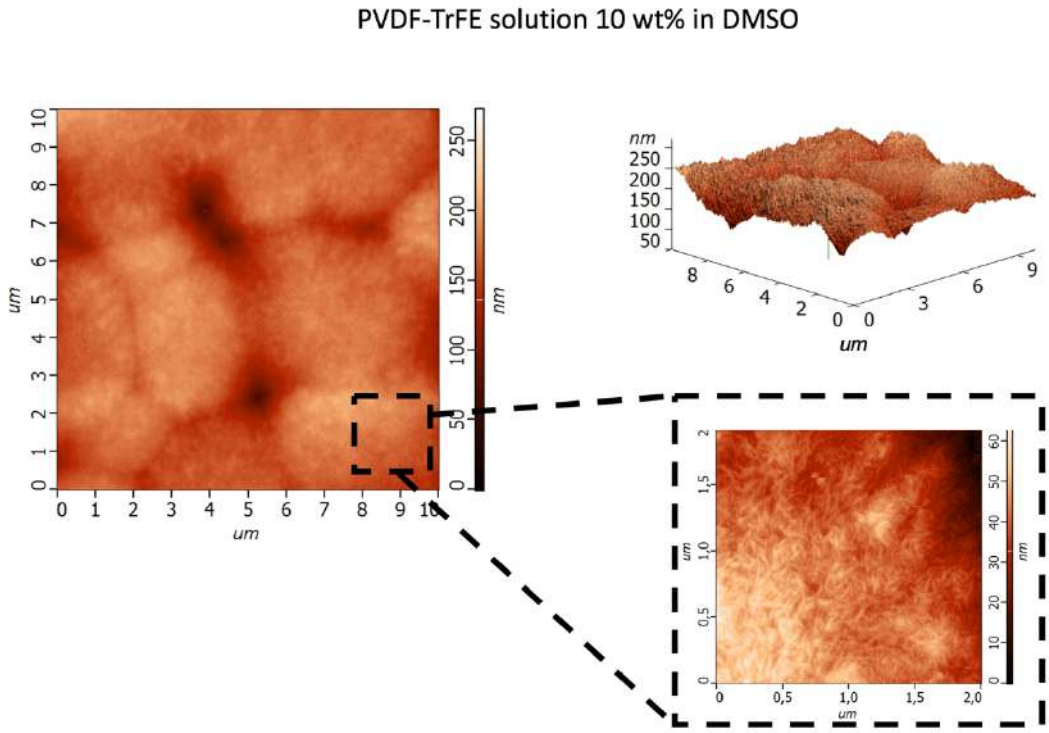

Fig. 4.23: AFM 2D and 3D images of PVDF-TrFE in DMSO.

The results of morphological characterization and profilometric analysis, have shown that the formulation in DMSO is preferred in order to fabricate PVDF-TrFE capacitors, due to a higher uniformity of the deposited film and a lower RMSR. As already explain in Chapter 2, the poling procedure (which is obtained through a high voltage across the polymer) is needed to introduce and increase piezo/pyroelectric behaviour in the PVDF-TrFE.

At first, before the deposition and poling of the PVDF-TrFE directly onto the sensing areas, we fabricated several capacitors to be connected to the sensing area of different OCMFETS for the flipping test measurement.

As already explained in Chapter 3, flipping test consists in an alternatively connection of the floating gate with the two plates of the PVDF-TrFE capacitor: by stimulating it with the same thermal stresses shifts of opposite sign of the threshold voltage are expected. This test is made in order to understand if the variations in the output current I_{DS} are related to the pyro/piezoelectric properties of the materials instead of other undesired effects and also to understand the effectiveness of the poling process of the PVDF-TrFE.

Therefore, the solution was spin coated onto a PEN substrate, in which a gold electrode was preliminarily evaporated, and then annealed at 140°C for two hours. A second gold electrode was deposited over the PVDF-TrFE film through thermal evaporation. The poling process was performed at 80 °C, and a voltage was applied across the polymer in incremental steps of 50 V at 10-min intervals up to 200 V.

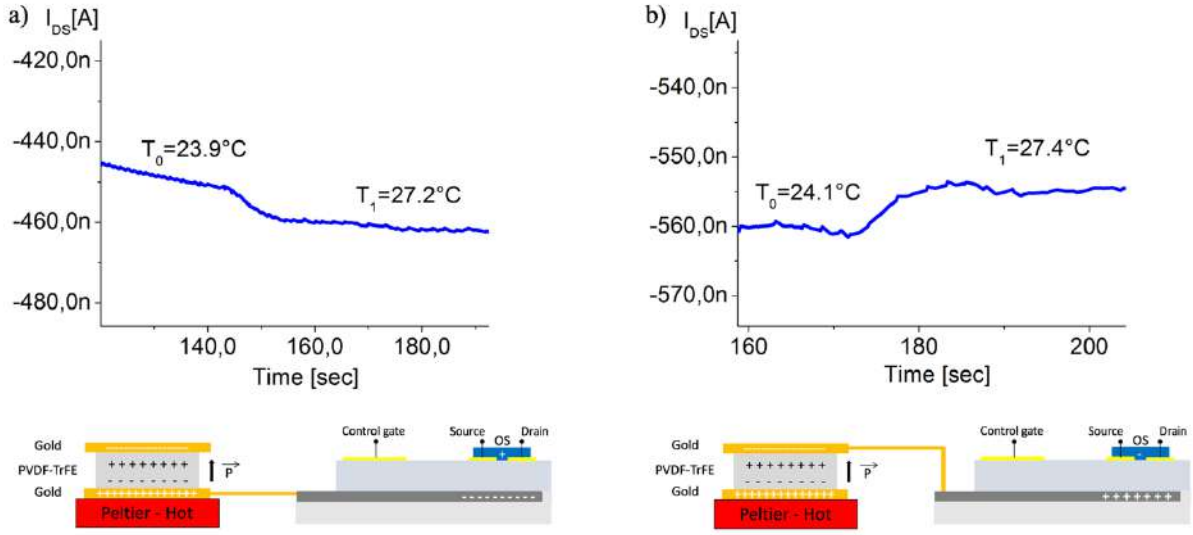

Fig. 4.24: Flipping test of an OCMFET coupled with a PVDF-TrFE capacitor in DOWN configuration (a) and in UP configuration (b).

From the plots shown in Fig. 4.24, which illustrate the flipping test of one of the capacitors poled, two important results can be highlighted. First of all, in both cases it can be clearly observed that the sensor is capable to sense temperature variations applied by the Peltier cell to the PVDF-TrFE film. Most importantly, it can be also noticed that, by connecting the floating gate of the OCMFET to the two different PVDF-TrFE electrodes, the shifts of the threshold voltage are opposite, according to the fact that the induced opposite charge in the floating gate leads to a threshold voltage shift in the opposite direction. This demonstrates that the output signal is actually a transduction of the charge induced by the thermal stimulation of the PVDF-TrFE film.

The final step for the fabrication of the bimodal sensor was the deposition and poling of the PVDF-TrFE directly onto the sensing area. The solution of PVDF-TrFE 10wt% in DMSO was spin coated on the sensing areas of the "pixel" (which consist in two OCMFETs: one with a poled PVDF-TrFE layer spin-coated onto the sensing area and one with the same spin-coated PVDF-TrFE layer, but unpoled). After the annealing (at 140 °C for two hours) the top electrodes were deposited over the PVDF-TrFE by thermal evaporation. Obviously, the two sensing areas act as bottom electrodes of the PVDF-TrFE capacitors. The poling process of only one capacitor (the OCMFET called "poled") was performed as described before.

4.3.3 Experimental results

At first, a detailed thermal characterization was performed. In this set of experiments, the Peltier cell was placed on the PVDF-TrFE capacitors and the temperature was increased (decreased) step

by step, measuring, at the same time, the output current. As can be seen in Fig. 4.25, each temperature step induces a variation of the current only in the OCMFET with the poled PVDF-TrFE, reaching a plateau as the induced temperature on the sensing element gets constant.

On the other hand, the temperature variations on the unpoled PVDF-TrFE do not affect the threshold voltage and the output current.

From this characterization, it is possible to estimate the current variations induced by each T.

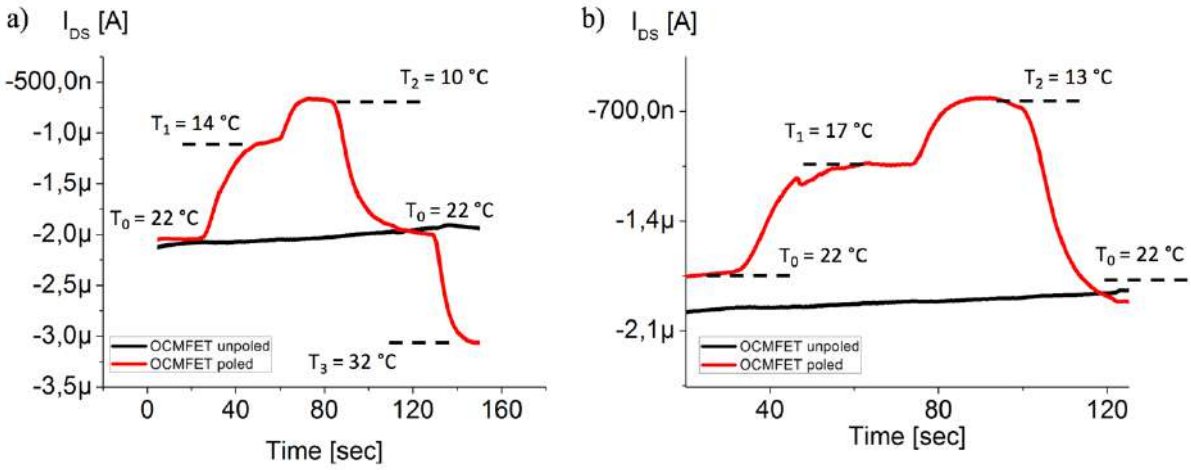

Fig. 4.25: a-b) OCMFET I_{DS} current variations upon the application of a thermal stimulus onto the sensing area with poled PVDF-TrFE (red curve) and unpoled (black curve).

After a thermal characterization, we tested the system as force sensor. The working principle of the devices is different: the OCMFET with the poled PVDF-TrFE on the sensing area, exploit the piezoelectric behaviour of the polymer when it is subject to any kind of mechanical stresses, the OCMFET with the unpoled PVDF-TrFE responds to the mechanical stimulus with a shift of the threshold voltage due to a capacitive modulation according to Equation:

$$\Delta V_{TH} = -\frac{\Delta Q_T}{C_{SUM}}, \tag{4.1}$$

Fig. 4.26 shows the output current of the two OCMFETs under a mechanical stimulus of 3 N. It demonstrates that the proposed approach can be used for detecting static forces.

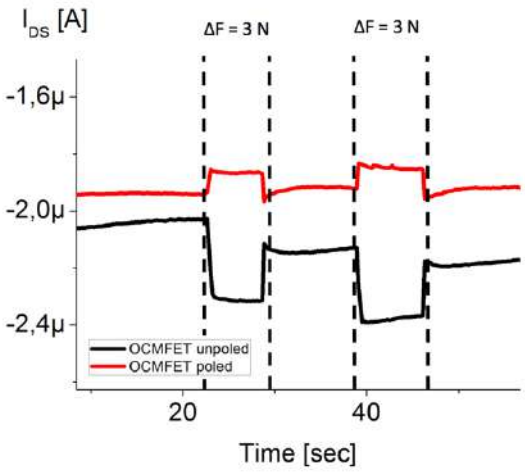

Fig. 4.26: Dynamic response of the sensor to application of force stimuli on the sensing elements.

The bimodal behaviour of the system is shown in Fig. 4.27, the calibration curves and sensitivities are shown in Fig. 4.28: coherently to the previous tests, the devices have been able to sense different temperatures and forces with different sensitivities in the typical range of tactile application.

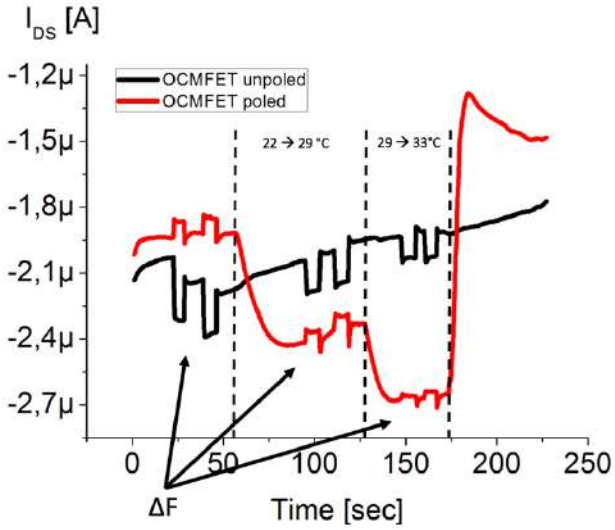

Fig. 4.27: Dynamic response of the sensor to the simultaneous application of temperature and force stimuli on the PVDF-TrFE poled (red curve) and unpoled (black curve).

Moreover, by using such a pixel and a proper readout circuit, it is possible to discriminate between the two stimuli regardless their dynamics. In addition, it is possible to finely tune the devices sensitivity and spatial resolution by changing the geometrical dimension of the sensing area, depending on the application requests. The great advantage of this approach relies on the fact that only one kind of electronic device and only one material can be used in order to fabricate a multisensing system, thus obtaining a very simple and convenient system that can be employed in epidermal applications.

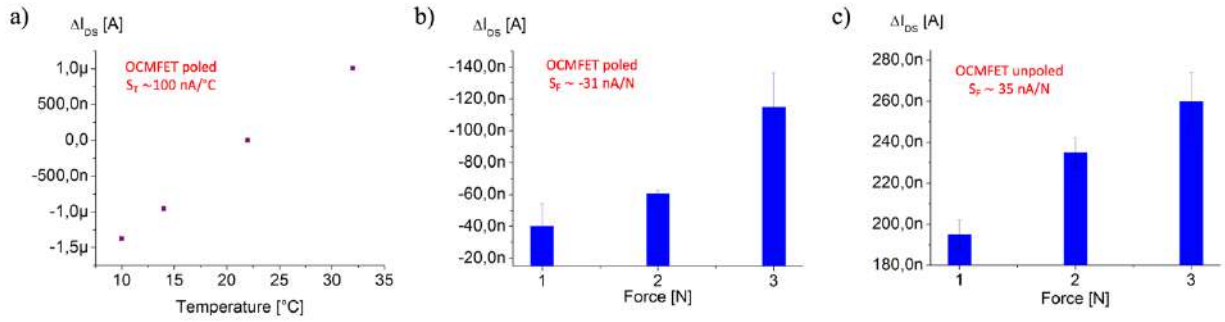

Fig. 4.28: a) Calibration curve and sensitivity of the OCMFET "poled" in response to thermal stimuli. b) and c) Calibration curve and sensitivities of the OCMFETs "poled" and "unpoled" in response to mechanical stimuli.

4.4 OCMFET as pH sensor

As widely discussed in Chapter 1, the skin is the largest organ in the human body and is a very important part of the tactile system; thanks to a complex network of sensors, the skin achieves the function of sensation thus informing the central nervous system (CNS) about the surrounding environment. It has been demonstrated that some thermoreceptors and nocioceptors (for instance the TRPV1 Ion Channel) are sensitive not only to temperature and painful stimuli, but also to chemical danger substances, so they act as *polymodal receptors*.

Referring to the object of my PhD research activity, i.e. the fabrication and optimization of tactile sensor which can simulate the sensory behaviour of human skin, we have investigated the possibility to use the OCMFET structure not only as physical sensor, but also as pH sensor in order to develop a multi-sensitive skin for several applications.

As already shown in Chapter 3, previous studies [10] demonstrated the possible employment of the OCMFET device for pH sensing, though with limited performances, mainly due to the high operating voltages.

To overcome these, we proposed a novel implementation of the OCMFET-based pH sensor [11]. Beside the possibility to operate the device with low voltages, a novel sensing layer has been employed, namely a thin film of O_2 plasma-activated Parylene C, which can be reproducibly deposited over the sensing area without any additional fabrication step. Most importantly, we have demonstrated that the proposed pH sensor, thanks to the FET amplification effect of the charge induced on the sensing area, is able to overcome the Nernst limit (i.e. the sensitivity limitation of 59 mV/pH, which is associated to the properties of the ISFET-based sensors, which are a milestones in the fields of chemical- and bio-sensing [12]), thus representing a relevant novelty in the field of biochemical sensing.

4.4.1 Device fabrication

The devices were fabricated on a 250 μm-thick polyethylene terephthalate (PET) substrate. At first, a Titanium patterned metallic film was used as the floating gate in the final sensor architecture. An UV-Ozone/thermal treatmen was subsequently performed in order to enhance the growth of the superficial native oxide layer. After that, a thin (150 nm) Parylene C film was deposited onto the entire substrate, and a gold layer was then evaporated and patterned using a self-alignment process, to obtain the drain, source, and control gate contacts. After the completion of the device, TIPS Pentacene in toluene (0.5 wt%) was drop casted directly over the channel of the transistors, and finally a glass ring (1.5 cm in diameter) was glued onto the substrate with a thin rim of polydimethylsiloxane (PDMS) in order to delimit the measurement area.

The whole structure was encapsulated with a layer (approximately 600 nm) of Parylene C, thus obtaining a 750 nm-thick layer onto the sensing area.

The sensing layer was obtained by selectively thinning the Parylene C layer over the sensing area using oxygen plasma exposure (the sensing area was selectively exposed using a patterned layer of a positive resist which was removed after the plasma activation). This process allows obtaining a simultaneous activation of the layer itself according to [13]. The initial 750 nm-thick Parylene C layer was exposed to oxygen plasma (power: 200 W; operative pressure: 0.5 mbar) for 5 min, obtaining a final thickness of approximately 500 nm (the same for all the devices).

4.4.2 Working principle

As already mentioned, the sensing layer of the OCMFET for pH sensing consists of a thin layer of O_2 plasma-activated Parylene C. Indeed, while in its pristine state Parylene C may act as an ion blocker membrane [14], after O_2 plasma exposure it acts as a H^+ sensing membrane due to the exposure of different functional groups such as C=O, C-O, O-C=O, C-O-O, and CO_3 [15].

The employment of Parylene C presents noticeable advantages since no additional fabrication step is needed, thus allowing obtaining a pH-sensitive OCMFET with no need of further chemical modifications of the sensing surface.

4.4.3 Experimental setup and results

The device sensing capability was investigated by using 500 μl of phosphate buffer solutions (PBSs) at known pH. The device overall performance was evaluated by performing electrical characterizations after 5 minutes of stabilization (the characterization is repeated three times in

order to evaluate the stability of the measurement). After each measurement, and before the replacement of the electrolyte, the sensing area was rinsed with de-ionized water. Several experiments with different sequences of PBS were carried out. Both the static and the dynamic characterization of the sensors were performed at room temperature using either a Keythley 2636 SourceMeter.

In Fig. 4.29 a), the transfer characteristics of a pH-sensitive OCMFET with the sensing area exposed to different buffer solutions (namely pH 4, 6, 7, 8, and 10) are shown. As can be noticed from the calibration curve presented in Fig. 4.29 b), the sensor showed a sigmoidal behavior and a linear response within the 6-8 pH range. The sensitivity of the reported sensor, which has been extrapolated from the linear part of the sigmoid, was about 1.4 V/pH, a value that is well beyond the sensitivities that are usually obtained with ISFETs employing Parylene C as sensing layer (i.e., ~20 mV/pH, [13]). Moreover, in order to further evaluate the sensor's sensing capability, its response has been investigated in a narrower pH interval, namely 7-7.6. As shown in Fig. 4.29 c), the device was capable to discriminate a minimum pH interval of 0.1. In addition to the static characterization, also the dynamics of the sensor was investigated.

The OCMFET pH sensor reliably responded to different PBS solutions with a good level of reproducibility and after only a few seconds of stabilization. In Fig. 4.29 d), an example of direct monitoring of current changes of an OCMFET pH sensor ($V_{DS} = V_{GS} = -1$ V) is presented. It is worth noting that, although a current drift related to bias stress effects in the OFET structure was present, the sensor was able to accurately discriminate between 3 different pH values. All the experiments have been performed after 48 hours from Parylene C activation, in order to obtain a stable level of hydrophilicity [16].

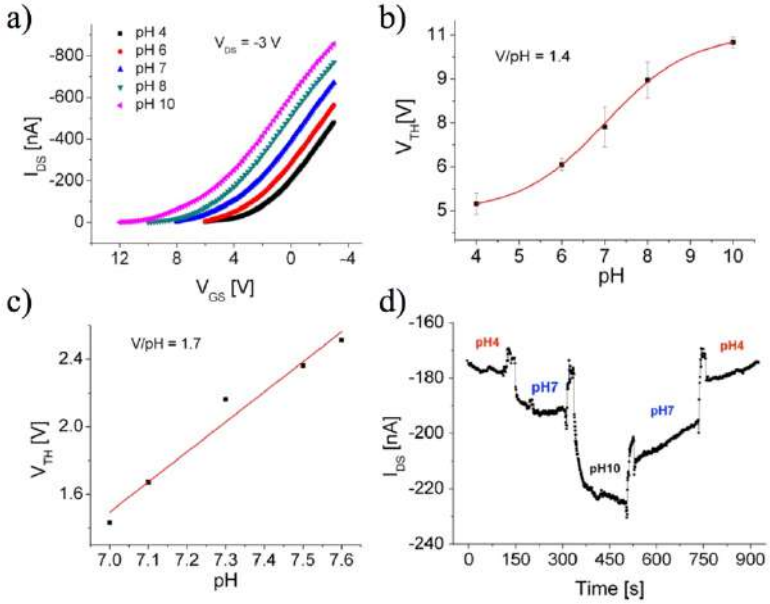

Fig. 4.29: a) Transfer characteristics in the saturation regime of an OCMFET device at different pH (from pH 4 to pH 10). b) Calibration curve of one sensor showing the typical sigmoidal behavior (mean and standard deviation of three V_{th} for each pH). c) Fine characterization of an OCMFET pH sensor in the range 7-7.6. d) Variation of the sensor output current I_{DS} over time induced by different pH values.

It has been presented an optimized OFET-based pH sensor with a plasma activated Parylene C sensing layer. Thanks to its double gate structure, the sensor is able to overcome the typical sensitivity obtained using Parylene C as the sensing element (which is limited to 20 mV/pH), obtaining V_{th} variations up to more than 1 V/pH. Moreover, the absence of a reference electrode into the liquid measurement environment, together with the intrinsic biocompatibility of the materials and the inexpensive, easy-to-process sensing layer, make the proposed approach an interesting candidate for the realization of innovative, low cost, and highly sensitive devices which can be integrated with OCMFET-based physical sensor in order to develop a multi-sensitive skin.

Bibliography

[1] P. Cosseddu et al. *"Fully deformable organic thin film transistors with moderate operation voltage"* IEEE Transactions on Electron Devices, 2011, vol. 58 (10), pp. 3416-3421.

[2] S. Lai et al. "*Ultra-conformable Organic Field-Effect Transistors and circuits for epidermal electronic applications*", Organic Electronics, 2017, vol. 46, pp. 60-67.

[3] I. Graz et al. "*Polymer Electrets and Ferroelectrets as EAPs: Fundamentals*" Springer International Publishing, 2016, pp. 1-10.

[4] Q. Li et al. "*Ferroelectric Polymers and their energy-related applications*", Macromolecular Chemistry and Physics, 2016, vol. 217, pp. 1228-1244.

[5] A. Salimi et al. "*Analysis method: FTIR studies of β-phase crystal formation in stretched PVDF films*", Polymer Testing, 2003, vol. 22 (6), pp. 699-704.

[6] S. Lai et al. "*Ultralow voltage pressure sensors based on organic FETs and compressible capacitors*", IEEE Electron Device Letters, 2013, vol. 34 (6).

[7] M. Zirkl et al. "*Synthesis of Ferroelectric Poly(Vinylidene Fluoride) Copolymer Films and their Application in Integrated Full Organic Pyroelectric Sensors*", Ferroelectrics, 2007, vol. 353, pp. 173-185.

[8] S. Khan et al. "*Screen printed flexible pressure sensors skin*", 25th Annual SEMI Advanced Semiconductor Manufacturing Conference (ASMC), 2014, pp. 219-224.

[9] O. Pabst et al. "*All inkjet-printed piezoelectric polymer actuators: Characterization and applications for micropumps in lab-on-a-chip systems*", Organic Electronics, 2013, vol. 14, pp. 3423-3429.

[10] A. Caboni et al. "*Flexible Organic Thin-Film Transistors for pH Monitoring*", IEEE Sensors Journal, 2009, vol. 9, pp. 1963-1970.

[11] A. Spanu, F. Viola et al. "*A reference-less pH sensor based on an organic field effect transistor with tunable sensitivity*", Organic Electronics, 2017, vol. 48, pp. 188-193.

[12] R. E. G. Van Hal et al. "*A novel description of ISFET sensitivity with the buffer capacity and double-layer capacitance as key parameters*", Sensors & Actuators B: Chemical, 1995, vol. 24, pp. 201-205.

[13] T. Trantidou et al. "*The dual role of Parylene C in chemical sensing: Acting as an encapsulant and as a sensing membrane for pH monitoring applications*", Sensors and Actuators B: Chemical, 2013*,* vol. 186, pp. 1-8.

[14] T. Matsuo et al. "*Parylene-gate isfet and chemical modification of its surface with crown ether compounds*", Sensors and Actuators, 1986, vol. 9, pp. 115–123.

[15] J. S. Song et al. "*Improved Biocompatibility of Parylene-C Films Prepared by Chemical Vapor Deposition and the Subsequent Plasma Treatment*", Journal of Applied Polymer Science, 2009, vol. 112, pp. 3677–3685.

[16] T. Trantidou et a. "*Oxygen plasma induced hydrophilicity of Parylene-C thin films*". Applied Surface Science, 2012, vol. 261, pp. 43-51.

Conclusions

A novel approach for the fabrication of multimodal tactile sensors based on organic transistors, for *artificial skin* applications, has been presented.

The attempt to create an artificial skin or *electronic skin* (*e-skin*), i.e. a skin like tissue that can simulate the receptive behaviour of human skin, is motivated by the possibility to fabricate a multi-sensitive interface for different kind of applications like robotic, prosthetic and, more in general, biomedical engineering.

In the first part of this work, which covered the first year and the first part of the second year of my PhD program, it has been demonstrated that, by using a particular implementation of organic field effect transistor structure (called OCMFET), is possible to develop a physical sensor by coupling the OCMFET sensing area with a piezo(pyro)-electric polymer.

The proposed devices can sense in a highly reproducible way, temperature variations from 10 up to 50°C and force variations around 0 to 5 N. Moreover, thanks to the employed materials, the devices can operate at very low voltages and can be fabricated over flexible substrates.

In the second part of this work, it has been demonstrated that the sensitivity of the devices can be finely tuned by properly tailoring the device layout. In order to prove the suitability of the proposed approach for tactile applications, it has been shown that this kind of sensors can be fabricated over ultrathin and ultra conformable substrates with a total thickness lower than 1 μm, and they can be conformably transferred onto the human skin like a sort of tattoo. Moreover, it has been demonstrated that, by introducing an approach based on the simultaneous employment of two different OCMFETs, the system is able to discriminate between the two different external stimuli (force and temperature).

The obtained results, represent an important achievement and could potentially open the way for a wide set of application going from robotics to prosthetics to wearable electronics.

In addition, compared to the other approaches proposed in the state of the art, the main advantages of the presented device are: (i) its mechanical flexibility, shape-conformability and optimal (bio)compatibility; (ii) its bimodal behaviour; (iii) the sensing element and the amplification element (the organic transistor structure) are physically separated, preventing the external stimulus (temperature and/or force) to affect the intrinsic characteristics of the

semiconductor; (iv) thanks to its structure, it is possible to easily achieve simultaneous multimodal sensing by simply acting on the device geometry and relying only on a single sensing material.

Appendix

Organic Field Effect Transistors

OFETs are three-terminal structures: two of the electrodes, the *source* and the *drain*, are in direct contact with the semiconductor; the third, the *gate*, is isolated from the semiconductor by the insulator. The working principle is based on a modulation of the electric current flowing between source and drain electrodes when a potential is applied to the gate electrode.

An OFET must have an organic semiconducting material as the active layer. Organic semiconductors have been known since the late 1940s. However, the first transistor based on an organic semiconductor was only reported in 1986 with a device made on an electrochemically grown polythiophene film[1].

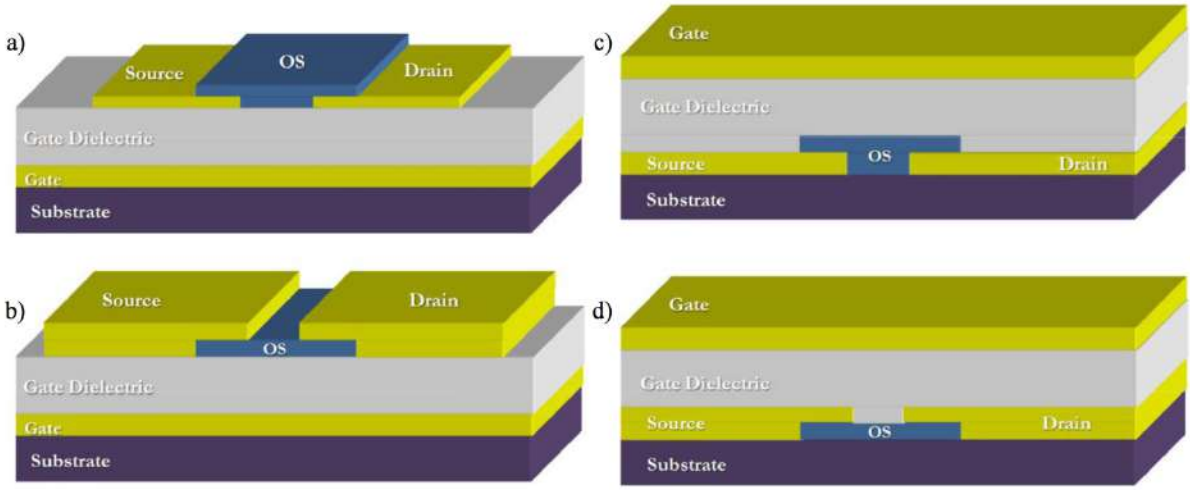

Fig. A1: Different configurations of OTFT.

In general, organic semiconductors are characterized by a very low conductivity and, consequently, OFETs adopt the architecture of the thin film transistor (TFT), in which the conducting channel is constituted by an accumulation layer rather an inversion layer[2].

Depending on the position of the organic semiconductor layer respect to the electrodes, is possible to define four different configurations for the device structure:

- bottom gate - top contact. The source and drain electrodes are located above the semiconductor layer while the gate lies below it, as shown in Fig. A1 b);

[1] H. Koezuka, A. Tsumura, T. Ando, *Synth. Met.* **1987**, *18*, 699-704.

[2] G. Horowitz, *Adv. Mater.*, **1998**, 10, 5, 365-777.

- bottom gate - bottom contact. The semiconductor layer is located above all the three electrodes, as shown in Fig. A1 a);
- top gate - top contact. All the three electrodes are above the semiconductor layer top gate, as shown in Fig. A1 d);
- top gate - bottom contact. The gate electrode is located above the semiconductor layer while the source and drain electrodes are below it, as shown in Fig. A1 c).

OFETs working principle

In OFETs, the output current I_{DS} flowing between source and drain depends on the matching between the Fermi level of the metal electrodes and HOMO (highest occupied molecular orbital) and LUMO (lowest unoccupied molecular orbital) of the organic semiconductor. Referring to Fig. A2, it is possible to define the hole injection barrier (Φ_{Bh}) as the difference between the ionization energy of the semiconductor (IE) and the metal work function (Φ_M); on the other hand, the electron injection barrier (Φ_{Be}) was defined trough the difference between the electrode work function (Φ_M) and the organic electron affinity (EA)

In a OFET with the Fermi level of the source and drain electrodes close to the LUMO of the semiconductor, electrons can be injected/extracted due to a low value of the the electron injection barrier (Φ_{Be}). When V_{GS} (i.e. the potential between gate and source is positive, electrons are attracted in the channel within few angstroms from the insulator-semiconductor interface and can be driven from source to drain by applying a positive voltage between drain and the source.

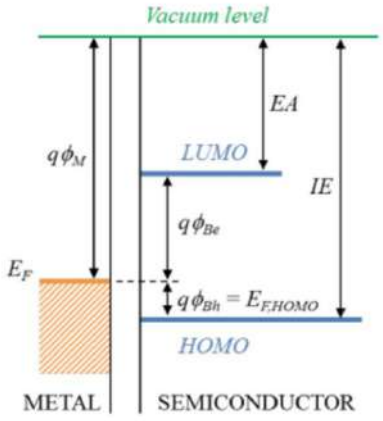

Fig. A2: Energy diagram of a metal-organic semiconductor interface

On the contrary, when the $V_{GS} < 0$, holes are induced in the channel. As the Fermi level of the metal is far from the HUMO of the semiconductor, the holes injection/extraction is very unlikely due to a very high value of the hole injection barrier (Φ_{Bh}), therefore, no current flows through the semiconductor except for leaks through the insulating layer. In this case, the organic material is named *n-type* as holes are the majority charge carriers, and the device is named *n-channel* as it is

activated upon the application of a positive gate potential.

OFET with the Fermi level of the source and drain metal close to the HUMO of the semiconductor has a symmetrical behavior.

In a OFET the charge transport is highly localized in few angstroms from the insulator-semiconductor interface but the bulk of the material is hardly or not affected by gate induced field.

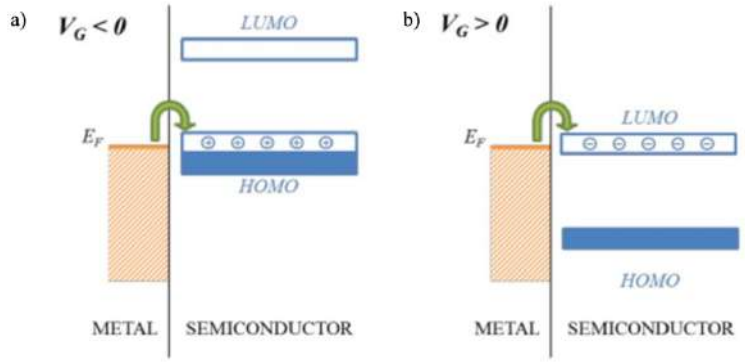

Fig. A3: a) Charge injection with respect to the applied voltage in a p-type semiconductor, b) Charge injection with respect to the applied voltage in a n-type semiconductor.

In the case of a p-channel device, increasing the gate voltage to positive values (i.e. $V_{GS} > 0$), the number of charge carriers accumulated in the channel will reduce until the channel is fully depleted of free carriers. In principle, OFET should work in inversion regime if a positive gate voltage can accumulate negative charge carriers, but the current in inversion regime is negligible due to the high injection barrier at the interface between metal electrodes/semiconductor.

Consequently, it is possible to define as *threshold voltage* (V_{th}) of the OFET as the gate voltage corresponding to the boundary between the accumulation and the inversion regime. If the gate voltage is above the threshold voltage ($V_{GS} > V_{th}$) the OFET is in its OFF state, i.e. no current flows through the channel. On the other hand, if $V_{GS} < V_{th}$, a current begins to flow across the channel and two different operating regions can be identified:

- **Linear (or Triode) region**. $V_{GS} < V_{th}$ and $V_{DS} > V_{GS} - V_{th}$, the electric field induced by the gate to the channel is uniformly distributed and thus a uniform charge distribution is induced in the channel, leading to a linear increase of the current in dependence to the applied source-drain voltage.
- **Saturation regime**. $V_{GS} < V_{th}$ and $V_{DS} < V_{GS} - V_{th}$, the electric field induced by the gate at the drain contact is zero, and thus a depleted area with no induced free charge carriers is present in the channel: this phenomenon is called *pinch-off*. As a consequence, the current flowing in the channel saturates and a further increase of V_{DS} will no produce a current increase (*saturation regime*).

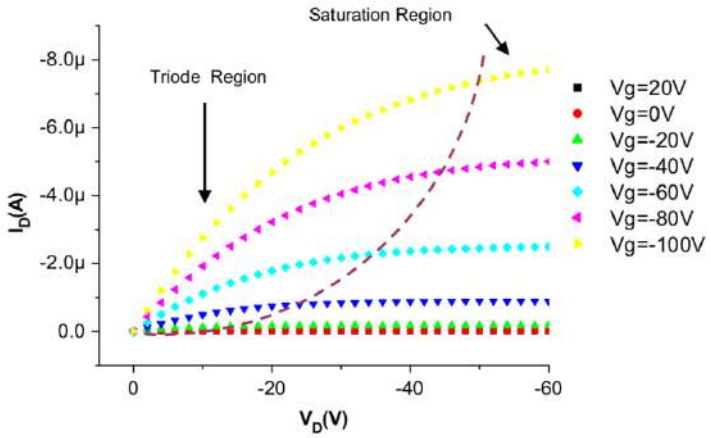

Fig. A4: Representative current-voltage characteristics of an organic field-effect transistor: output characteristics indicating the linear and saturation regimes.

In the linear regime and in the saturation regime the equations governing the device behaviour are the following:

$$I_{DS(lin)} = \frac{W}{L}\mu C_i\left[(V_{GS} - V_{th})V_{DS} - \frac{V_{DS}^2}{2}\right] \approx \frac{W}{L}\mu C_i(V_{GS} - V_{th})V_{DS}, \qquad (A1)$$

$$I_{DS(sat)} = \frac{1}{2}\frac{W}{L}\mu C_i\,(V_{GS} - V_{th})^2, \qquad (A2)$$

where W is the channel width, L is the channel length, C_i is the capacitance of the gate dielectric and μ is the charge carrier mobility.

Extraction of basic electrical parameters of OFETs

The physical parameters which are usually considered in order to characterize the electrical performances of an OFET are the following:

- the field effect mobility μ, which indicates the charge carrier mobility inferred by the applied electric field;
- the threshold voltage V_{th}, already defined previously, corresponding to the minimum gate voltage value for the formation of the conductive layer at the interface between the semiconductor and the dielectric;

In this thesis, in order to evaluate such parameters, a procedure based the prescriptions provided by the Institute of Electrical and Electronic Engineers (IEEE) it has been followed[3]: the mobility and the threshold voltage, considered constants, are determined by a linear fit of the square root of the transfer characteristic acquired in saturation regime:

[3] IEEE, *Standard test methods for the characterization of organic transistors and materials*, New York, **2008**.

$$\sqrt{I_{DS(sat)}} = \left(\sqrt{\frac{1}{2}\frac{W}{L}\mu C_i}\right)V_{GS} - \sqrt{\frac{1}{2}\frac{W}{L}\mu C_i} * V_{th}. \quad (A3)$$

In particular, the mobility can be easily extracted from the slope of the linear region of the curve described in Equation A3, and the threshold voltage can be extracted from the intercept.